

ENSEMBLE MONTE-CARLO SIMULATION OF  
QUANTUM WELL INFRARED PHOTODETECTORS, AND  
InP BASED LONG WAVELENGTH QUANTUM WELL  
INFRARED PHOTODETECTORS FOR THERMAL IMAGING

A THESIS SUBMITTED TO  
THE GRADUATE SCHOOL OF NATURAL AND APPLIED SCIENCES  
OF  
MIDDLE EAST TECHNICAL UNIVERSITY

BY

ORAY ORKUN CELLEK

IN PARTIAL FULFILLMENT OF THE REQUIREMENTS  
FOR  
THE DEGREE OF DOCTOR OF PHILOSOPHY  
IN  
ELECTRICAL AND ELECTRONICS ENGINEERING

SEPTEMBER 2006

Approval of the Graduate School of Natural and Applied Sciences

---

Prof. Dr. Canan ÖZGEN  
Director

I certify that this thesis satisfies all the requirements as a thesis for the degree of Doctor of Philosophy.

---

Prof. Dr. İsmet ERKMEN  
Head of Department

This is to certify that we have read this thesis and that in our opinion it is fully adequate, in scope and quality, as a thesis for the degree of Doctor of Philosophy.

---

Prof. Dr. Cengiz BEŞİKCİ  
Supervisor

**Examining Committee Members :**

Prof. Dr. Tayfun AKIN (Chairman)

---

Prof. Dr. Cengiz BEŞİKCİ

---

Prof. Dr. Bilal TANATAR (Bilkent Univ.)

---

Prof. Dr. Nevzat Güneri GENCER

---

Prof. Dr. Mehmet PARLAK

---

**I hereby declare that all information in this document has been obtained and presented in accordance with academic rules and ethical conduct. I also declare that, as required by these rules and conduct, I have fully cited and referenced all material and results that are not original to this work.**

Oray Orkun CELLEK

## **ABSTRACT**

### **ENSEMBLE MONTE-CARLO SIMULATION OF QUANTUM WELL INFRARED PHOTODETECTORS, AND InP BASED LONG WAVELENGTH QUANTUM WELL INFRARED PHOTODETECTORS FOR THERMAL IMAGING**

Cellek, Oray Orkun

Ph.D., Department of Electrical and Electronics Engineering

Supervisor : Prof. Dr. Cengiz BEŞİKCİ

September 2006, 198 pages

Quantum well infrared photodetectors (QWIP) utilize quantum wells of large bandgap materials to detect infrared radiation. When compared to conventional low bandgap LWIR photodetectors, the QWIP technology offers largest format thermal imagers with much better uniformity.

The theoretical part of this study includes the development of a QWIP ensemble Monte-Carlo simulator. Capture paths of electrons to quantum wells are simulated in detail. For standard AlGaAs/GaAs QWIPs, at medium and high E-fields L valley quantum well (QW) is a trap for electrons which causes higher capture probability

when compared with InP/InGaAs and GaAs/InGaAs QWIPs. The results suggest that high photoconductive gain observed in InP/InGaAs and GaAs/InGaAs QWIPs is not due to good transport properties of binary barrier material but due to higher  $\Gamma$ -L valley energy separation.

The experimental part of the study includes the fabrication and characterization of InP/InGaAs and InP/InGaAsP QWIPs and 640x512 FPAs with the main objective of investigating the feasibility of these material systems for QWIPs. The InP/InGaAs and InP/InGaAsP QWIP detectors showed specific detectivity values above  $10^{10}$  cm.Hz<sup>1/2</sup>/W (70K, f/2, background limited). The devices offer higher allowable system noise floor when compared with the standard AlGaAs/GaAs QWIP technology. It is also experimentally shown that for strategic applications LWIR InP based QWIPs have advantages over the standard QWIP technology. The InP/InGaAs 640x512 QWIP FPA reached 36 mK average NETD value at 70 K with f/1.5 optics and 10 ms integration time. The InP/InGaAsP QWIP on the other hand yielded 38 mK NETD histogram peak at 70 K with f/1.5 optics and 5 ms integration time on 320x256 window of the 640x512 FPA.

Keywords: Infrared photodetectors, QWIP, focal plane array.

## ÖZ

### KUANTUM KUYULU KIZILÖTESİ FOTODEDEKTÖRLERİN TOPLU MONTE-CARLO SİMÜLASYONU, VE TERMAL GÖRÜNTÜLEME İÇİN InP TABANLI UZUN DALGABOYU KUANTUM KUYULU KIZILÖTESİ FOTODEDEKTÖRLER

Cellek, Oray Orkun

Doktora, Elektrik ve Elektronik Mühendisliği Bölümü

Tez Yöneticisi : Prof. Dr. Cengiz BEŞİKCİ

Eylül 2006, 198 sayfa

Kuantum kuyulu kızılötesi fotodedektörler (KKKF) büyük bant aralıklı malzemeler ile kurulan kuantum kuyuları ile uzun dalgaboyu kızılötesi ışınımı algılamaktadırlar. Geleneksel düşük bant aralıklı malzemelerle karşılaştırıldıklarında, uzun dalgaboyunda en yüksek formatta görüntülemeyi mükemmel homojenlikle sağlamaktadırlar.

Bu doktora çalışmasının teorik kısmı bir KKKF toplu Monte-Carlo simülatörü oluşturmayı kapsamaktadır. Bu simülatör ile KKKF'lerde elektronların yakalanma ve kaçış mekanizmaları detaylı olarak incelendi. Orta ve düşük elektrik alan şiddetinde L vadisi kuantum kuyusu AlGaAs/GaAs KKKF'de düşük ve sabit

fotokazanca neden olmaktadır. InP/InGaAs ve GaAs/InGaAs KKKF’de ise yüksek fotokazancın ikili bariyer malzemesi nedeniyle değil yüksek  $\Gamma$ -L vadileri enerji farkı nedeniyle olduğu ispatlanmıştır.

Doktora çalışmasının deneysel kısmı yeni InP/InGaAs ve InP/InGaAsP KKKF’lerin ve bunların 640x512 formatında odak düzlem matrislerinin üretimi ve karakterizasyonunu kapsamaktadır. InP/InGaAs ve InP/InGaAsP fotodedektörler  $10^{10}$  cm.Hz<sup>1/2</sup>/W (70 K, f/2, BLIP) mertebesinde duyarlık göstermişlerdir. Bu aygıtlar standart KKKF teknolojisine göre daha yüksek sistem gürültü tabanına izin verebilmektedirler. Ayrıca stratejik uygulamalar için InP tabanlı uzun dalgaboyu KKKF’lerin standart KKKF teknolojisine göre avantajları olduğu gösterildi. Üretilen 640x512 InP/InGaAs odak düzlem matrisi 36 mK (f/1.5, 10 ms, 70 K) ortalama NETD değerine ulaşırken, 320x256 pencere içinde InP/InGaAsP 640x512 odak düzlem matrisinin NETD histogram dağılımının tepesi 38 mK (f/1.5, 5 ms, 70K) değerinde ölçülmüştür.

Anahtar Kelimeler: Kızılötesi fotodedektörler, QWIP, odak düzlem matrisi.

## ACKNOWLEDGMENTS

I would like to thank Prof. Dr. Cengiz Beşikci, for his enlightened guidance, and his continuous effort in keeping our research laboratory active, hence giving me the chance to successfully complete this thesis.

I would like to thank Prof. Dr. Tayfun Akin for serving on my thesis progress committee, allowing my access to his laboratories. Together with Prof. Dr. Cengiz Beşikci, Prof. Akin helped us creating a productive research laboratory which allowed me and many other students/friends have a chance to enter microelectronics research world.

I would like to thank to Prof. Dr. Bilal Tanatar for his earlier work on calculation of scattering rates in quantum well structures, for his advice on simulation of electron transport through heterostructures, and for his continuous support and interest in the thesis progress committee meetings.

I gratefully thank Prof. Dr. Nevzat Güneri Gencer and Prof. Dr. Mehmet Parlak for serving in my thesis defense committee, and for their suggestions and corrections in this thesis.

I would like to thank ASELSAN Inc. for their support and funding in this research study. I would like to especially thank Electronics Design Manager Mrs. Hacer Selamoğlu, for her interest in this research study and for her support.

I appreciate continuous support of Department of Turkish Ministry of Defence and TÜBİTAK in funding the related projects.



My thanks to Ümit Tunkaya is for his continuous guidance, support and cooperation through the progress of this thesis and research projects, designing photolithography masks, useful discussions, and for his friendship.

I would like to thank Dr. Selçuk Özer for teaching me the basics of semiconductor fabrication, sharing his expertise, and for his cooperation.

I would like to thank my undergraduate and graduate classmate, laboratory colleague, and good friend Umut Bostancı for his time in coding the Monte-Carlo simulation transient response patches, for his continuous support in the project work, for the invaluable discussions, and for his bright ideas.

I would like to thank Burak Aşıcı for his careful work in flip-chip bonding, for his discussion time about HgCdTe technology, and for his friendship through the long years in the laboratory.

I thank and appreciate Hasan Koçer for his help in providing us some radiometry equipment, information about infrared imager technology, helpful discussions on applications of the QWIP imagers, his support in technological documentation, for the great encouragement in the experimental work, and for the tea-time that he shared with me allowing further discussions.

I would like to thank Suleyman Umut Eker and Melih Kaldırım for their support in the later stages of my thesis, for their friendship, and for the fun dinner, lunch and breakfast times.

I appreciate hard work of Özgür Şen for his efforts in keeping us away from the bureaucracy, and for the free tea.

Our laboratory witnessed friendship and support of Mustafa Özkan, Emre Öncü, Özlem Ersagun, Abdülkadir Yeler, Fatih Işık, and Serkan Dinmez . I thank them for creating a friendly environment.

I must thank Murat Güre from Bilkent University for his help and time in RIE etching, for his technical suggestions, for his encouragement, for a lunch, and for the jokes.

My sincere thanks are to Dr. Selim Eminoğlu, for his continuous assistance in keeping the VLSI tools active, sharing his great knowledge on IC design, test, and measurement.

I really appreciate Orhan Akar for his careful work in dicing our samples, suggestions on semiconductor processing, help in maintaining fabrication equipment, and for his great patience.

I thank Yusuf Tanrikulu for his support in using and maintaining the SEM, XPS, and for his friendship.

I thank Harun Tanık, and Murat Ünal from METU Microsystems fab for their technical suggestions in semiconductor processing, work in maintaining the process and vacuum equipment.

I thank Dr. Deniz Sabuncuoğlu Tezcan for some wire-bonding service, her cooperation, and jokes.

I thank my classmate and colleague Murat Tepegöz for his support in using the VLSI tools, and for the useful discussions.

Turkish Army Electro-optical Systems Maintenance and Repair Center continuously supported our work. I would like to thank Fuat Bıyıklı for his suggestions, and information about military thermal imaging needs.

Finally, this study could never be possible with the great support of my family, I thank them for their patience and encouragement.

## TABLE OF CONTENTS

PLAGIARISM .....	iii
ABSTRACT.....	iv
ÖZ .....	vi
ACKNOWLEDGMENTS .....	viii
TABLE OF CONTENTS.....	xi
1. INTRODUCTION.....	1
1.1 Scope.....	1
1.2 Infrared Radiation .....	4
1.3 Detecting Infrared Light.....	6
1.3.1 Photoconductive Detectors .....	7
1.3.2 Photovoltaic Detectors .....	9
1.4 Infrared Photodetectors for Thermal Imaging.....	12
2. QUANTUM WELL INFRARED PHOTODETECTORS.....	14
2.1 QWIP Operation and Characteristics .....	14
2.1.1 Intersubband Transitions in Quantum Wells .....	15
2.1.2 Standard QWIP Conduction Band Structure .....	16
2.1.3 Dark Current .....	17
2.1.4 Responsivity and Photoconductive Gain .....	19
2.1.5 Noise and Noise Gain .....	21
2.1.6 Detectivity .....	22
2.1.7 Light Coupling .....	23
2.2 Material Systems for n-type QWIPs .....	25
2.2.1 AlGaAs/GaAs .....	25
2.2.2 GaInP/GaAs .....	25
2.2.3 Other Material Systems.....	26

2.3 QWIP vs. Photovoltaic HgCdTe Detector and State of the Art.....	26
2.3.1 Latest Developments in QWIP, Superlattice and HgCdTe Technologies.....	31
2.3.1.1 Recent Developments in Multi-Color QWIP FPAs.....	35
2.3.1.2 Recent Developments in Two-Band HgCdTe FPAs.....	38
3. INFRARED FOCAL PLANE ARRAYS .....	41
3.1 Design Issues of Infrared Imagers and FPAs.....	41
3.1.1 Atmospheric Window and Peak Detection Wavelength.....	42
3.1.2 Detector Type and Material .....	44
3.1.3 Optical System .....	46
3.1.4 Read Out Circuit Topology.....	48
3.1.4.1 Direct Injection ROIC.....	49
3.1.4.2 Source Follower per Detector ROIC.....	52
3.1.4.3 Capacitive Transimpedance Amplifier ROIC.....	53
3.1.4.4 ROIC Input Stages with Current Mirror .....	53
3.1.5 Frame Rate and Integration Time .....	55
3.1.6 Cooler Requirements.....	57
3.2 FPA Figure of Merits .....	58
3.2.1 Noise Equivalent Temperature Difference.....	58
3.2.2 Minimum Resolvable Temperature Difference .....	58
4. QWIP ENSEMBLE MONTE CARLO SIMULATOR - VERTIGO .....	61
4.1 Previous Work on QWIP Modeling/Simulation .....	61
4.1.1 Analytical Models .....	63
4.1.2 Self-Consistent and Numerical Models .....	64
4.2 VERTIGO – The QWIP Ensemble Monte Carlo Simulator .....	66
4.2.1 Wavefunction Calculation.....	66
4.2.2 Simulated Device Structures and Material Parameters.....	68
4.2.3 Simulation Approach .....	71

4.2.4 Electrostatic Calculations, Initial Conditions, and Boundary Conditions.....	72
4.2.5 Calculating Particle Trajectory and Ensemble Parameters .....	74
4.2.6 Heterojunction Treatment .....	75
4.2.7 Tunneling at Emitter and X valley Barrier.....	76
4.2.8 Electron Scattering.....	77
4.2.9 3D Electrons in the Quantum Well Region .....	78
4.2.10 2D Electrons in the Quantum Well Region .....	78
5. SIMULATION RESULTS AND DISCUSSION .....	81
5.1 Band Profile and Electric Field Domain Formation .....	81
5.2 Barrier Electron Velocity .....	84
5.3 Electron Capture.....	88
5.4 QWIP Gain.....	90
5.5 Dependence of Gain, Electron Velocity and Excited Electron Lifetime on QWIP Material Parameters .....	92
5.6 Monte-Carlo Simulation of Transient Characteristics of QWIPs .....	98
5.7 Conclusions.....	104
6. InP BASED LWIR QWIP TECHNOLOGY .....	106
6.1 Previous Work on InP Based QWIPs.....	106
6.2 InP Based QWIP Structures .....	109
6.3 QWIP Device Fabrication .....	112
6.4 Characterization Set-up.....	114
6.5 Characterization Results .....	118
6.6 Low Temperature/Low Background Characterization of InP/InGaAs QWIP .....	129
6.7 Conclusions .....	133
7. InP BASED LWIR QWIP FOCAL PLANE ARRAY PERFORMANCE ...	135
7.1 FPA Fabrication .....	135

7.2 FPA Characterization Set-up.....	137
7.2.1 Camera .....	139
7.2.2 Read-out Integrated Circuit.....	140
7.2.3 FPA Characterization Method.....	144
7.3 Focal Plane Array Performance .....	146
7.4 Conclusions .....	157
8. CONCLUSION AND FUTHER WORK.....	158
REFERENCES.....	162
APPENDICES	
A. MATERIAL PARAMETERS.....	177
B. SOLUTION OF POISSON’S EQUATION.....	182
C. SCATTERING RATES .....	184
D. MOMENTUM CALCULATION AFTER SCATTERING .....	195
CURRICULUM VITAE .....	198

# CHAPTER 1

## INTRODUCTION

Infrared (IR) photodetector technology, being driven mostly by military, metrology and telecommunications applications, is one of the major branches of optoelectronics technology. Starting with mercury thermometers, infrared photodetectors evolved through bolometers, elemental semiconductors, and compound semiconductors in the last century. Finally, nature's limitations are being eliminated by engineered bandgap photodetectors, namely quantum well infrared photodetectors (QWIP) [1], superlattice photodetectors, and quantum dot infrared photodetectors (QDIP).

### 1.1 Scope

Quantum well infrared photodetectors (QWIPs) have emerged as potential alternatives to conventional infrared detectors utilizing low bandgap semiconductors [1]. The most important advantage provided by the QWIP is the relatively mature material and processing technology. Tunable spectral band, radiation-hardness, and the possibility of monolithic integration with the peripheral electronics are among the other advantages [2]. Recently, various groups [3–6] have reported large format focal plane arrays, noise equivalent temperature difference less than 10 mK and high detectivity at 77 K. For further improvement in the



QWIP technology, different material systems and design approaches are being investigated.

There has been a large amount of experimental and theoretical work toward a better understanding of QWIP operation; however, there is still lack of knowledge on this issue. Even though the device is a unipolar photoconductor with a fairly simple layer structure, precise QWIP modeling is a difficult task. While the transport of the continuum electrons needs sophisticated models due to far from equilibrium conditions and the reflection of electrons at the quantum well (QW) locations, an accurate description of the capture and emission mechanisms requires the realistic evaluation of the rates of carrier scattering between two-dimensional (2D) states, together with scattering mechanisms between two- and three-dimensional (2D $\leftrightarrow$ 3D) states. The shortcomings of the previous models, as described in Chapter 3, call for a more detailed model/simulator to achieve a better understanding of QWIP, which is a device whose operation depends on a combination of complicated mechanisms.

With the above motivation, this Ph.D. study focuses on understanding the QWIP behavior through detailed simulations. Following these studies, InP based QWIP photodetectors and focal plane arrays are fabricated and characterized for performance assessment as well as verifying the theoretical work. The scope of the thesis can be divided into two parts.

- (a) Monte-Carlo simulation is an invaluable method to simulate semiconductor devices. As an alternative to analytically formulating a complex semiconductor device, simulating ensemble of electrons gives very important results in terms of device operation, especially for devices where electrons see sharp potential differences and quantum effects. In this Ph.D study, a very detailed Monte-Carlo simulation is coded and applied to QWIPs. As to our knowledge, the simulator reported in this thesis has been the most detailed work reported for QWIPs. The main difference between this simulator and those reported previously is the level of detail

incorporated into the simulator. Both 3D and 2D electrons are simulated by taking size quantization into account in both  $\Gamma$  and L valleys of the conduction band. The rates of the presumably dominant 2D and  $2D \leftrightarrow 3D$  scattering processes are calculated using the wavefunction solutions of the Schrödinger equation. Dependence of electron transport on various QWIP parameters is investigated and the phenomena related to electron transport in QWIP is cleared. While complementing the previous work, the results offer a deeper understanding of some important QWIP characteristics by resolving the details of transport and electron dynamics in the device.

- (b) QWIP technology emerged with the AlGaAs/GaAs material system, which resulted in many demonstrations of QWIPs known as “standard QWIP”. In order to investigate the feasibility and advantages of QWIPs with other material systems, QWIP focal plane arrays (FPA) with InP/InGaAs and InP/InGaAsP material systems are fabricated and characterized. High quality thermal imaging with these QWIPs is demonstrated. In addition, advantages of InP based QWIPs over the standard QWIP technology are presented. It is concluded that, in high noise, or low temperature, or low background flux environments, the InP based QWIP technology offers better characteristics than standard QWIPs.

In the rest of this chapter, the fundamentals of infrared sensing is summarized. After this introduction, Chapter 2 explains QWIP operation and characteristics. Information on focal plane arrays and performance parameters are discussed in Chapter 3. Chapter 4 summarizes earlier QWIP modeling work and gives details of the developed QWIP Monte-Carlo simulator. Chapter 5 includes discussion of the QWIP Monte-Carlo simulation results. Chapters 6 and 7 reports detailed characteristics of the fabricated QWIP sensors. Finally, Chapter 8 contains conclusion and further work.

## 1.2 Infrared Radiation

The frequency of infrared radiation extends between the visible red and the millimeterwave/microwave band. Thermal imaging is usually performed through sensing the infrared radiation in the mid wave infrared (MWIR) and long wave infrared (LWIR) bands which lie in the 3-5  $\mu\text{m}$  and 8-12  $\mu\text{m}$  wavelength intervals. These intervals are called atmospheric windows, since atmosphere is almost transparent to electromagnetic radiation in these bands. Figure 1.1 shows atmosphere's infrared transmission characteristics [4].  $\text{H}_2\text{O}$  and  $\text{CO}_2$  are the important gas molecules that absorb infrared light in the atmosphere.

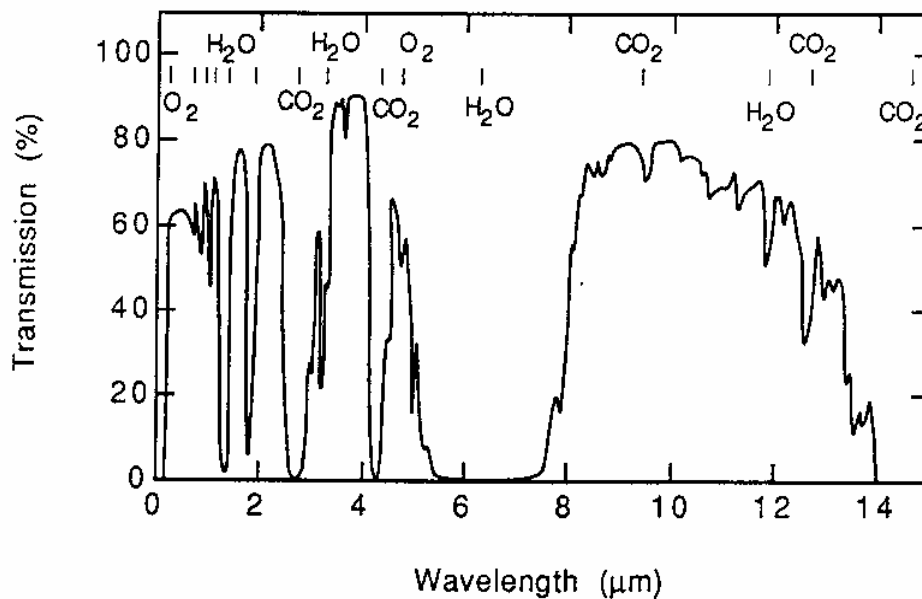


Figure 1.1 Transmission spectrum of atmosphere along 2km path at sea level, where precipitable water height is 14mm [4].

Every object above 0 K emits infrared radiation. For an ideal blackbody, the radiant emittance spectrum can be expressed by Planck's Law

$$M_e = \frac{1}{\lambda^5} \frac{2\pi hc^2}{\exp\left(\frac{hc}{\lambda kT}\right) - 1} \quad \text{W}/\mu\text{m} \cdot \text{m}^2 \quad (1.1)$$

where  $h$  is the Planck constant,  $c$  is the speed of the light,  $k$  is the Boltzman constant,  $\lambda$  is the photon wavelength, and  $T$  is the blackbody temperature. The shape of the above distribution is shown in Figure 1.2. It is seen that room temperature objects' emittance spectrum peaks at 10  $\mu\text{m}$ , which lies in the LWIR band. Hotter objects' emittance peak lies in shorter wavelengths, where MWIR detectors may be used for detection. The thermal contrast, which can be defined as the ratio of the derivative of the flux with respect to background temperature, to the flux level is higher in MWIR band.

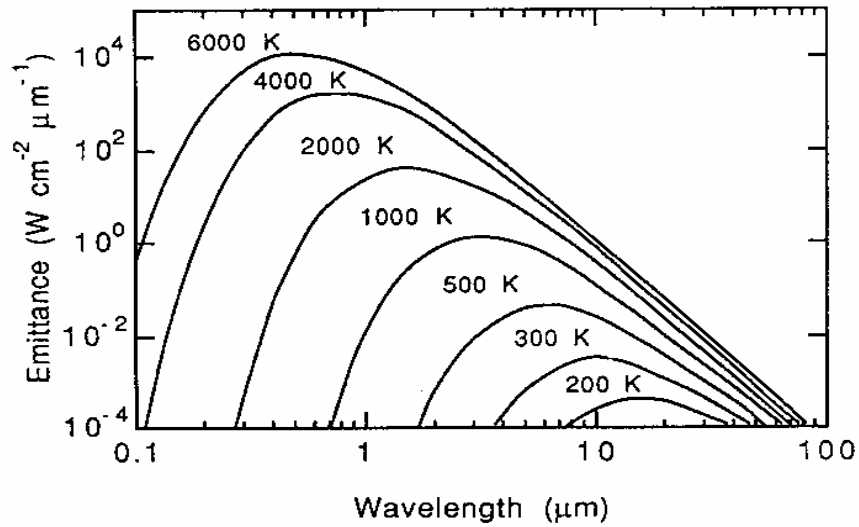


Figure 1.2 Spectral emittance of an ideal blackbody at different temperatures [4].

### 1.3 Detecting Infrared Light

Infrared light carries much of the power emitted from a blackbody at room temperature. Either the emitted photons, or the photon transferred heat may be utilized to detect the IR power. IR detectors are classified according to these quantities that they measure:

- Photon Detectors (Examples: photoconductors and photodiodes)
- Thermal Detectors (Examples : Bolometers and ferroelectric detectors)

Most of the LWIR photon detectors are cryogenically cooled detectors due to the high concentration of thermally generated electrons at room temperature. This chapter introduces the LWIR photon detector family, which includes the QWIP. Thermal detectors show significant advancements in the last decade, and an extensive review may be obtained from the literature [5].

In conventional photoconductors and photodiodes, the detection mechanism relies on the generation of free carriers in a nearly intrinsic material by photoexcitation. If the incident photons generate electrons and holes through band to band photogeneration, the photoconductor is called intrinsic. The detector sweeps these excess carriers out into the circuit by the help of an external bias. The cutoff wavelength of the intrinsic photoconductor is determined by the energy bandgap of the semiconductor. The relation can be expressed as  $E_g = hc / \lambda$ , or numerically  $E_g = 1.24 / \lambda$  where the unit of  $\lambda$  is micrometers and the unit of  $E_g$  is eV. The major problem associated with infrared detection is that long wavelength photons require a small bandgap. As evident from energy bandgap calculations, the semiconductor bandgap tends to decrease with increasing atomic spacing of the crystal (Figure 1.3). The final result is that materials with larger inter-atomic distances tend to show weaker mechanical properties together with technological

problems in the synthesis of their crystals uniformly. This is the reason behind the technological challenge in fabrication of LWIR photodetectors.

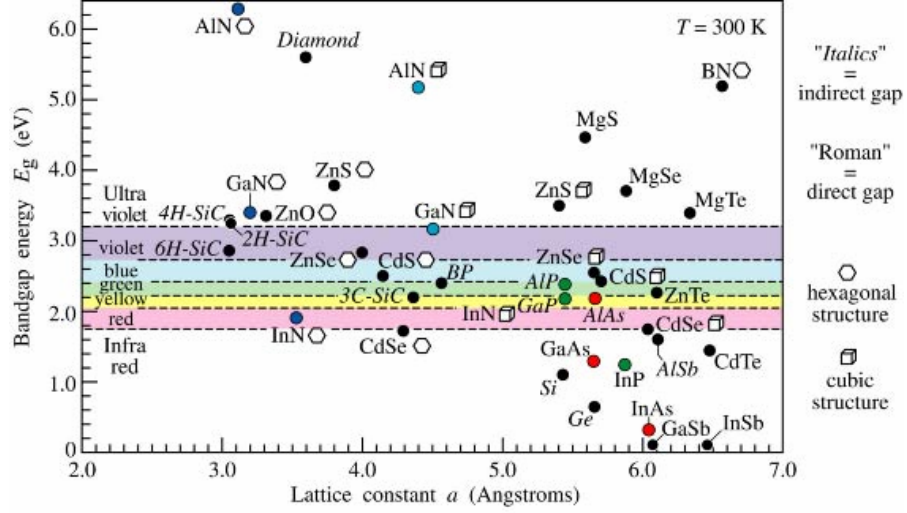


Figure 1.3 Energy bandgap vs. atomic spacing for various crystals [4].

### 1.3.1 Photoconductive Detectors

In a photoconductor, the detector is an intrinsic material with bandgap set to the energy of the wavelength of photons to be detected. Applying bias to the detector sweeps the photo-generated carriers out into the circuit. The cutoff wavelength of the device is determined by the energy bandgap of the semiconductor. Figure 1.4 shows the conceptual band profile of the device under operating bias. The photoexcited carriers are collected at one terminal and the new ones are injected at the other terminal. The ratio of the lifetime to the drift-time of the carriers determines the factor of contribution of each carrier into photocurrent and is called photoconductive gain. Conventional intrinsic photoconductors suffer from large dark current, which makes it impossible to use them in a large-format focal plane arrays due to high power consumption.

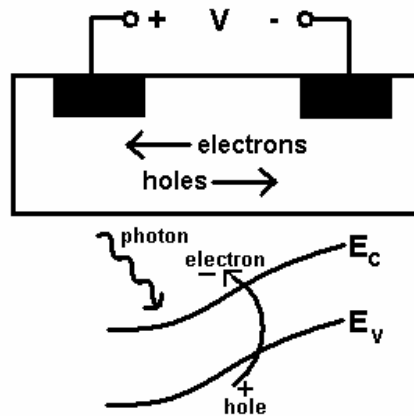


Figure 1.4 Device structure and energy band profile of a conventional photoconductor under operating bias.

Extrinsic photodetectors utilize the transition of carriers between a localized dopant state and the nearest band. For example, Ga in Si host crystal forms a localized state near the band edge. Incoming photon excites the electron in the Ga site and the material operates like a low bandgap material. Materials such as Si:Ga, Si:As, and Si:Sb are used in astronomy oriented applications to detect LWIR photons and photons with wavelength longer than 14  $\mu\text{m}$ . However, shallow impurities require stringent cooling requirements, and they can not offer tactical field operation in FPA format.

As an alternative to the above described low bandgap materials or extrinsic detectors, quantum well infrared photodetectors detect infrared radiation through the transition of carriers between the artificially generated states. QWIPs take the advantage of utilizing technologically mature larger bandgap materials to create artificial low energy bandgaps to detect infrared radiation. A low bandgap material layer stacked between two large bandgap material layers creates a quantum well. The quantized states in the quantum wells can have energy separation corresponding to infrared photon energy. Utilizing these quantized states for photodetection is possible with stacked multi-quantum well (MQW) structures

(Figure 1.5). Incident photons excite carriers from a low energy state to higher energy states, and the contribution of the excited carriers to conduction generates the photocurrent. QWIP is a multi quantum well structure with suitable contact and light coupling geometry. QWIPs are vertical transport devices that are usually processed as vertical mesa diodes suitable for large format focal plane array fabrication. Details of QWIP operation is given in Chapter 2.

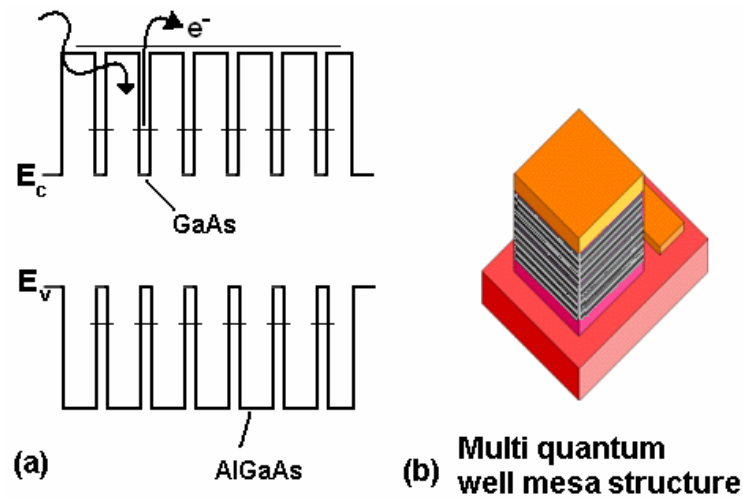


Figure 1.5 Example of constructing multi quantum well structure using different bandgap semiconductors (a). Growing multiple periods allows forming the multi quantum well structure in mesa form (b).

### 1.3.2 Photovoltaic Detectors

Photoconductors need external bias voltage, which results in excessive dark current. Large dark current not only increases the noise of the detector, but also makes the detector unsuitable for some read-out mechanisms. Photovoltaic detectors utilize their own built in electric field to sweep out photocarriers to the contacts. Semiconductor p-n junction is the most widely used photovoltaic detector, and it is



called photodiode. Infrared light can be detected with photodiodes made from low bandgap semiconductors such as InSb and HgCdTe. Inserting an intrinsic layer between the p and n layers can increase optical absorption of the device. Such a device is called p-i-n photodiode. Most important problems of IR photodiodes are related with the epitaxial growth problems, and the weak mechanical properties of the low bandgap semiconductors. Their performance is limited with the carrier traps, recombination-generation centers and tunneling leaks.

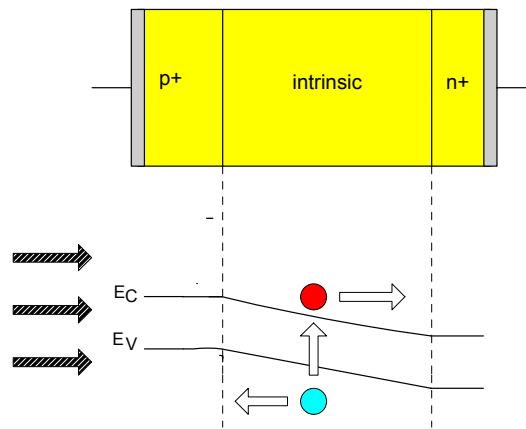


Figure 1.6 Simplified device structure, and the energy band diagram of photovoltaic pin photodetector.

QWIPs can also be designed to work in photovoltaic mode to show nonzero responsivity at zero bias voltage [6,7]. Photovoltaic QWIPs are well suited for applications requiring low dark current. They suffer from low responsivity, and external system noise, but take the advantage of long integration time due to minimal photocurrent with minimal photoconductive gain.

Inspired from QWIP technology, another “artificial bandgap” photodetector technology is type-II superlattice photodetectors. InAs/(GaIn)Sb material system is used for both MWIR and LWIR bands. This technology allows higher operation temperature than QWIP at the same wavelength band. An example device structure

is shown in figure 1.7. Type II identifies non-overlapping bandgaps. Hence in the even and odd layers in the superlattice, there are quantized states in the valance band and conduction band respectively. Ideally there is no overlap between these states' wavefunctions however thin layers allow a small overlap to allow absorbtion of a photon with minimal dark current. Hence, very small separation between the states can be tuned to detect desired wavelength. This structure can be doped with different type dopants through the superlattice and can be utilized as a p-i-n structure [8].

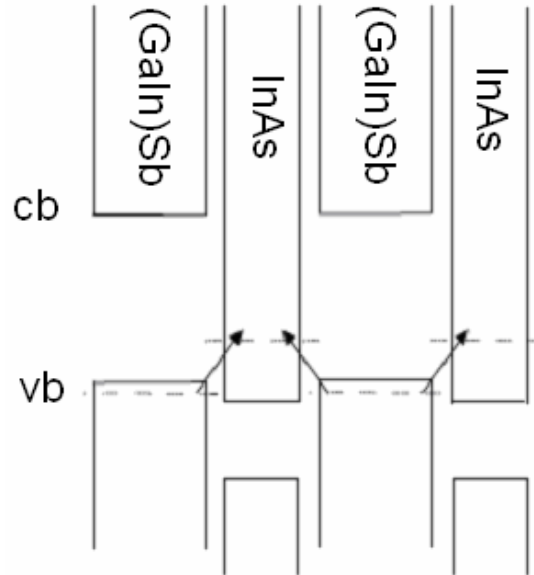


Figure 1.7 Type II superlattice bandgap diagram. Absorbed photons causes electron transfer between the states in the arrow direction [8].

## **1.4 Infrared Photodetectors for Thermal Imaging**

There are different methods to utilize an infrared photodetector for thermal imaging. The simplest, yet technologically most challenging arrangement is photodetectors arranged in a two dimensional array. When such an array is placed at the focal plane of an optical focusing system, signal from each photodetector gives measure of photon emission intensity from the point in the scene. Such an array of photodetectors is called focal plane array (FPA). Fabricating the photodetectors in 1D array and utilizing a scanning mirror is also possible for thermal imaging. If the material technology does not allow large 2D array, 2 dimensional scanning mirrors can scan a scene and temporal signal from the photodetector can be used to form an image (Figure 1.8).

In LWIR region, fabricating large area 2D FPAs is technologically challenging due to material and processing nonuniformities. Other challenge is to obtain interconnections from each pixel. This is usually handled by indium bump hybridization technique to connect a detector array to a read-out circuit array (Figure 1.9). With this architecture there are conductive bumps placed on each pixel which act as interconnect between the detector die and signal multiplexing circuit. This circuit, read-out integrated circuit (ROIC), has a built-in analog multiplexer to send the signal serially to external electronics.

The need for large format, multi-color focal plane arrays is among the major drivers of the current infrared photodetector research studies where QWIP technology offers an important advantage. Other advantages of QWIPs are given in chapter 2 together with information about characteristics and operation of QWIP.

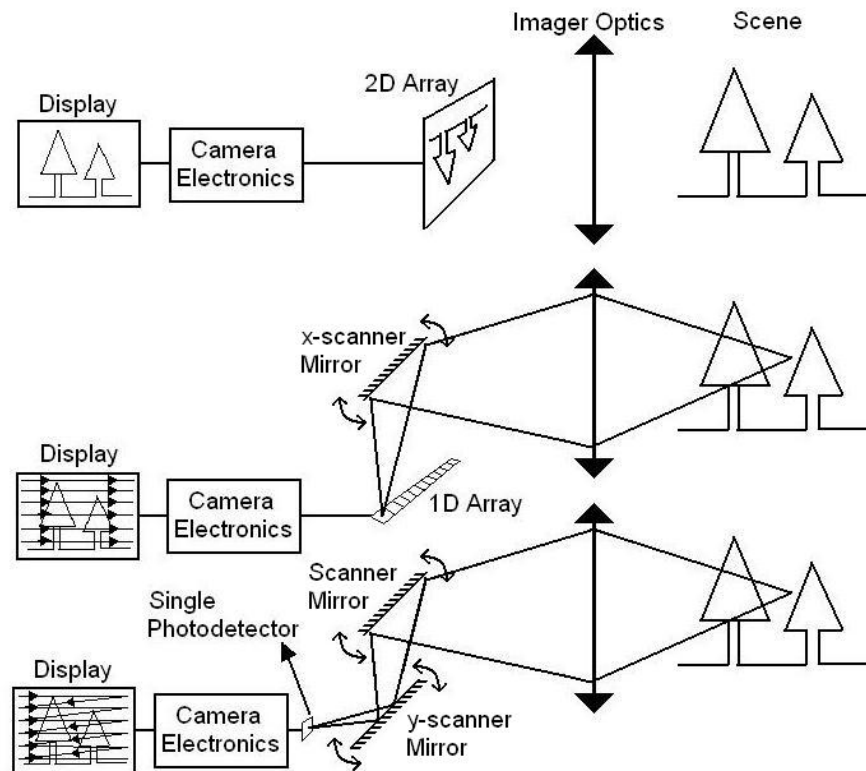


Figure 1.8 Illustration of 2D array staring, 1D array scanning, and single photodetector scanning thermal imaging systems.

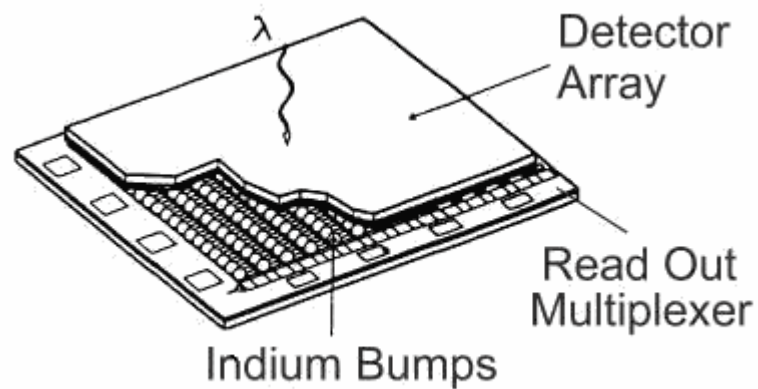


Figure 1.9 Detector focal plane array coupled to a read-out integrated circuit via an indium bump array.[9]

## CHAPTER 2

### QUANTUM WELL INFRARED PHOTODETECTORS

Intersubband transition in a GaAs-AlGaAs quantum well is first reported by West and Eglash in 1985 [10] . Since then, there has been significant effort to make this suitable lattice matched material system useful for infrared detection. In fact, intersubband absorption in semiconductors were also observed and suggested in structures like modulation doped field effect transistor (MODFET) and metal oxide semiconductor (MOS) structure, however they remained in far infrared region (FIR) instead of the technologically important long wave infrared region (LWIR) [11]. First QWIP demonstration and high performance QWIP detectors in LWIR band were reported by Levine *et. al.* in 1989 [12-14]. Fabrication of high performance focal plane arrays followed these in 1991 [2,3].

This chapter summarizes the QWIP physics and characteristics, as well as a comparison of QWIPs with the HgCdTe detectors for LWIR imaging applications.

#### 2.1 QWIP Operation and Characteristics

QWIP is mainly used as a photoconductor. Incident photons excite electrons from their bound states into continuum states, hence cause change in number of mobile carriers and current (Figure 2.1). Each photoexcited electron either reaches the

collector contact or is captured by a quantum well. QWIP operates by exchange of photoelectrons between the quantum wells and contacts.

The electronic bound and continuum states, for photoexcitation are created artificially by building quantum wells using closely spaced semiconductor heterojunctions. The peak response wavelength of QWIP can be tuned by varying quantum well width and depth. [1,15]

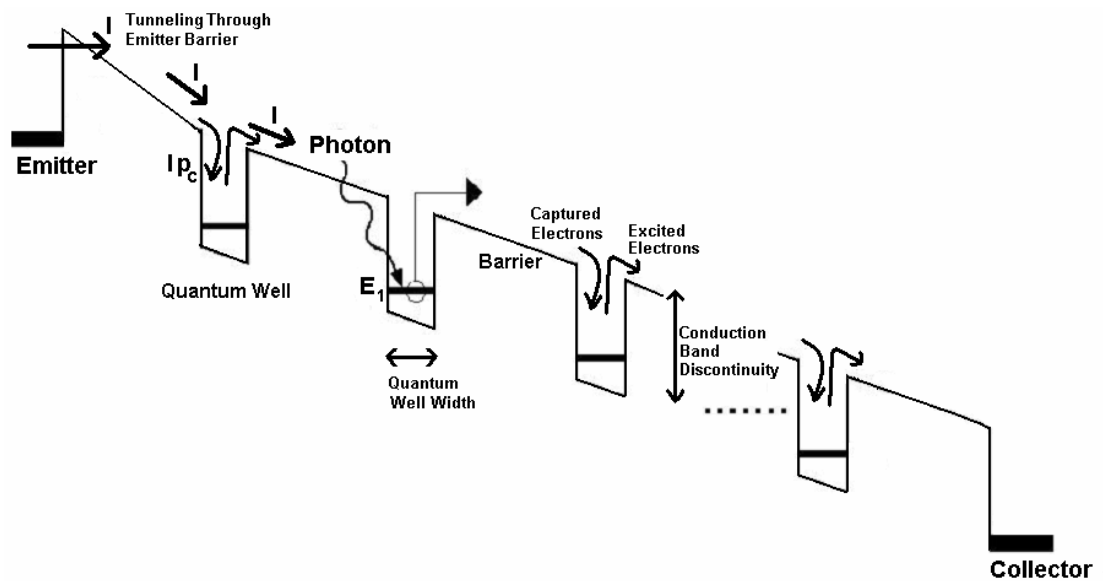


Figure 2.1 Operating principle of QWIP

### 2.1.1 Intersubband Transitions in Quantum Wells

Electrons in quantized states of a semiconductor quantum well can absorb electromagnetic radiation, and be excited to higher states. The total rate of electron intersubband transition due to photon absorption can be calculated by Fermi's golden rule and an appropriate interaction potential [16],

$$W = \frac{2\pi}{\hbar} \sum_{f,i} |M|^2 f_i (1 - f_f) \delta(E_f - E_i - \hbar\omega) \quad (2.1)$$

where,  $f_i$  and  $f_f$  are the occupancy probability of initial and final states,  $\hbar\omega$  is the photon energy,  $E_i$  and  $E_f$  are initial and final state energies, and  $M$  is the matrix element given as

$$M = \frac{e}{m} \left( \frac{\phi \hbar}{2\epsilon_0 n_r \omega c} \right)^{1/2} (\delta_{k_{xy}} \delta_{k_{xy}}) \sin \theta \langle \psi_{z,n} | p_z | \psi_{z,n} \rangle \quad (2.2)$$

In this expression,  $\theta$  is the angle of incidence of the photon to the quantum well plane,  $n_r$  is the material refractive index,  $m$  is the electron effective mass, and  $\omega$  is the photon angular frequency. It is seen that the transition rate depends on  $|M|^2 \approx \sin^2 \theta$ . In other words, light normally incident to the quantum well plane ( $\theta=0^\circ$ ) has zero absorption probability. This is called polarization selection rule and can be restated as "optical intersubband transitions associated with a single spherical band are induced by light polarized in the quantum well direction" [16].

### 2.1.2 Standard QWIP Conduction Band Structure

The standard QWIP, is an AlGaAs/GaAs MQW structure intended for LWIR thermal imaging. Depending on the specific features of the application, the device parameters are chosen in the ranges given below [1,11].

GaAs quantum well width : 40Å - 50Å

AlGaAs barrier width : 300Å - 500Å

Al mole fraction : 0.25 - 0.3

Doping : n-type  $10^{17} \text{ cm}^{-3}$  -  $2 \times 10^{18} \text{ cm}^{-3}$

Number of periods : 20 - 50

The main features of the conduction band profile of a standard QWIP is shown in Figure 2.2. Intersubband transitions in the  $\Gamma$  valley quantum well are used for

photodetection. Arrows in the figure indicate the important current mechanisms. In the GaAs quantum well regions, the L and X valleys form quantum wells and quantum barriers, respectively.

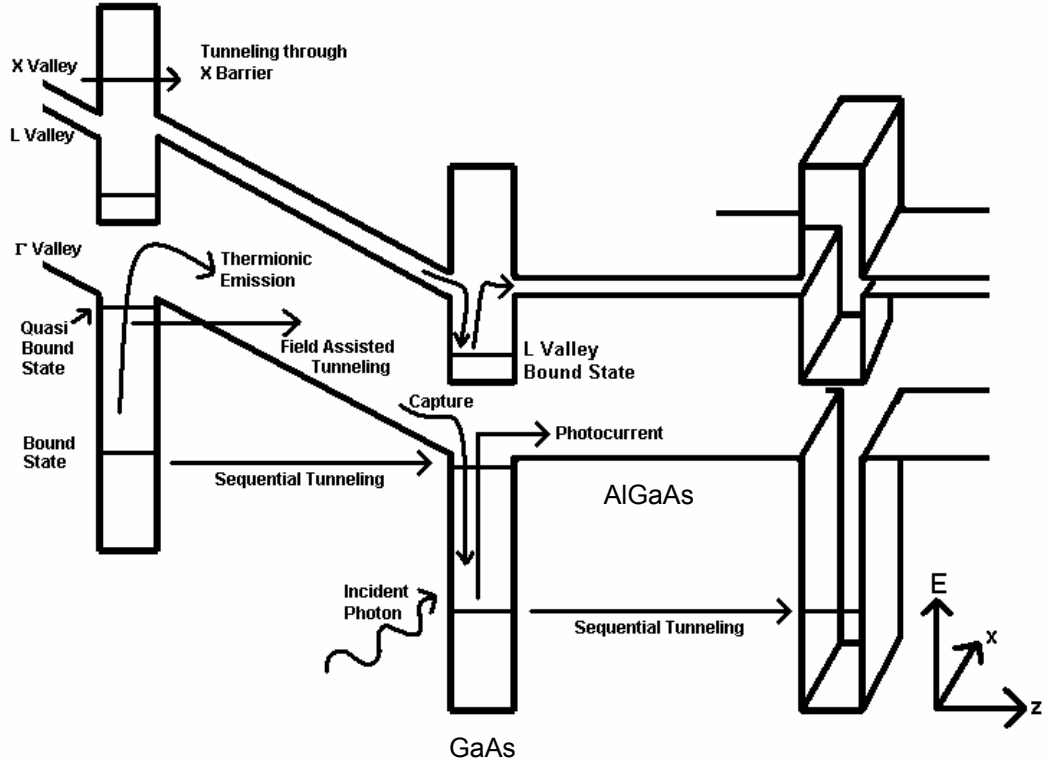


Figure 2.2: Main features of the conduction band of a standard AlGaAs/GaAs QWIP, E axis represents energy of electron in conduction band, z represents layer growth direction, x represents a direction parallel to quantum well plane.

### 2.1.3 Dark Current

QWIP is a MQW device, and its i-v characteristics can be modeled by compiling various current mechanism models such as thermionic emission from quantum wells, tunneling at emitter contact, photoexcitation, field assisted tunneling at the quantum wells and sequential tunneling [1]. Figure 2.2 illustrates these current



components in the device. At typical operation temperature range of 65K-77K, thermionic emission, photoexcitation and tunneling current at the emitter barrier are the dominant current mechanisms to be modeled in standard QWIP structures [1].

Typical AlGaAs/GaAs QWIP i-v behaviour displays a strong increase in device current until an electric field of 10 kV/cm due to accelerating electrons, and then the current nearly saturates due to complicated capture/escape balance [17]. The dark current density versus bias voltage plot of a typical 50-well  $\text{Al}_{0.25}\text{Ga}_{0.75}\text{As}/\text{GaAs}$  QWIP under various temperatures is given in Figure 2.3 [14]. The detector has 305Å thick barriers and 40Å wells which are n-type doped at a density of  $1.4 \times 10^{18} \text{ cm}^{-3}$ . Dark current of bound-to-continuum QWIPs depends strongly on doping and peak responsivity wavelength of the device [15,18]. As the peak responsivity wavelength decreases, the thermal energy barrier seen by the bound electrons decreases, hence thermionic emission rate from QWs increases. Dark current due to thermionic emission changes according to the following simple relation [19]

$$I_{th} = \frac{e^2 m^*}{\pi \hbar^2} \frac{A v_D}{L_w} \Delta_1 \exp[-(E_b - e\Delta_2 - E_F - E_1)/kT] \quad (2.3)$$

where,  $E_b$  is the barrier height,  $E_1$  is the subband energy level,  $\Delta_1$  is the potential drop across one barrier,  $\Delta_2$  is the potential across one well,  $A$  is the area of the device,  $m^*$  is the effective mass, and  $L_w$  is the well width. The temperature dependence of dark current is also very strong as seen in figure 2.3. In LWIR imaging applications, optimizing the peak wavelength to obtain dark current density at the order of  $0.1 \text{ mA/cm}^2$  is an essential part of QWIP design. This not only reduces the noise of the detector, but also allows longer integration times with a direct injection read-out integrated circuit cell as will be explained in chapter 3. [20].

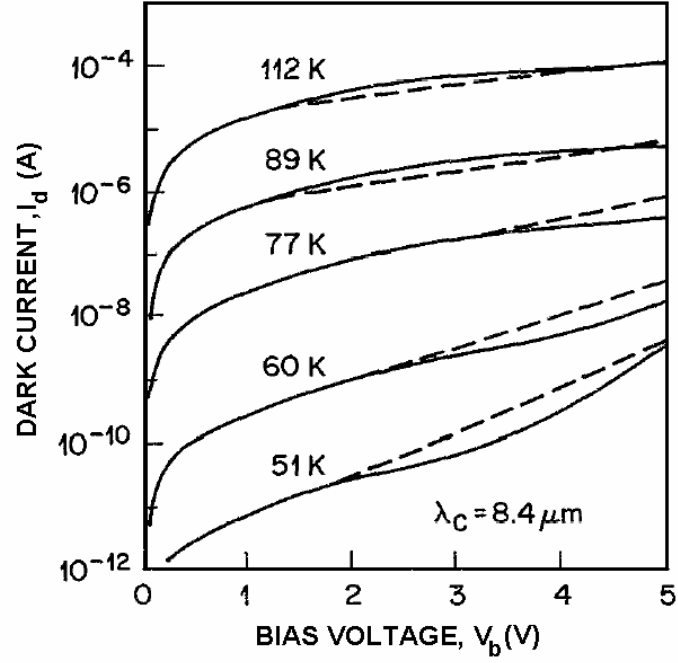


Figure 2.3 Dark current of AlGaAs/GaAs standard QWIP at various temperatures. Diode mesa diameter is 200  $\mu\text{m}$  [14].

#### 2.1.4 Responsivity and Photoconductive Gain

QWIP responsivity can be defined in terms of the detector parameters as

$$R = \left( \frac{e}{h\nu} \right) \eta g_p p_e \quad (2.4)$$

where,  $g_p$  is the optical gain,  $p_e$  is the escape probability of a photoexcited electron from quantum well into conduction without being recaptured,  $\eta$  is the absorption quantum efficiency, and  $h\nu$  is the photon energy of the incident monochromatic radiation. Photoconductive gain of QWIP is defined in a way similar to that of the conventional photoconductors

$$g_p = \frac{v\tau_L}{l} = \frac{\tau_L}{\tau_T} = \frac{L}{l} \quad (2.5)$$

where  $v$  is the average electron drift velocity,  $\tau_L$  is the excited electron lifetime,  $l$  is the device length,  $L$  is the photoexcited electron mean free path, and  $\tau_T$  is the device transit time of the electron [1]. In other words, optical gain is the ratio of the electron's drift distance to the device length. Longer electron mean free path means larger optical gain, hence greater responsivity. Typical responsivity vs. bias dependence of standard QWIP is shown in Figure 2.4. It is seen that responsivity of standard AlGaAs/GaAs QWIP tends to saturate at medium bias voltages.

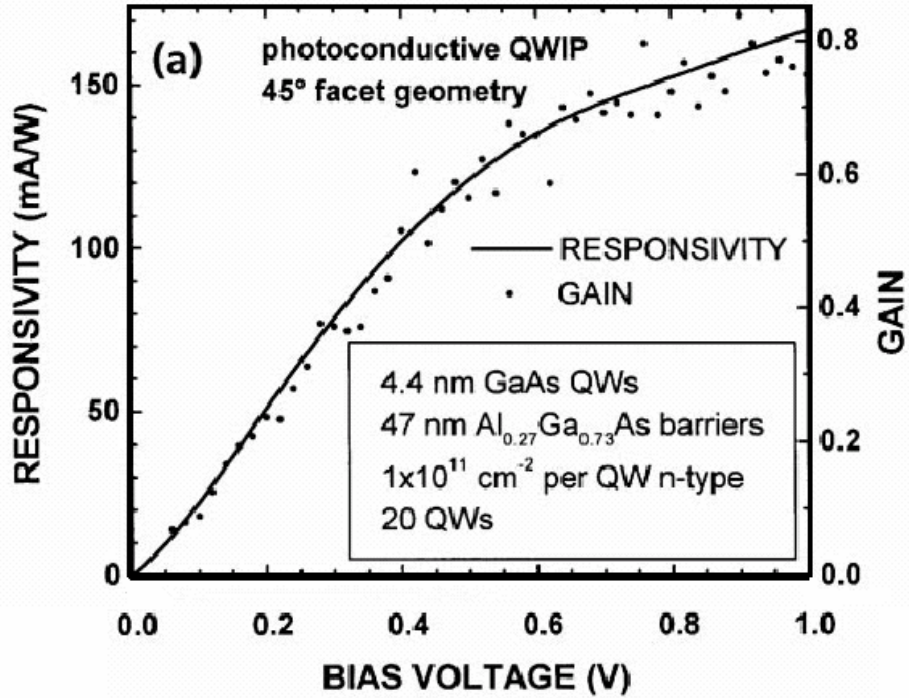


Figure 2.4 Responsivity vs. bias and noise gain vs. bias characteristics of a standard 9.3  $\mu\text{m}$  cutoff QWIP [21].

### 2.1.5 Noise and Noise Gain

The dominant noise mechanism in QWIP is the generation-recombination (GR) noise, which is due to fluctuations in number of mobile carriers as a result of the random photoexcitation and capture of photoelectrons [22]. GR noise current power in a photoconductor can be expressed as

$$i_{GR}^2 = 4eI_{DC}g_n\Delta f \quad (2.6)$$

where  $e$  is the electron charge,  $g_n$  is the noise gain,  $I_{DC}$  is the average current flowing through the photoconductor, and  $\Delta f$  is the measurement bandwidth. On the other hand, fluctuations in the velocity of the carriers create Johnson noise, whose noise current power is expressed as  $i_J^2 = 4kTG\Delta f$ , where  $T$  is the detector temperature, and  $G$  is the differential conductance of the QWIP. For standard QWIPs, GR noise is usually the dominant noise mechanism.

GR noise can be related to capture probability ( $p_c$ ) of the photoexcited electrons by expressing gain in terms of capture probability. Liu used the current continuity in the device and contribution of each well to the photocurrent to reach the following approximate expression [23] for the QWIP gain,

$$g_n = \frac{1}{Np_c} \quad (2.7)$$

where  $N$  is number of quantum wells in QWIP, and  $p_c$  is the capture probability at a single quantum well. Dependence of  $g$  on  $1/N$  is experimentally verified [23]. In derivation of the above expression, each quantum well is assumed to have the same  $p_c$  value. In this thesis study, dependence of  $p_c$  on bias and on location of quantum well is presented. This dependency in the literature has been estimated indirectly with experiments [1]. Based on other assumptions, relation of  $g_n$  and  $g_p$  is also investigated in the literature. As shown in figure 2.5, it has been observed that  $g_n \cong g_p$  for bound to continuum QWIPs [24].

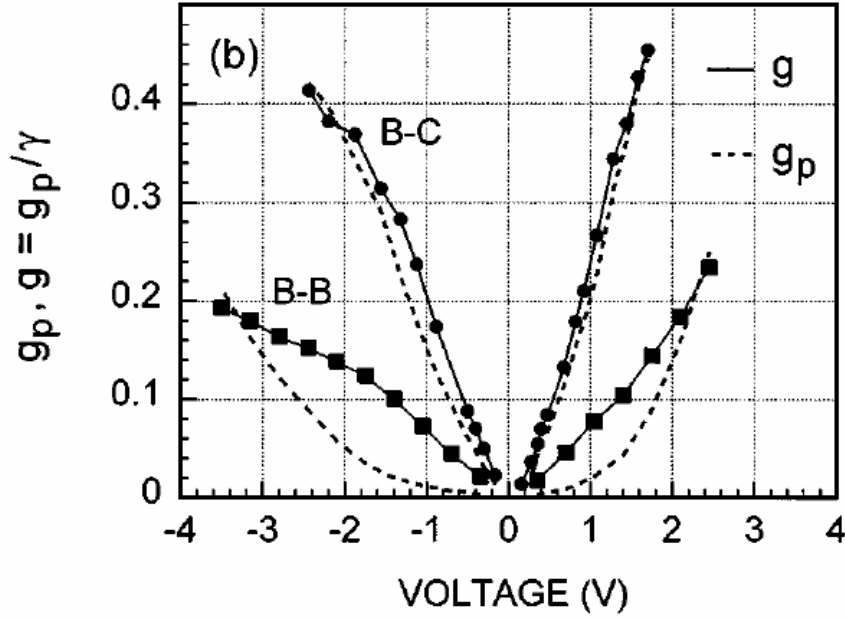


Figure 2.5 Experimental measurements of noise gain,  $g_n$  (shown as  $g$  in the plot) and photoconductive gain,  $g_p$  in bound-to-bound (B-B) and bound-to-continuum (B-C) QWIPs. [24]

### 2.1.6 Detectivity

Detectivity is the signal-to-noise ratio normalized to detector area and measurement bandwidth. Detectivity is an important figure of merit for an infrared detector. Although various noise mechanisms can be included in detectivity calculation, GR noise alone can determine the standard QWIP performance,

$$D^* = \frac{R\sqrt{A\Delta f}}{i_n} = \frac{(e/h\nu)\eta g_p p_e}{\sqrt{4eJ_{DC}g_n}} \quad (2.8)$$

In the above expression,  $J_{DC}$  is the DC current density in the device. It is seen that maximizing  $D^*$  involves dealing with a complex relation between the electrical parameters;  $J_{DC}$ ,  $g_p$  and  $g_n$  [25,26]. Levine *et.al* [14,27] suggests maximizing  $g_p$

using bound-to-continuum QWIPs to benefit from the high signal level, and Schneider *et.al.* [6,25,26] suggests minimizing  $g_n$  using photovoltaic QWIPs in order to reach higher  $D^*$ , and to reach long integration times in imaging applications. Both of the methods rely on controlling gain parameters of the QWIP, which depends on the details of transport properties.

### 2.1.7 Light Coupling

Detectivity of QWIP can be increased by increasing absorption quantum efficiency, which needs improved light couplers. As mentioned above, electrons confined in a 2D quantum well do not respond to photons whose electric field vector is in the plane of quantum well. Because the electrons are confined in the direction of growth and quantization of energy levels is associated in that direction only. There are several methods to increase coupling of photon electric field with the bound electrons (Figure 2.6). The simplest one is coupling light through a  $45^\circ$  etched faced into the substrate that constitutes a waveguide [3]. Another method is etching diffraction gratings onto the QWIP mesa to diffract normally incident radiation passing through the substrate. The grating pattern can be periodic or random, and the feature size should be tuned to the peak detection wavelength [28]. Diffraction gratings can also be etched through the backside of the detector after substrate removal. Such couplers are demonstrated in focal plane arrays and are given the name “enhanced-QWIP (E-QWIP)” [29].

Choi *et. al.* suggested corrugated QWIP (C-QWIP) [30] structures which have etched corrugations on top of the detectors. Removing the detector substrate also improves quantum efficiency of a single mesa, since it helps to confine the photons into the mesa by total internal reflection. Effect of optical couplers is rarely included in modeling electron transport in QWIP due to low quantum efficiency of the wells.

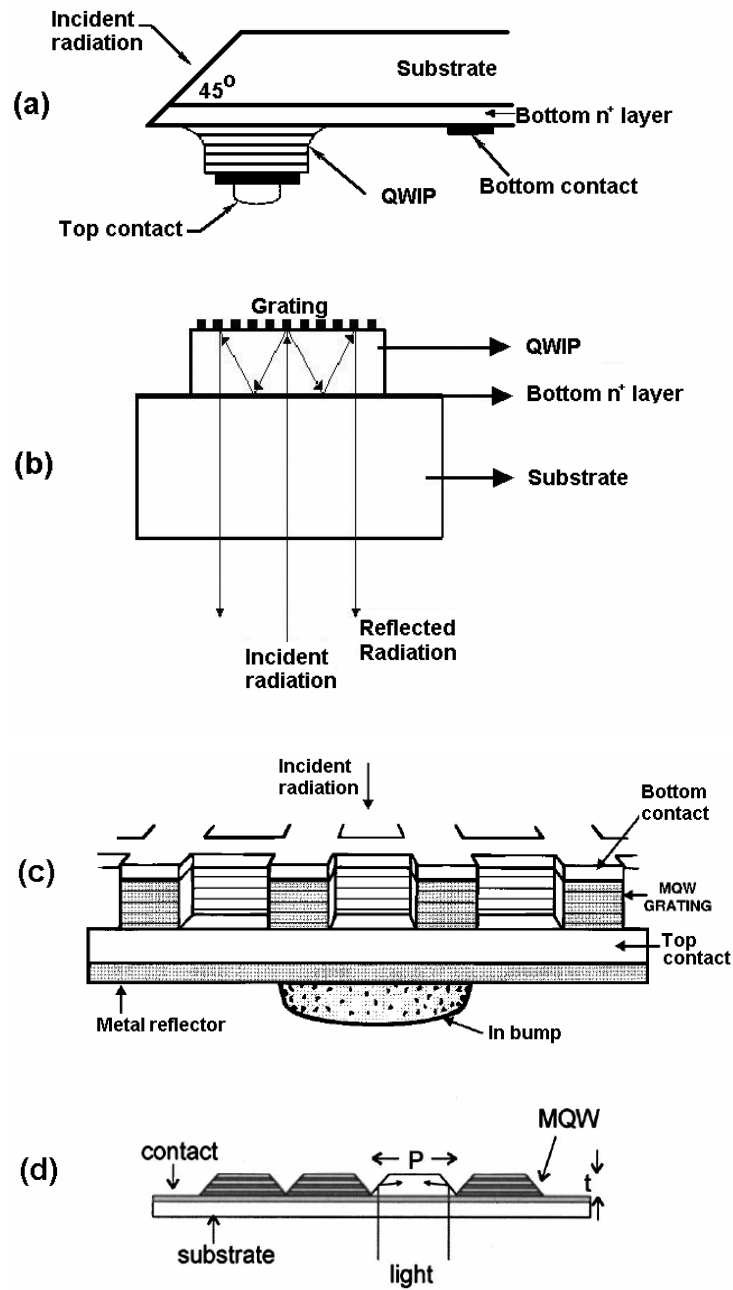


Figure 2.6 Different light coupling methods to QWIP : (a) 45° facet coupling, (b) grating coupling, (c) enhanced QWIP, (d) corrugated QWIP. [3, 28-30]

## **2.2 Material Systems for n-type QWIPs**

In the literature, many different semiconductor material systems for QWIPs are reported [1,11]. They usually follow design principles of the lattice matched AlGaAs/GaAs QWIPs. Bound-to-bound, bound-to-quasibound and bound to continuum QWIPs are successfully demonstrated with the AlGaAs/GaAs material system [12,15,20]. Peak detection wavelength can vary from 4.2  $\mu\text{m}$  up to 19  $\mu\text{m}$  [30-31] with this material system. However, in the MWIR region AlGaAs barrier material suffers from the indirect bandgap with the X valley close the quantum well bound state. Alternative material systems offer flexibility for two color and voltage tunable QWIP applications.

### **2.2.1 AlGaAs/InGaAs**

This is the most widely used material system for MWIR QWIPs on GaAs substrate [33-35]. The strained InGaAs quantum well is sandwiched between AlGaAs barriers. Based on the In mole fraction, the quantum well width should be kept under the critical thickness. Two color FPAs utilizing stacked LWIR and MWIR detectors use AlGaAs/InGaAs structure for MWIR band due to its higher responsivity with respect to AlGaAs/GaAs MWIR QWIPs [35]. The feasibility of InGaAs/GaAs has also been demonstrated for VLWIR QWIPs [36].

### **2.2.2 Ga<sub>0.5</sub>In<sub>0.5</sub>P/GaAs**

Lattice matched Ga<sub>0.5</sub>In<sub>0.5</sub>P/GaAs QWIP on GaAs substrate is an Al free alternative to standard LWIR AlGaAs/GaAs QWIP. The structure is demonstrated with peak responsivity of 0.34 A/W at 8  $\mu\text{m}$  wavelength with a photoconductive gain of 0.86 [37].



### 2.2.3 Other Material Systems

Some examples of QWIPs with different material systems are;  $\text{In}_{0.53}\text{Ga}_{0.47}\text{As}/\text{In}_{0.52}\text{Al}_{0.48}\text{As}$  QWIP on InP substrate at  $4\mu\text{m}$  peak absorption wavelength [36], lattice matched  $\text{InGaAsP}/\text{InP}$  QWIP at  $7.7\mu\text{m}$  response peak [39], and lattice matched  $\text{GaAs}/\text{Al}_{0.5}\text{In}_{0.5}\text{P}$  QWIP at  $3.23\mu\text{m}$  response peak [40]. However, for successful FPA operation these QWIP designs should have low dark current, high responsivity and high uniformity at the same time [1]. Only  $\text{AlGaAs}/\text{GaAs}$  on GaAs,  $\text{InGaAs}/\text{AlGaAs}$  on GaAs, and  $\text{InP}/\text{InGaAs}$  on InP have yet been successfully utilized for QWIP FPAs, apart from this Ph.D study.

## 2.3 QWIP versus HgCdTe Detector and State of the Art

Infrared detection through intersubband transitions in QWs was demonstrated in 1985 [10]. This has been followed by the rapid development of the QWIP technology, and later by Sb based type II superlattice technology. HgCdTe was introduced in 1959 as an infrared photon detector material, and it has been the most widely used material for FPAs working in the LWIR band in the last four decades. Today, HgCdTe technology faces a serious competition by the QWIP technology, for both single and multi-band infrared detection. The superiority of one technology over the other for various applications is still highly controversial.

Photovoltaic HgCdTe detectors, having smaller dark currents, offer higher detectivity, higher quantum efficiency, and higher operating temperature. Typical HgCdTe photodiode quantum efficiency is approximately %50-%60 where typical grating coupled QWIP sensor quantum efficiency is %15. QWIP detectivity rapidly increases with decreasing temperature (an order of magnitude increase for 10 K decrease in temperature below 70 K). Theoretically, HgCdTe detectors yield better

performance down to 50 K in the LWIR band [1]. However, QWIP detectivity and imaging NETD is continuously being improved with new design approaches. Sb based type-II superlattice photodetector is example to this effort. HgCdTe detector detectivity, is limited by material quality. HgCdTe wafers suffer from relatively high defect concentration due to limitations of the CdZnTe substrates and HgCdTe growth technology. Minimum defect concentration reported is on the order of  $10^5 \text{ cm}^{-2}$  [11].

QWIPs are based on III-V based compound semiconductors, which have mature growth and processing technology, and strong mechanical properties. While, it has been argued that the developments in the QWIP technology will saturate due to some physical limitations [1], it is also a fact that QWIP technology is much more open to improvement through new QW structures, material systems and design approaches [11,20].

Noise equivalent temperature difference (NETD) is an important figure of merit for field imaging applications. When a photodetector pixel is exposed to uniform background, the signal difference that can be detected is limited by the temporal noise of the pixel. The temperature difference which generates signal at the noise level is called temporal NETD. Temporal NETD is determined by frame rate and  $D^*$  of the detector, hence by the quantum efficiency which is known to be low for QWIPs. However, for tactical applications, temporal noise is not the dominant noise source. As will be explained in chapter 3 tactical thermal imaging performance is limited by uniformity of the pixel array. Signal variation from pixel-to-pixel results in spatial noise. This spatial noise determines spatial NETD which is a measure of minimum detectable temperature difference between neighboring pixels when they are looking to the same background. It is proposed that NETD of a thermal imaging system is limited by FPA nonuniformity, for detectivity values higher than  $10^{10} \text{ cm.Hz}^{1/2}/\text{W}$ , for 50  $\mu\text{m}$  pixel pitch (Figure 2.7) [1,14]. The nonuniformity on QWIP focal plane arrays can be reduced to %0.01 by signal processing [1,40]. Indeed, AIM reported temporal NETD less than 10 mK

for a 640x512 sized QWIP FPA [7]. Technologically, obtaining high uniformity with staring array HgCdTe is far more difficult.[1].

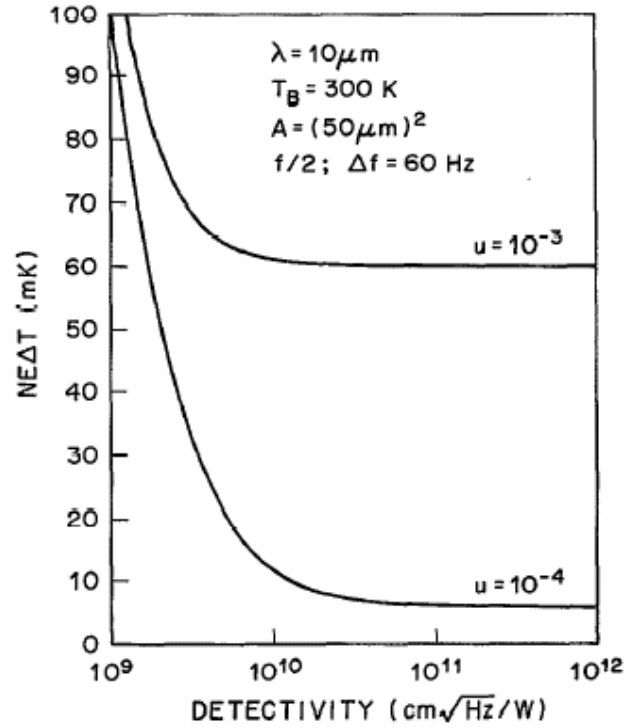


Figure 2.7. Dependence of noise equivalent temperature difference on detectivity and uniformity ( $u$  is the uniformity parameter). [1]

QWIP FPAs yield NETD values close to that of HgCdTe FPAs due to the high FPA uniformity. It is a must to use the QWIP with long integration time to take the advantage of staring array architecture. For tactical applications, this advantage compensates the disadvantage of lower QWIP quantum efficiency. QWIP and HgCdTe cameras are at the same level of performance for applications such as target tracking, target identification, weapon sight and surveillance applications. However, for strategic applications such as space observations and applications

with a low-background, HgCdTe technology can be expected to be superior. Strategic applications demand high detectivity [1].

QWIP is a novel technology, and QWIP performance is increasing continuously [11]. Although HgCdTe FPAs are more widely used today, there is a significant amount of effort to replace HgCdTe FPAs with QWIPs for some applications in order to decrease the cost of thermal imagers. High uniformity and low-cost due to mature III-V technology allows QWIP to compete with HgCdTe technology. HgCdTe photodetectors have low production yield [1,43] and relatively large price/performance ratio at the sensor level (Table 2.1).

Table 2.1: Sensor cost comparison of HgCdTe and QWIP technologies [43]

	<b>HgCdTe FPA</b>	<b>QWIP FPA</b>
Material Cost	\$3000/inch <sup>2</sup>	\$300/inch <sup>2</sup>
Size of Wafer	7 inch <sup>2</sup>	7 inch <sup>2</sup>
Lot Cost (10 wafers, 2 inch dia)	\$210,000	\$21,000
Processing Cost (for 70 inch <sup>2</sup> )	\$140,000	\$20,000
Total Cost	\$350,000	\$41,000
Chip Yield (FPA)	25%	50%
Relative Cost	17	1

Among industrial examples, Sofradir 480x6 HgCdTe sensor offers 25 mK NETD value with single row integration time of 20  $\mu$ s in a scanning system (at 80K, f/2.5) [44]. For 640x480 image format this corresponds to minimum 12.8 ms frame time. Standard 640x512 QWIP of QWIP-Tech gives 25 mK NETD value at f/2 at 60 K with 15 ms integration time. It is seen that standard staring QWIP FPA competes with scanning HgCdTe array sensors. However the 60K cooler requirement, together with higher sensor area, and lower f/#, hence larger optics requirements are disadvantage of this example QWIP. One improvement to this design is increasing

the integration time to 30 ms with a very low gain QWIP structure known as photovoltaic QWIP [6]. This design can reach 10 mK NETD at 640x512 format with f/2 optics, at the expense of increased integration time. Table 2.2 summarizes performance of some commercially available IR FPAs. It can be concluded that for applications allowing long integration times, QWIP is an alternative IR image sensor. Moreover, if an application demands staring LWIR sensor with format larger than 384x288, QWIP is the only available technology that can offer <40 mK NETD.

Table 2.2: Performance summary of some example commercial LWIR FPAs.

Company	Sensor	Pitch	Integration time	f/#	NETD (Temporal)
Sofradir[44]	480x6 MCT	49.8 $\mu\text{m}$ x 25.4 $\mu\text{m}$	20 $\mu\text{s}$	f/2.5	25 mK
Sofradir	384x288 QWIP	28 $\mu\text{m}$ x 28 $\mu\text{m}$	< 17 ms	f/2	25 mK
AIM [45]	640x512 pv-QWIP	24 $\mu\text{m}$ x 24 $\mu\text{m}$	30 ms	f/2	<10mK
Sofradir	320x256 MCT	30 $\mu\text{m}$ x 30 $\mu\text{m}$	<2.5 ms	f/2	18 mK
AIM	256x256 MCT	40 $\mu\text{m}$ x 40 $\mu\text{m}$	0.35 ms	f/2	<20 mK
AIM	256x256 pv-QWIP	40 $\mu\text{m}$ x 40 $\mu\text{m}$	20 ms	f/2	<10 mK
AIM	384x288 QWIP	24 $\mu\text{m}$ x 24 $\mu\text{m}$	1.5 ms	f/2	40 mK
QWIP-TECH [46]	1024x1024 QWIP	19.5 $\mu\text{m}$ x 19.5 $\mu\text{m}$	15 ms	f/2	35 mK
QWIP-TECH	640 x 512 QWIP	25 $\mu\text{m}$ x 25 $\mu\text{m}$	15 ms	f/2	25 mK
QWIP-TECH	320x256 QWIP	30 $\mu\text{m}$ x 30 $\mu\text{m}$	15 ms	f/2	25 mK

When operating temperature of QWIP and HgCdTe is compared, it is seen that HgCdTe photodiodes at the same wavelength can operate at higher temperatures. Quantum well electrons in QWIP are quantized only in the growth direction. However, in the plane of the quantum well they are free to transport, and can occupy a continuum of energy states. Absorbing phonons causes electrons to gain

energy, and be excited from QW and generates dark current. On the other hand, energy bandgap is ideally forbidden for electrons in HgCdTe photodiodes and a valance band electron can only be excited to conduction band by photoexcitation. This is the reason for HgCdTe photodetectors to operate at higher temperatures [1].

Strong mechanical properties, chemical stability and radiation hardness are other advantages of III-V QWIPs over HgCdTe photodiodes. Process temperature of HgCdTe is limited to 85 °C due to material and doping stability. While III-V devices can be processed and stored up to 300 °C temperature or more [45], weak bonds of HgCdTe crystal cause degradation of crystal properties and limit the maximum process and storage temperature of the material.

### **2.3.1 Latest Developments in QWIP, Superlattice, InSb and HgCdTe Technologies**

In the last decade, QWIP technology advanced rapidly, and large format (640x512 and 1024x1024) QWIP FPAs took place in the commercial market [45, 46]. Taking into consideration the fact that 640x512 LWIR HgCdTe FPA is still not commercially available, potential of QWIP technology can be better understood. Today, QWIP technology development is under progress and covers multi-color focal plane arrays. Multi-color detection with advanced image processing is very useful in target tracking, target recognition, missile detection and spectroscopy.

LWIR QWIP technology is offered commercially by many producers. Thales Optronique produces 384x288 ¼ European TV format QWIP imagers with compact packages and medium level performance. It offers 50 mK NETD with a compact f/2.7 optics, and 4° x 3° field of view (Figure 2.8).

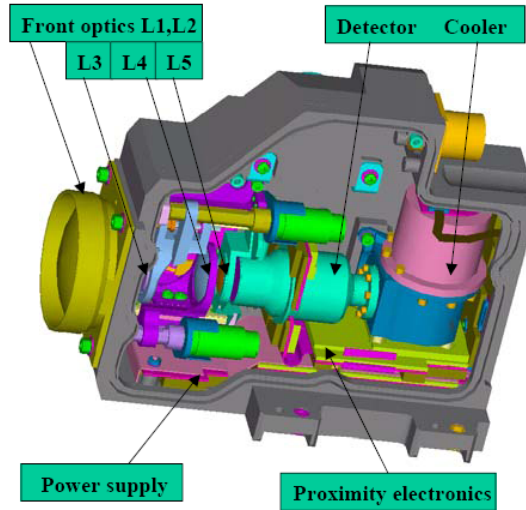


Figure 2.8 384x288 AlGaAs/GaAs QWIP “Catherine” thermal camera offered commercially by Thales [47].

German company AIM demonstrated another compact LWIR QWIP thermal camera with 640x512 QWIP FPA. The performance is reported to be 20 mK NETD with integration time less than 20 ms with  $f/2$  optics. Figure 2.9 shows the camera and example thermal image.

MWIR FPA fabrication is far more mature when compared to LWIR FPAs. The main reason is the low ( $\sim 100\text{meV}$ ) bandgap energy or photoexcitation energy associated with LWIR intrinsic photodetectors. Low bandgap materials tend to have large lattice constants and weak mechanical properties. Moreover, uniformly synthesizing these crystals has always been a problem [48]. MWIR photosensitive materials have bandgap or photoexcitation energy near 300-400 meV. Higher activation energy and bandgap not only make these materials stronger but also reduce the thermionic emission probability of electrons in the device and allow less stringent cooling requirements. When compared with LWIR devices same level of activation energy variation corresponds to less nonuniformity hence allow better image quality. Chapter 3 includes more detailed discussion of FPA figure of merits.

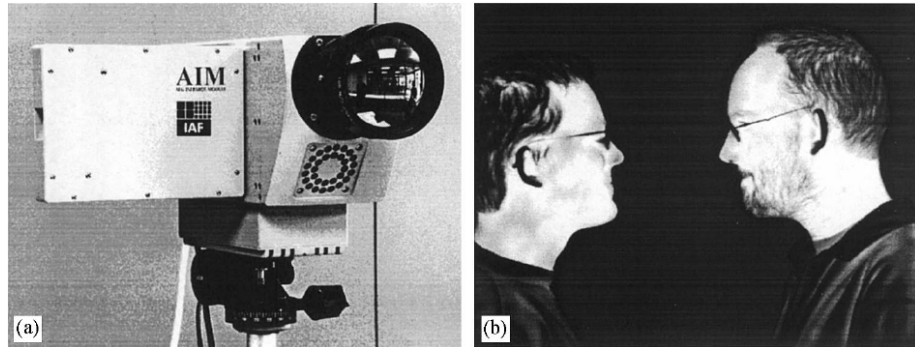


Figure 2.9 640x512 LWIR QWIP thermal camera demonstrated by AIM (a), and example thermal image obtained with this camera (b) [6].

InSb photodiode FPAs are relatively easier to fabricate since they do not have a heterojunction. Cincinnati Electronics demonstrated 1024x1024 format InSb FPA with 13 mK NETD, and also demonstrated 2048x2048 FPA. Figure 2.10 shows an image obtained with 2048x2048 InSb FPA [49]. Megapixel sized MWIR AlGaAs/InGaAs QWIPs are also demonstrated by Missile Defence Agency. These devices reach 19 mK NETD with f/2.5 optics at 95 K. Figure 2.11 shows the FPA photo and thermal image obtained with this FPA[50].

Superlattice infrared photodetectors utilizing type-II GaSb/InAs or GaInSb/InAs material system showed promising performance for future thermal imaging systems. Recently AIM demonstrated 256x256 format MWIR GaInSb/InAs FPA yielding 10 mK NETD with f/2 optics at 5 ms integration time [8]. AIM's Commercial MWIR 384x288 superlattice FPA has <50 mK NETD performance with 24  $\mu\text{m}$  pitch. The pitch of the FPA is 40  $\mu\text{m}$  and the FPA temperature is at 73 K. Figure 2.12 shows example thermal images obtained with this FPA. 384x288 MWIR/LWIR dual band GaInSb/InAs type-II superlattice FPA and 78 K operation of 320x256 format GaSb/InAs type-II superlattice infrared photodetectors is also reported [8,51].



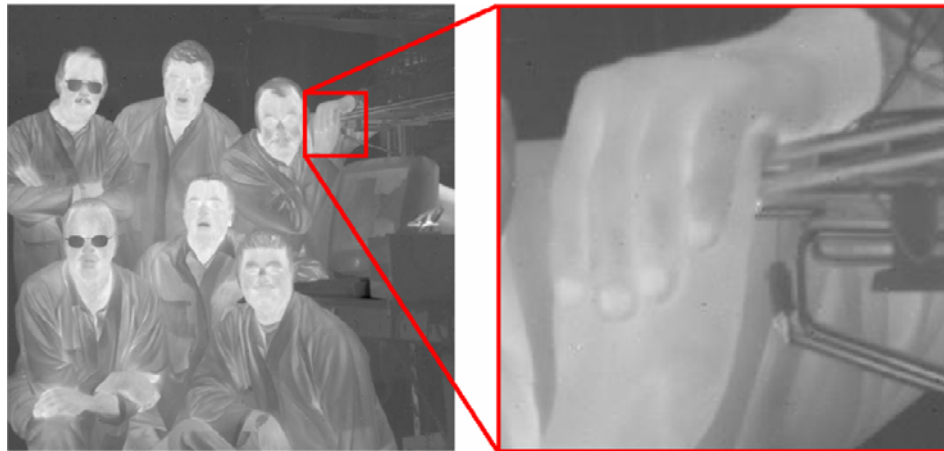


Figure 2.10 2048x2048 high resolution InSb FPA image from Cincinnati Electronics [49]

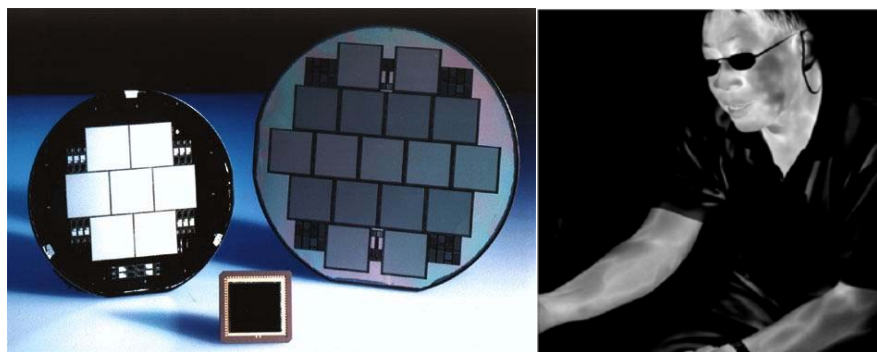


Figure 2.11 Fabricated 1024x1024 MWIR QWIP FPAs and MWIR image obtained from 1024x1024 format QWIP FPA. [50]



Figure 2.12 Thermal image obtained with 256x256 MWIR GaInSb/InAs type-II superlattice infrared photodetector FPA [8].

### 2.3.1.1 Recent Developments in Multi-Color QWIP FPAs

Important reports in multi-color QWIP development field are summarized in this section. U.S. Army Research Laboratory at Adelphi reported the following performance specifications for 256x256 MWIR-LWIR QWIP camera in 2001, images obtained with this system is given Figure 2.13 [42]

NETD	:	30 mK (MWIR) / 34 mK (LWIR)
Spectral Band	:	LWIR : 8.2 $\mu\text{m}$ – 9.0 $\mu\text{m}$ MWIR : 4.7 $\mu\text{m}$ – 5.2 $\mu\text{m}$
Measurement Temperature	:	60 K
F/#	:	3

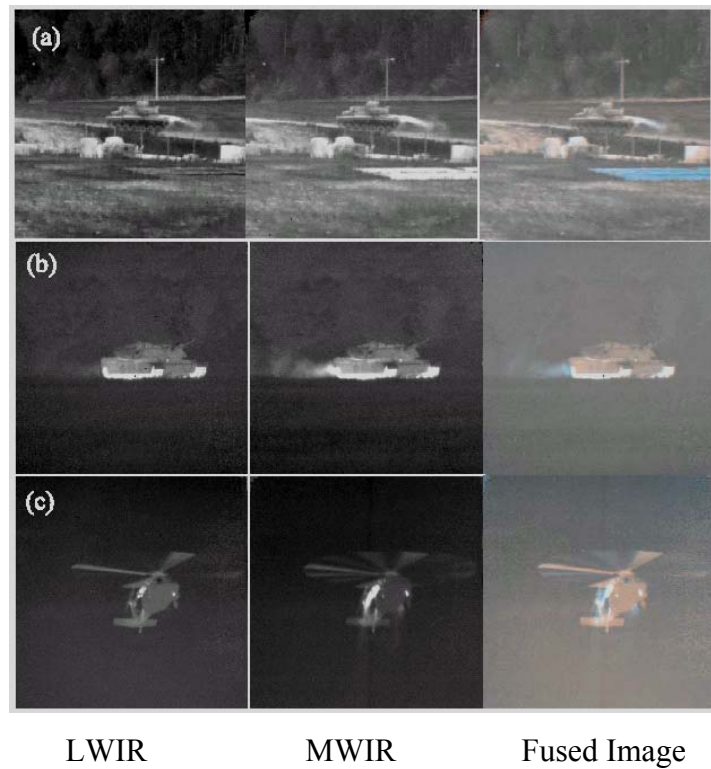


Figure 2.13 Images taken with a two-band QWIP camera and the fused image obtained from these two-band images. (a) M60 tank, (b) M1-A1 tank, (c) Blackhawk helicopter [42]

In 1999, NASA Jet Propulsion Laboratory (JPL) reported 74K video images taken with 640x512 LWIR-VLWIR QWIP camera. Figure 2.14 shows example image from this dual band LWIR/VLWIR QWIP FPA. Reported performance values were [52],

NETD	:	36 mK (LWIR) ve 44 mK (VLWIR)
Spectral Band	:	8 $\mu\text{m}$ -9 $\mu\text{m}$ (LWIR), 14 $\mu\text{m}$ -15 $\mu\text{m}$ (VLWIR)
Measurement Temperature	:	40 K
F/#	:	f/2 lens
Frame rate	:	30 Hz

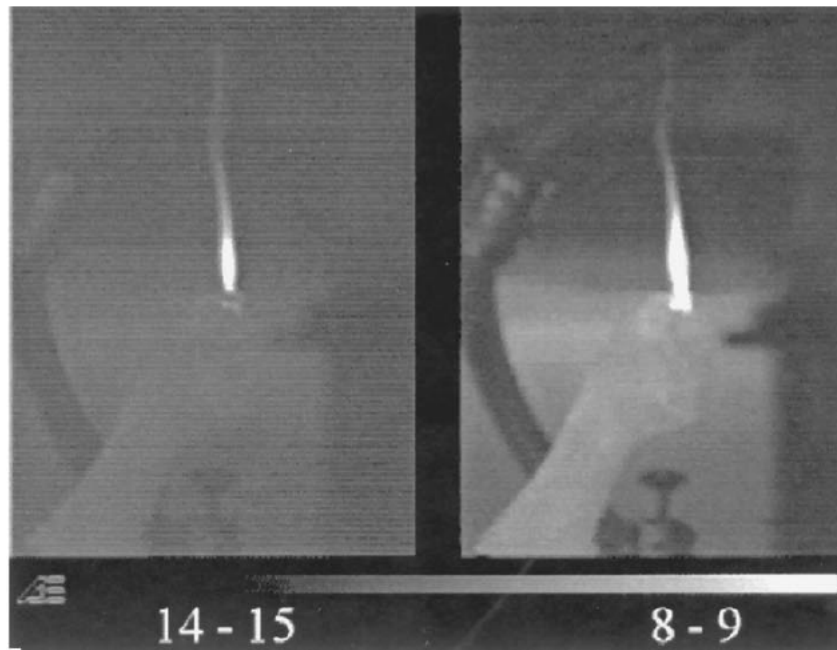


Figure 2.14 Images obtained with LWIR/VLWIR 640x512 QWIP FPA [52].

In 2001, Lockheed-Martin reported 256x256 MWIR-MWIR, LWIR-MWIR and LWIR-LWIR multi-color QWIPs [35] Reported performance values are given below and images taken with these 256x256 two color/band arrays are given in Figure 2.15.

#### MWIR-MWIR 256x256

NETD	:	41 mK and 32 mK
Peak Response Wavelength	:	4.0 $\mu\text{m}$ and 4.7 $\mu\text{m}$
Measurement Temperature	:	90 K
F/#	:	f/3
Frame Rate	:	100 Hz

#### MWIR-LWIR 256x256

NETD	:	<35 mK , for both bands
Peak Response Wavelength	:	8.5 $\mu\text{m}$ (LWIR) and 5.1 $\mu\text{m}$ (MWIR)

Measurement Temperature	:	65 K
F/#	:	f/2
Frame Rate	:	100 Hz

#### LWIR-LWIR 256x256

NETD	:	23 mK and 43 mK
Peak Response Wavelength	:	8.3 $\mu\text{m}$ and 11.2 $\mu\text{m}$
Measurement Temperature	:	40 K
F/#	:	f/3
Frame Rate	:	100 Hz

AEG Infrarot Module (AIM, Germany) has been working on QWIPs for more than 10 years. Their commercial QWIP 388x284 MWIR/LWIR FPA is a stacked QWIP with 3 connections per pixel. Figure 2.16 shows SEM image of pixels of this FPA. The reported NETD value is 43 mK for LWIR band and 17 mK for MWIR band.

#### **2.3.1.2 Recent Developments in Two-Band HgCdTe FPAs.**

Intense research and development on multi-color/band HgCdTe focal plane arrays is also under progress. Recent advancements in this field is summarized in this section. AIM reported feasibility of 2 color MWIR/MWIR 192x192 HgCdTe FPA [7]. The reported parameters are :

NETD	:	30 mK (Band 1), 25 mK (Band 2)
Spectral Band	:	3.4 $\mu\text{m}$ -4.0 $\mu\text{m}$ (Band 1), 4.2 $\mu\text{m}$ – 5.0 $\mu\text{m}$ (Band 2)
f/#	:	3
Frame Rate	:	Maximum 870 Hz

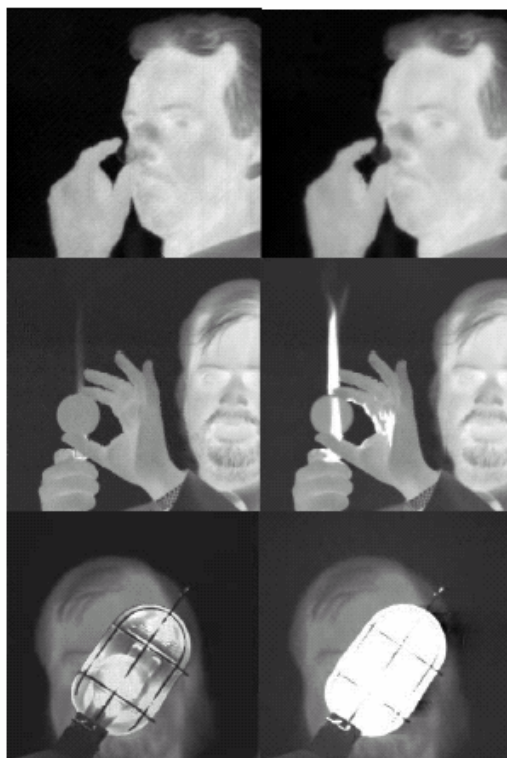


Figure 2.15 2 color QWIP images obtained with Lockheed-Martin FPAs. From top row to bottom row : LW/LW, LW/MW, MW/MW [35].

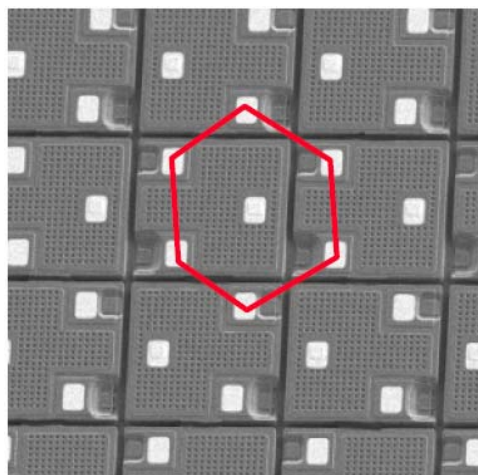


Figure 2.16 SEM picture of dual band pixels of 388x284 dual-band FPA. Adjacent pixels have altered indium bump connections for denser layout [45].

This HgCdTe focal plane array has the advantage of having 30 mK NETD at 800 Hz frame rate. Due to this advantage, the sensor is targeted for missile seeker applications [7].

LETI Infrared Laboratory (France) developed two-color HgCdTe FPA in collaboration with France Ministry of Defense and the commercial company SOFRADIR. Performance of this FPA is summarized below [53]:

$R_oA$	:	$10^7 \Omega.cm^2$ (Band 1), $4 \times 10^5 \Omega.cm^2$ (Band 2)
Spectral Band	:	$2.3 \mu m - 3.1 \mu m$ (Band 1), $3.2 \mu m - 5.0 \mu m$ (Band 2)
Quantum Efficiency	:	%50 (Band 1, without antireflection coating) %75 (Band 2, without antireflection coating)

Hughes laboratory (U.S.A.) reported the following specifications for LWIR-MWIR single pixel HgCdTe photodetector [54].

$R_oA$	:	$>100 \Omega.cm^2$ (LWIR) and $5.5 \times 10^5 \Omega.cm^2$ (MWIR)
Cutoff wavelength	:	MWIR : $5.5 \mu m$ LWIR : $10.2 \mu m$

The above discussions emphasize the importance of QWIP technology as an alternative to the costly HgCdTe technology to lower the cost of high performance thermal imagers. The developments in QWIP technology rely on new design approaches and new material systems for better focal plane array performance. In the next chapter, the infrared focal plane array technology is summarized.

## **CHAPTER 3**

### **INFRARED FOCAL PLANE ARRAYS**

Infrared focal plane arrays (IR FPA) consist of IR sensitive detector pixels arranged in 2D matrix form or as 1D linear array placed at the focal plane of optical system of an imager. 2D arrays are called staring arrays, while 1D arrays need a scanner mechanism to generate an image, hence named scanned arrays. Choosing scanned or staring arrays in an optical system depends on the resolution, frame rate, wavelength region, sensor availability, and other factors. While shorter wavelength IR detectors are easier to fabricate in large FPA formats up to 2048x2048 [48], longer wavelength IR materials often cannot conform the uniformity requirements for this large area matrix fabrication.

Chapter 2 includes discussion of QWIP figure of merits at single photodetector level. This chapter discusses figure of merits for IR FPAs, read-out electronics, and IR cameras at a system level keeping focus on the infrared detector which is the core of an infrared imager.

#### **3.1 Design Issues of Infrared Imagers and FPAs**

Focal plane array design for thermal imaging applications depends strongly on application and system needs. Figure 3.1 shows fabrication sequence of a typical thermal imager integrated detector dewar cooler (IDDCA) assembly which consists



of IR detector, ROIC, packaging and the cooling peripheral. The IDDCA is the core of the thermal imager, and the FPA is the core of the IDDCA. The properties of the optics, cooler, proximity electronics, and signal processors in these steps are all determined by the FPA specifications.

### **3.1.1 Atmospheric Window and Peak Detection Wavelength**

The design starts with the atmospheric window to be used. The atmospheric transmission dependence on wavelength is shown in Fig 1.1. Peak detection wavelength of the detector determines the activation energy hence the dark current generated in the device. The target to be imaged can be terrestrial background in tactical environments, can be exhaust plumes in missile seeker applications, or can be cold objects in low background strategic applications in space. The wavelength of photons emitted from these different type backgrounds determine the detector type to be used. In the LWIR band high performance military thermal imagers are today limited to HgCdTe, QWIP, Superlattice photodetectors. In the MWIR band InSb, and HgCdTe photodetectors are widely used technologies. For the SWIR band imaging applications InGaAs and HgCdTe photodiode arrays can be used [48].

LWIR imaging band offers higher flux than in MWIR band (Fig. 1.2). Depending on application, most of the military targets emit largest amount of photons in LWIR band, hence higher signal levels can be obtained. However, in high resolution applications demanding smaller diffraction blur spot, or in applications demanding high temperature object imaging MWIR can be preferable. If low signal of an MWIR sensor pixel can be read from the wide system noise floor, MWIR sensors gives better NETD values for high temperature scene imaging. [48]

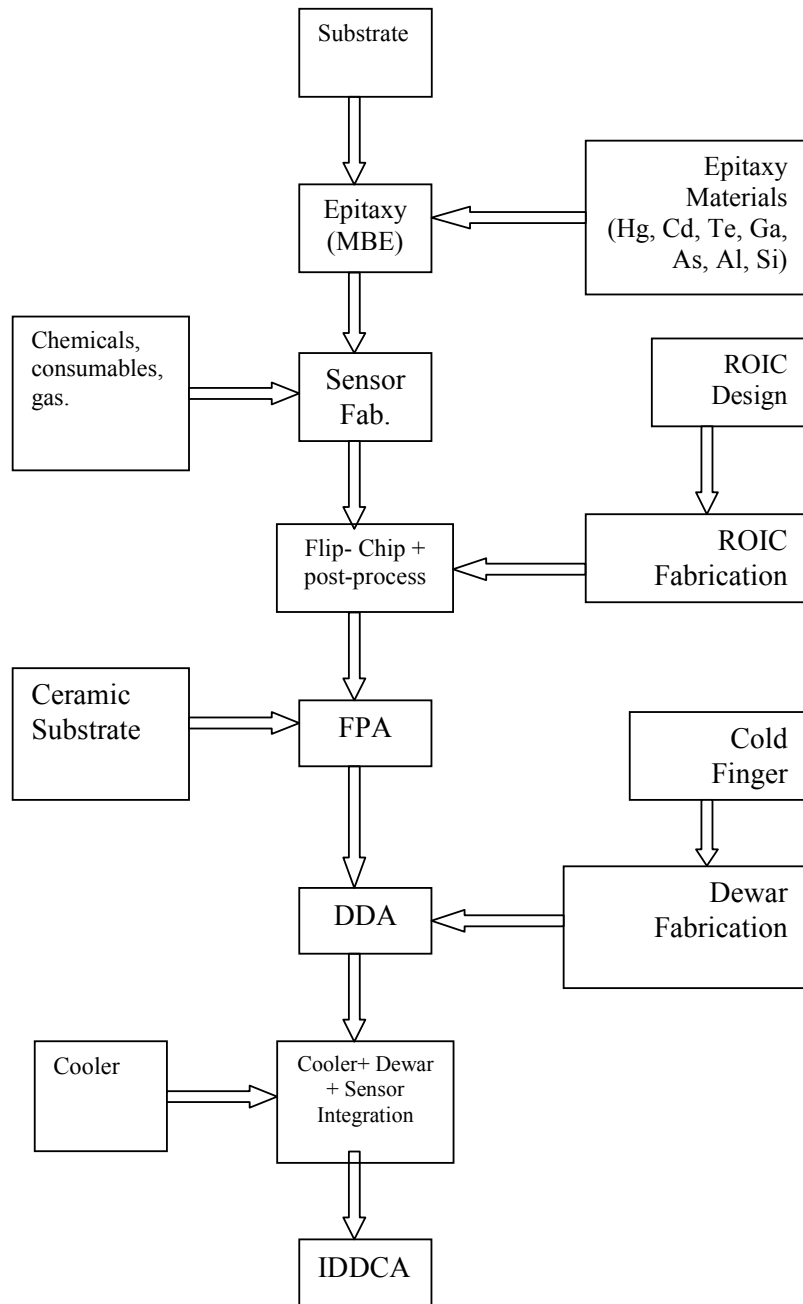


Figure 3.1 Fabrication sequence of a cooled IR FPA.

### 3.1.2 Detector Type and Material

Any kind of photon detector's SNR is limited with the stochastic nature of the incident photons falling onto the detector. Photons are emitted from objects with random interval and this random character puts a fundamental noise onto the signal collected from a detector. The shot noise nature of photons can be expressed as the shot noise of photoelectrons at the terminal of a photodiode. When photocurrent is greater than the dark current, this fundamental limitation puts an upper limit to photodetector detectivity, and the photodetector is named "background limited infrared photodetector" (BLIP). Figure 3.2 shows BLIP detectivity limit, and detectivity vs. wavelength plot of some example photodetectors [48].

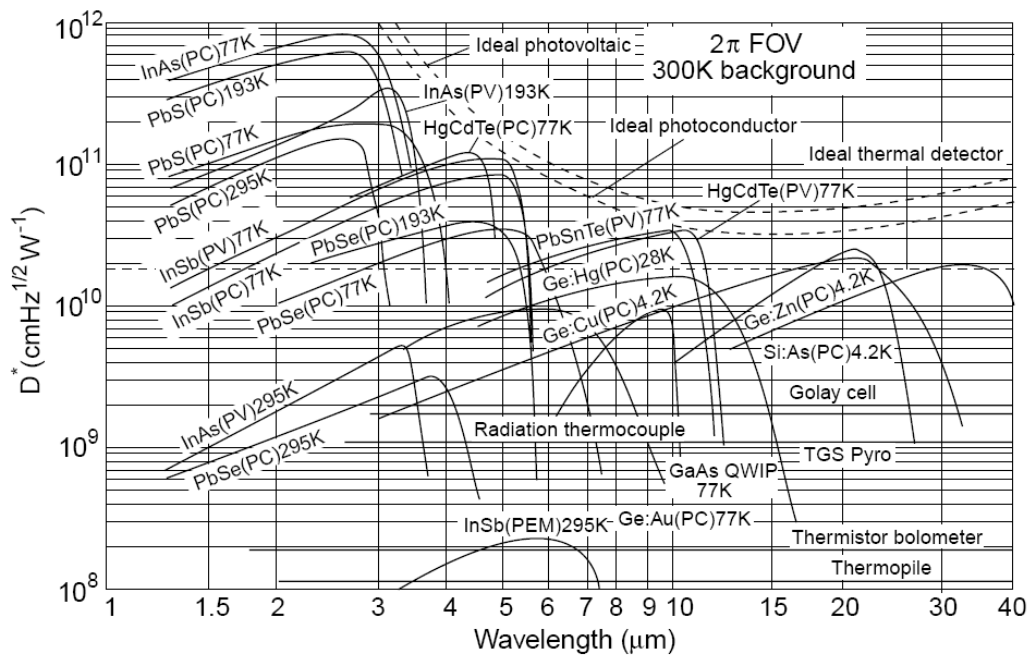


Figure 3.2 BLIP detectivity limit at  $180^\circ$  field of view and 300 K background. Detectivity vs. wavelength plot of some infrared detector types [48].

Among many different detector technologies proposed until today, only some of them managed to reach production level for military thermal imaging cameras. The design issues explained in this chapter and the cost of the system made some

Table 3.1: Comparison of modern military infrared photon detector technologies [45].

Performance Parameter	InSb (3-5 $\mu\text{m}$ )	HgCdTe (3-5 $\mu\text{m}$ )	HgCdTe (8-11.5 $\mu\text{m}$ )	AlGaAs/GaAs QWIP (3-5 $\mu\text{m}$ )	AlGaAs/GaAs QWIP (8-12 $\mu\text{m}$ )	InAs/(GaIn)Sb Superlattices (3-5 $\mu\text{m}$ )	InAs/(GaIn)Sb Superlattices (8-11.5 $\mu\text{m}$ )
<b>Quantum efficiency for ideal AR-coating</b>							
Front-side illumination	%90	%90	%90	n/a	n/a	as HgCdTe	as HgCdTe
Backside illumination	%90	>%70	>%70	%15 peak	%10-30 peak		
<b>AR coating, reflectivity</b>	<%5	<%5 for backside illumination	<%5 for backside illumination			<%5 for backside illumination	<%5 for backside illumination
<b>1/f noise behaviour</b>	As HgCdTe MW	As InSb	More sensitive than in 3-5 $\mu\text{m}$	Negligible	Negligible	As InSb	More sensitive than in 3-5 $\mu\text{m}$
<b>Operation Temperature</b>	<90 K	< 140 K	< 80 K	88 K	< 70 K	< 120 K	< 80 K
<b>Cut-off</b>	5.7 $\mu\text{m}$	Adjustable with composition	Adjustable with composition	Adjustable with layer structure	Adjustable with layer structure	Adjustable with layer design	Adjustable with layer design
<b>Dark current, <math>j_D</math></b>	Excessive $j_D$ due to mismatch of cut-off wavelength and atmospheric window	$j_D$ matches to atmospheric window	$j_D$ matches to atmospheric window	$j_D$ matches to atmospheric window	$j_D$ matches to atmospheric window	$j_D$ matches to atmospheric window	$j_D$ matches to atmospheric window
<b>Availability of substrates</b>	Commercially available	Own growth necessary	Own growth necessary	Commercially available	Commercially available	Commercially available	Commercially available
<b>Operability of pixel</b>	>%99.5	>%99.5	> %97	> %99.8	> %99.8	As QWIP	As QWIP
<b>Temperature stability of material and doping</b>	> 120 °C	< 85 °C	< 85 °C	> 300 °C (limited to > 120 °C by In-bumps)	> 300 °C (limited to > 120 °C by In-bumps)	> 120 °C	> 120 °C
<b>Long term stability of material</b>	Good	Medium	Medium	Good	Good	tbd	tbd
<b>MTF, Crosstalk</b>	Long diffusion length, diffraction in mesa structure, reduced MTF at Nyquist	Diffusion length reduced, no diffraction in planar technology, higher MTF at Nyquist	Diffusion length reduced, no diffraction in planar technology, higher MTF at Nyquist	Diffraction in mesa structure and grating, reduced by removal of substrate	Diffraction in mesa structure and grating, reduced by removal of substrate	Mesa structure but no grating, substrate removed	tbd
<b>Spectral bandwidth</b>	Wide	Wide	Wide	Narrow, tunable by layer structure	Narrow, tunable by layer structure	Wide	Wide
<b>Multi color, multiband capability</b>	No	Yes	Yes	Yes	Yes	Yes	Yes
<b>Production equipment for layer growth</b>	Special	Special	Special	Commercially available, GaAs technology	Commercially available, GaAs technology	Commercially available, GaAs technology	Commercially available, GaAs technology

technologies obsolete, or they remained at experimental level. Table 3.1 summarizes advantages and disadvantages of state-of-the-art infrared photodetector types [45].

### 3.1.3 Optical System

Scanning systems employ a scanner mechanism placed on the path of the optical lens assembly. Figure 3.3 shows image formation on an interlaced scanner imager. The sensor is a linear array in these systems and an oscillating scanning mirror scans the area to be imaged. In these systems, at each scan step, each detector pixel can integrate infrared light for a finite time whose maximum can be expressed as

$$\tau_{\text{int}} = 1/(\text{Frame Rate} * \text{number of displayed pixels on a row}) \quad (3.1)$$

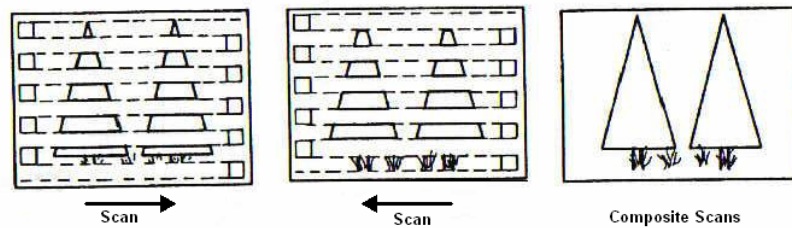


Figure 3.3 Thermal imaging with interlaced scanning [59].

In staring systems detectors are simply placed in the focal plane of the optical system and they take advantage of long integration times. Long integration time decreases the noise bandwidth. As detectors collect photons for a longer time, the signal to noise ratio increases. Maximum integration time limit can be expressed as,

$$\tau_{\text{int}} = 1/(\text{Frame Rate}) \quad (3.2)$$

The imager peak detection wavelength also determines the optical resolution that can be achieved with a thermal imager. Modern infrared optical systems are always designed at the diffraction limit. As the wavelength of the light increases diffraction of the light from a finite aperture limits the size of the minimum spot size to be focused on the FPA. It can be treated as impulse response of the optical system. The blur spot size is given approximately:  $2.4 \cdot \lambda \cdot f/\#$  [56]. Shorter wavelength MWIR detectors offer smaller diffraction blur spot hence have better performance in terms of resolution in long range detection applications. The  $f/\#$  of the system is defined as the ratio of the FPA-optical aperture distance to the aperture diameter (Fig. 3.4). It defines the optical flux incident onto the focal plane from a uniform background. Lower  $f/\#$  optical systems collect higher amount of flux onto the focal plane, but their size, price, depth of focus and optical aberration correction becomes a problem. The intensity of light collected onto focal plane through a circular aperture defining  $f/\#$  is expressed as:

$$E' = \frac{E}{4(f/\#)^2 + 1} \quad (3.3)$$

where  $E$  is the exitance from a unity emissivity background as expressed in equation 1.1. Higher  $f/\#$  systems have lower photon flux collected onto their focal plane but they are more compact, have lower cost, and their design is easier in order to minimize optical aberrations.

The features and distance of the target determine the field of view (FOV) need of a thermal imager. The FOV is defined by the effective focal length of the thermal imager lens (Figure 3.5). It can be expressed by :

$$FOV_{Horizontal} = 2 \tan^{-1} \left( \frac{\text{Sensor width} / 2}{\text{Effective focal length}} \right) \quad (3.4)$$

$$FOV_{Vertical} = 2 \tan^{-1} \left( \frac{\text{Sensor height} / 2}{\text{Effective focal length}} \right) \quad (3.5)$$

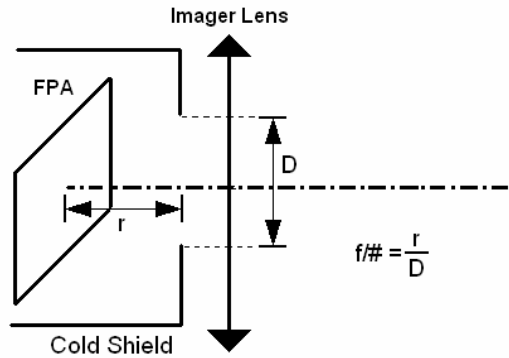


Figure 3.4 Definition of f-number for a staring array thermal imager.

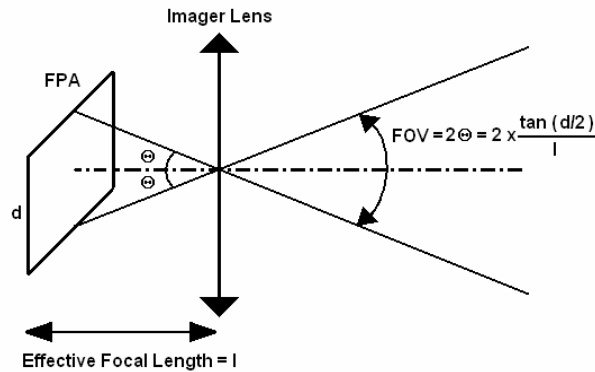


Figure 3.5 Example diagram showing vertical field of view (FOV) calculation.

### 3.1.4 Read Out Integrated Circuit Topology

Cooled infrared detector material technology does not allow monolithic fabrication of ROIC and the photodetector array on the same substrate. Hence hybrid integration of silicon CMOS ROIC and compound semiconductor sensor array is

necessary. Usually the ROIC is an analog multiplexer which serially guides analog data from each pixel to output ports. Figure 3.6 shows the block diagram of a typical staring array ROIC.

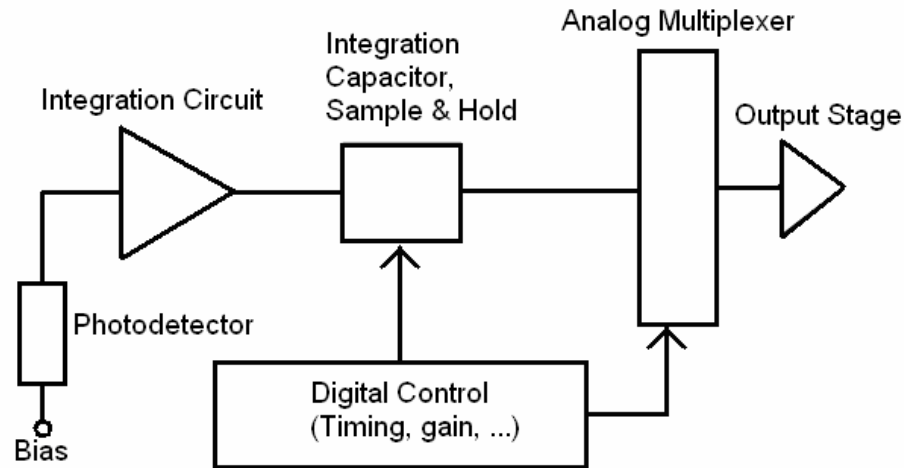


Figure 3.6 Block diagram of a typical staring array ROIC.

Flip-chip bonded photodiodes inject their photocurrent into the circuit via indium bumps. Collection of signal is usually done by integrating photocurrent on an integration capacitor. The front part of the ROIC is called integration circuit. For different applications and technologies, integration circuit architecture is significantly changed where the rest of the stages remain similar to those in other ROIC designs.

#### 3.1.4.1 Direct Injection ROIC

Direct injection (DI) read out is the widely used input circuit in military thermal imaging technology. Figure 3.7 shows typical direct injection unit cell. Due to its simplicity, direct injection unit cells usually employ in-pixel integration capacitor and allow long integration times. There is no active power dissipation other than that on the photocurrent path. Hence DI circuits allow dense and large format



ROIC design. Detector bias is adjusted from the  $V_{\text{detector}}$  pin or  $V_{\text{DI}}$  gate voltage of the input MOSFET. The “Reset” signal resets the charge on the integration capacitor  $C_{\text{int}}$  before beginning of each frame. However, the bias on the detector monotonously decreases during integration which results in shift from the optimum operating point of the photodetector. Furthermore, this shift can occur non-uniformly, degrading the spatial uniformity of the imaging array. DI circuits may also suffer from low injection efficiency [57, 58]. Injection efficiency is related to sharing of photocurrent between the photodetector’s internal dynamic resistance and the input resistance of the ROIC unit cell as explained in figure 3.8. In DI architecture, injection efficiency ( $\eta$ ) depends on transconductance of the input MOSFET ( $g_m$ ), and at low frequencies injection efficiency is given as [59] :

$$\eta = \frac{g_m R_{\text{Detector}}}{1 + g_m R_{\text{Detector}}} \quad (3.6)$$

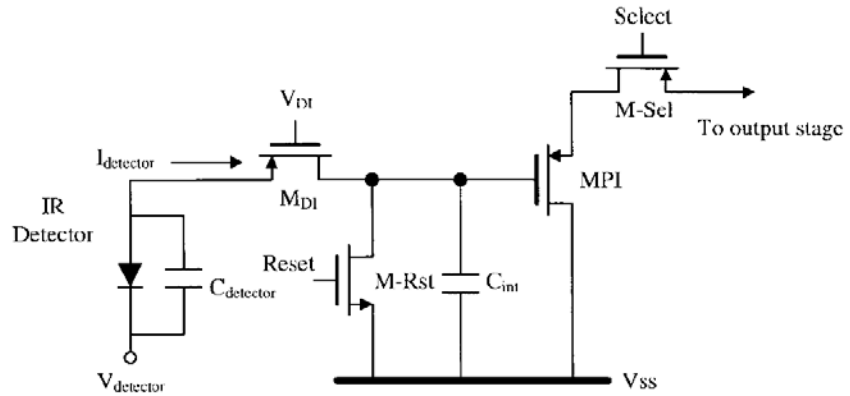


Figure 3.7: Direct injection ROIC input schematic [60]

QWIPs usually have very large dynamic resistance at their operating points hence near unity injection efficiency is easily obtained with direct injection ROIC. However the competing LWIR HgCdTe photodiodes may suffer from low  $R_0A$  products and this can degrade their ROIC injection efficiency. In this Ph.D. study

Indigo Systems 640x512 ISC9803 ROIC with DI circuit is used as explained in the next chapter.

DI architecture can be modified in order to decrease the input impedance seen by the photodetector at the input node. Buffered direct injection (BDI) (Figure 3.9) occupies an input preamplifier with gain  $-A$ , which drives the injection transistor with feedback. Hence the channel impedance of the input MOSFET is reduced approximately by a factor of  $1/(1+A)$ . Moreover with the help of the negative feedback, the detector bias is better controlled during integration. However extra amplifier added to the circuit increases complexity and power dissipation [60].

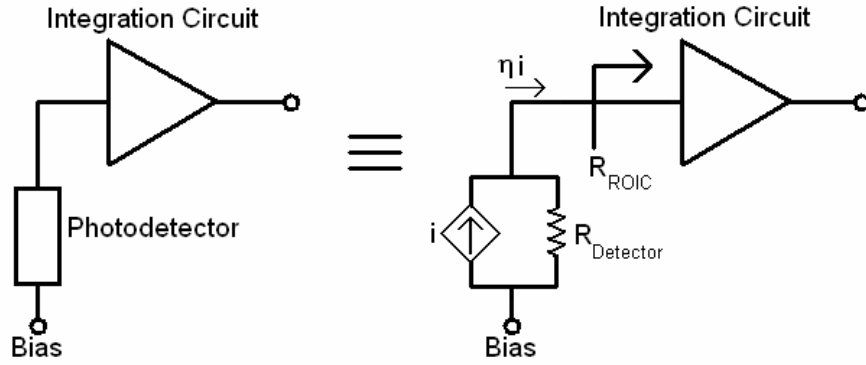


Figure 3.8: Modeling of photocurrent injection into the ROIC integration circuit from the photodetector.

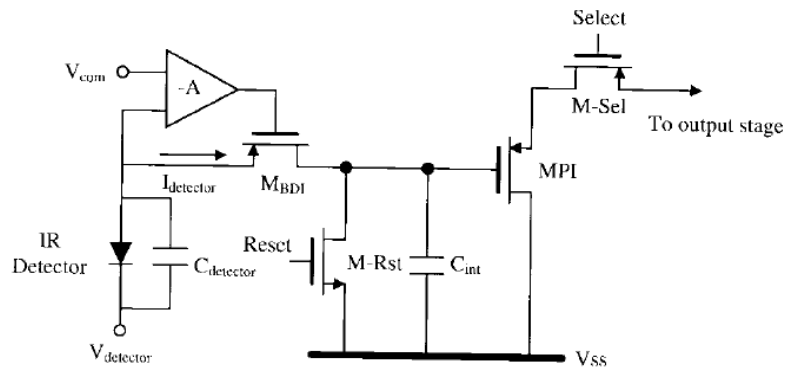


Figure 3.9 Schematic of buffered direct injection circuit [60]

### 3.1.4.2 Source Follower per Detector ROIC

Source follower per detector (SFD) employs a photodiode's self capacitance and the input node capacitance of the ROIC to integrate the charge. Figure 3.10 shows schematic of an SFD ROIC unit cell. M-Rst transistor resets the input node to  $V_{dd}$  voltage. After reset, the photocurrent discharges the capacitances connected to the node until the “Select” signal samples the node voltage through the follower MNI and MNL transistors.

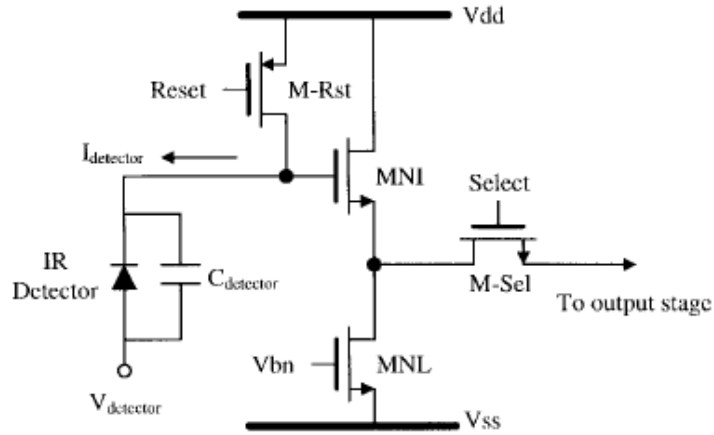


Figure 3.10 Schematic of source follower per detector ROIC input stage [60]

For high density, low power, and short integration time applications SFD input cell can be used, SFD ROICs with 2048x2048 format are being used for MWIR astronomical imaging applications [61]. However, the SFD architecture again cannot stabilize the detector bias during integration and suffers from switching noise which creates spatial nonuniformity through the array [60].

### 3.1.4.3 Capacitive Transimpedance Amplifier ROIC

For further bias stability on the detector, capacitive transimpedance amplifier shown in Figure 3.11 can be used. The inverting amplifier feedback includes the integration capacitor, and due to Miller effect smaller size capacitors can be used. Detector bias is controlled via  $V_{com}$  and  $V_{detector}$  bias voltages. The M-Rst MOSFET resets the integration capacitor before beginning of each frame period.

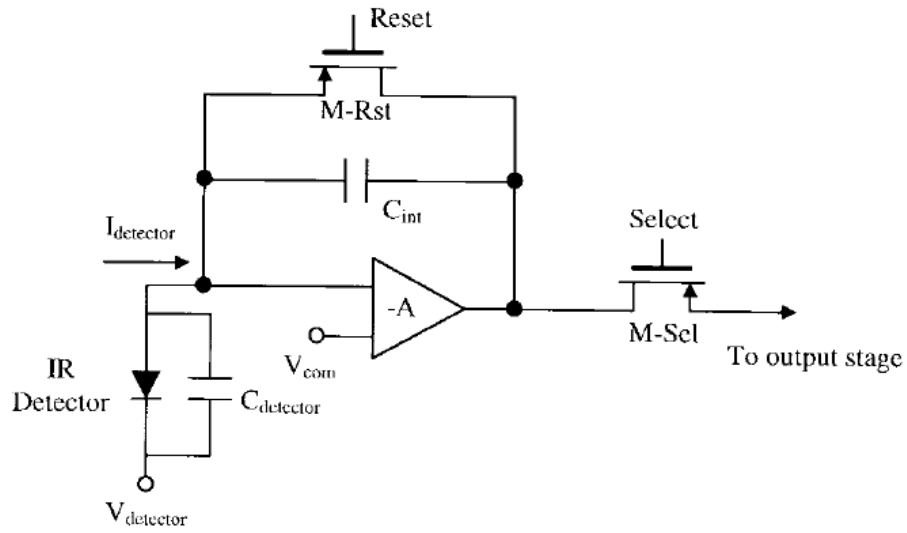


Figure 3.11 Schematic of capacitive transimpedance amplifier unit cell. [60]

### 3.1.4.4 ROIC Input Stages with Current Mirror

Instead of integrating the photocurrent directly onto an integration capacitor, photocurrent can be mirrored and amplified with a current mirror, injected into a capacitor, and then sampled. Gate modulation, current mirror direct injection and current mirror integration circuits are examples to these approaches. Figure 3.12 shows gate modulation input cell. The photocurrent is injected into current mirror

of  $M_{load}$  and  $M_{input}$  transistors. By adjusting the mirroring ratio, the current can be scaled, and  $C_{int}$  can be charged. In this circuit the dependence of injection efficiency and current gain on threshold voltage mismatch and  $V_{source}$  reference voltage creates uniformity problems.

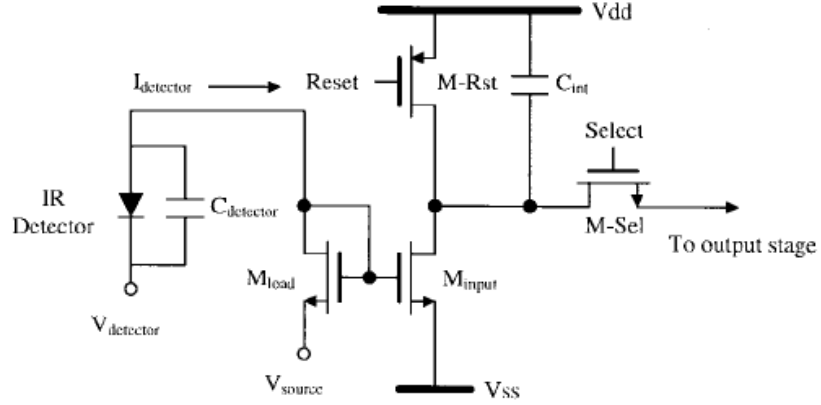


Figure 3.12 Gate modulation input circuit schematic [60].

As an improvement to the gate modulation input circuit the photodetector can be placed on a branch of cascade connected current mirrors. Figure 3.13 shows schematic of current mirror direct injection (CMDI) unit cell. The circuit offers near unity injection efficiency even for low detector impedances. In this circuit, bias on the detector is stabilized by equality of gate-to-source voltages of  $M_{n1}$  and  $M_{n2}$  transistors if they are equal size. This improves the bias stability of the circuit.

Further improvement to CMDI is current mirror integration (CMI) design whose schematic is given in Figure 3.14 [63]. This design offers high injection efficiency, rail to rail operation, and unlike CMDI, an external capacitance can be used with this design. However, for large format QWIP FPAs, in-pixel capacitance is necessary in order to use the sensor with long integration times.

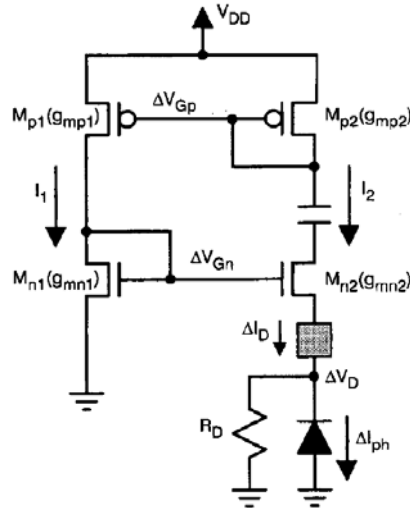


Figure 3.13 Schematic of current mirror direct injection unit cell [62]

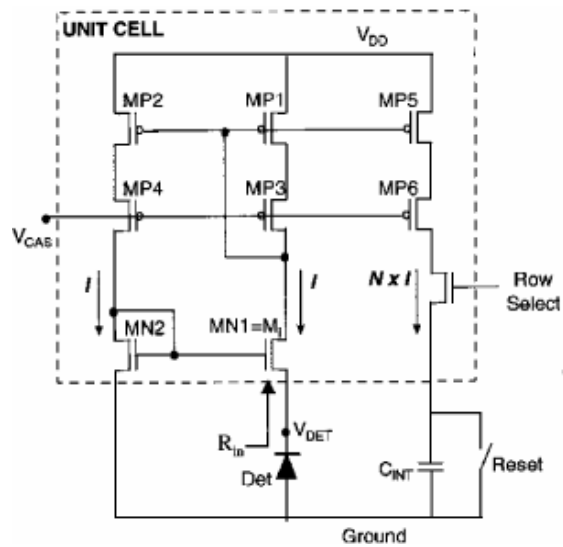


Figure 3.14 Schematic of current mirror integration circuit [63].

### 3.1.5 Frame Rate and Integration Time

When reporting performance of a sensor system, integration time is one of the key factors, since it determines the noise bandwidth of the input circuit and maximum frame rate of the system. Figure 3.15 shows the perfect integrator with a reset

switch. When the integrator integrates charge for  $\tau_{\text{int}}$  time, and is reset periodically, the Fourier analysis gives the equivalent noise bandwidth of [59] :

$$\Delta f = \frac{1}{2\tau_{\text{int}}} \quad (3.7)$$

Assuming a QWIP pixel connected to an integration circuit with unity current gain, and assuming BLIP operation, number of electrons collected on the integration capacitor can be expressed as :

$$N_{\text{Signal}} = I_{\text{Photo}} \tau_{\text{int}} / q \quad (3.8)$$

Assuming G-R noise limited operation, noise electrons integrated on the capacitor can be expressed as:

$$N_{\text{Noise}} = \frac{\tilde{i}_n \cdot \sqrt{\Delta f} \cdot \tau_{\text{int}}}{q} = \sqrt{4qI_{\text{Photo}}g_n} \cdot \sqrt{\frac{1}{2\tau_{\text{int}}}} \cdot \frac{\tau_{\text{int}}}{q} = \sqrt{\frac{2I_{\text{Photo}}g_n\tau_{\text{int}}}{q}} = \sqrt{2N_{\text{Signal}}g_n} \quad (3.9)$$

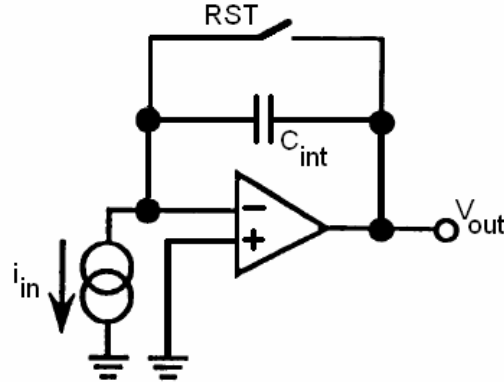


Figure 3.15 Perfect integrator schematic [59].

The SNR of the system is proportional to  $\sqrt{N_{\text{Signal}}}$  hence proportional to  $\sqrt{\tau_{\text{int}}}$ . As the integration time is increased the number of collected carriers increases, but number of noise electrons increases with square root of the signal carriers. Hence, increasing the integration time monotonously increases SNR of the system.

### 3.1.6 Cooler Requirements

Modern cooled thermal imager cameras use closed cycle Stirling cycle coolers with miniature dewars (Figure 3.16). Approximately half of the cost of the IDDCA is due to the cryogenic equipment surrounding the sensor. Above discussed FPA sensor specifications determine the sensor operating temperature, sensor active area, ROIC power consumption, cold shield diameter, and optical interface. All of these factors determine the cooler heat load, which is the allowable heat to be transferred from the FPA surface at the operating temperature. The heat load of the cooler strongly determines the price and mean lifetime of the cooler. Military Stirling coolers' heat load range from a few mW to 5 W depending on application [45]. While a missile seeker application requiring rapid cool-down time require a small sensor operating above 100 K and a compact cooler, a high performance mega-pixel QWIP thermal imager would require a larger capacity cooler due to its large sensor area.



Figure 3.16: Stirling cooler integrated with detector dewar which houses the FPA in vacuum conditions [64].



## **3.2 FPA Figure of Merits**

Measuring performance parameters of an infrared FPA is in essence measuring its SNR at different frame rates, operating temperatures, and at different ROIC modes.

### **3.2.1 Noise Equivalent Temperature Difference (NETD)**

Temporal signal recorded from each pixel of an imager includes some level of uncertainty. Standard deviation of this time domain signal is called temporal noise of the pixel. If a differential signal from a spot on the image is smaller than this temporal noise, the temperature difference in time cannot be resolved with that imager. The minimum differential temperature change that can be detected with a single pixel is called noise equivalent temperature difference (NETD) of that pixel. NETD of a system depends on SNR of the system. NETD pixel map and histogram of a sensor is used to compare FPA/ROIC hybrids with each other when a constant temperature background is being imaged. As a general rule, parameters effecting the SNR should be reported with NETD measurement results. Some of them are  $f/\#$ , detector temperature, detection wavelength, and integration time.

### **3.2.2 Minimum Resolvable Temperature Difference (MRTD)**

When an object to be imaged is far away and could only occupy 1 pixel of the FPA, the detection range is limited by the temporal characteristics of the FPA. The signal from the object at distance  $r$  is proportional to  $1/r^2$ , and until it exceeds the noise of the pixel the object is undetectable. However, when the object occupies many pixels on the screen, recognition and identification is only possible if the adjacent pixels have uniform response. Moreover, light diffraction and optical crosstalk should not limit the observer (Figure 3.17) [65]. In order to test the effects of all of these

aspects on the FPA performance, minimum resolvable temperature difference (MRTD) measurement is performed.

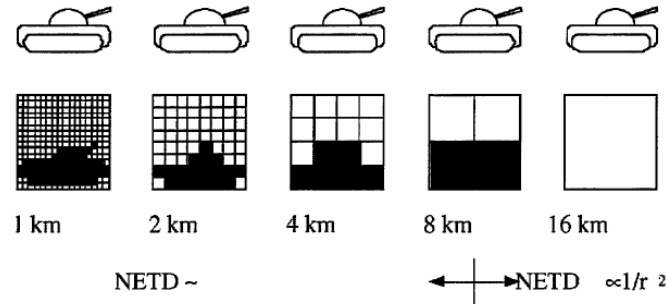


Figure 3.17 Illustration of condition when the target occupies one pixel, and many pixels [65].

While the NETD test characterizes only the FPA, ROIC, and proximity electronics' performance, MRTD characterizes whole system from the thermal imaging lens to the operator display monitor, and even may include effect of the training level of the operator. The test is performed by placing standard thermal targets in front of the thermal imager. The light from the targets are passed through the collimator in order to simulate the necessarily high spatial frequencies. Figure 3.18 shows example bar target pattern. The black regions and the white regions have temperature difference set by the operator. The operator sets the display contrast to maximum and begins to lower the temperature difference between the black bars and the white background. Higher spatial frequency bars disappear, and cannot be resolved as temperature difference is reduced. This temperature difference is recorded as minimum resolvable temperature difference at the spatial frequency of the bar pattern. As the operator continues to decrease the temperature difference, other spatial frequency bars become irresolvable. This procedure results in MRTD vs. spatial frequency plot [66,67].

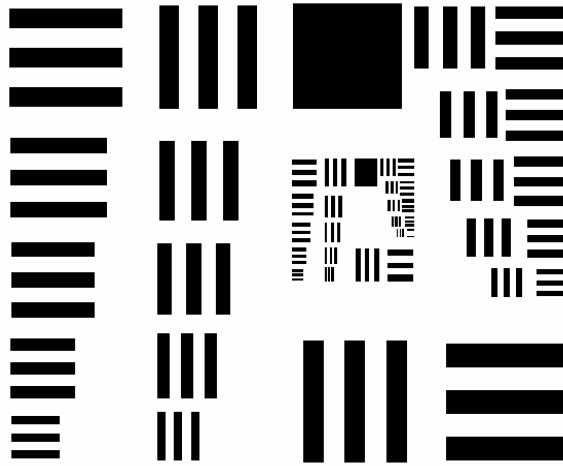


Figure 3.18 Pattern for MRTD measurement, known as USAF tri-bar resolution chart. [66].

When compared with NETD testing, MRTD testing evaluates the thermal camera's performance in more detail by including more effects of the system. However, real terrain conditions are still not included in the MRTD plots. Atmospheric turbulence, non-ideal emissivity of objects, external system noise in the field of operation, and other effects are not included in a laboratory MRTD test set-up. Hence, in order to test the performance of the infrared sensor in a dedicated thermal imager system, detailed field tests are inevitable.

## **CHAPTER 4**

### **QWIP ENSEMBLE MONTE CARLO SIMULATOR-VERTIGO**

This chapter presents a brief literature survey on QWIP modeling, followed by the introduction of the detailed ensemble Monte Carlo simulator constructed in this work. We will try to emphasize the need for such a detailed simulator by presenting the shortcomings of the previous modeling work for QWIP, which has been described as a “dirty device” by Liu in one of his review papers [11]. The QWIP characteristics are determined by a combination of mechanisms, which, are difficult to be incorporated into unsophisticated device models. While rough predictions on QWIP operation and characteristics can be achieved with simple models, a deeper understanding of the underlying physics, and the verification of the above predictions call for a detailed model capable of precisely simulating the complicated mechanisms in the MQW structure. The results of such a work should clearly be invaluable for optimizing the QWIP structure for better performance.

#### **4.1 Previous Work on QWIP Modeling/Simulation**

While the transport of the continuum electrons in QWIP needs sophisticated models due to far from equilibrium conditions and the reflection of electrons at the QW locations, an accurate description of the capture and emission mechanisms requires the realistic evaluation of the associated scattering rates. There has been a

significant effort toward analytical modeling of QWIPs, as well as numerical modeling based on the drift–diffusion model of electron transport [11,23,68-75]. However, the well-known limitations of the drift–diffusion model do not allow reliable investigation of the details of QWIP operation [76].

While hydrodynamic transport models have been used as more reliable alternatives to the drift–diffusion formulation for the simulation of semiconductor devices, the application of this approach to QWIPs is not straightforward. Conventionally, the energy-dependent parameters in these models are extracted from Monte Carlo simulations on bulk material. In the case of QWIPs, the extraction of these parameters is much more complicated due to the multi-quantum-well structure resulting in vertical transport significantly different than that in bulk material.

Ensemble Monte Carlo simulations are expensive in terms of computer time. However, the accuracy and detail achieved in turn make it worth using this technique for a thorough investigation of device operation, especially for devices such as QWIPs whose operation has not completely been understood. The Monte Carlo technique is also a useful tool for the optimization of such devices. There have been several reports on the Monte Carlo simulation of QWIPs [77-81]. These simulations, while not simulating the 2D electrons in the quantum wells, resolved various important aspects of QWIP operation. However, there is need for further work toward a better understanding of QWIP operation and characteristics through detailed Monte Carlo simulations. Reliable evaluation of some important device characteristics requires realistic modeling of capture and emission mechanisms, which are highly effective in determining the QWIP behaviour.

In this section, we will summarize the reported analytical models for QWIPs followed by the numerical models.

#### 4.1.1 Analytical Models

Analytical models usually employ the drift diffusion-model for bulk semiconductors by incorporating QWIP features into them. Quantum wells are modeled as sinks and sources of photoelectrons. Barriers are treated rather classically. Quantum mechanical electron reflection at the heterojunctions are usually ignored, but inherently defined in photoelectron escape probability.

Pan and Fonstad presented a simple model to calculate the energy band profile in QWIPs [68]. They considered quantum wells as reservoir of electrons and their ionized dopants. Using the capture-emission balance equation and current expression in the barriers, they estimated the charge density in each quantum well. Estimated charge allowed the calculation of QWIP band profile. However, the model assumed constant capture probability. One of their conclusions was that uniform electron accumulation occurs in the device under large bias.

Analytical model developed by Ryzhii *et al.* [69] is based on generation-recombination (G-R) equation in quantum well, drift equation on barriers and the contact injection model. Dark current, responsivity and band profile expressions were derived, and threshold voltage and power density were estimated. They calculated the characteristics of QWIPs with different numbers of quantum wells.

Analytical modeling of intersubband transitions in QWIPs is reported by Choi *et al.* [34,70]. Peak detection wavelength, the absorption line width, and the oscillator strength of a typical GaAs/Al<sub>x</sub>Ga<sub>1-x</sub>As multiple quantum well detector is calculated and compared with experimental QWIP characteristics.

Noise modeling of QWIPs mostly includes modeling G-R noise. It is related with the capture and escape dynamics of electrons, which are fundamental processes in novel quantum devices. Usual approach is relating noise gain to the capture probability. Beck [22] calculated the photoconductive gain, and generation-

recombination noise of quantum well infrared photodetectors. Liu and Levine calculated the photoconductive gain by using current continuity in the capture and escape paths [15,23]. Choi compared the above noise models, and related the noise gain to the photoconductive gain [24]. Schonbein *et al.* investigated and modeled the G-R noise and noise gain for photovoltaic QWIPs [26].

#### **4.1.2 Self-Consistent and Numerical Models**

The first Monte-Carlo simulation of QWIPs is reported by Artaki and Kizilyalli in 1991 [71]. All of the electrons in the device were modeled as purely 3D electrons. They concluded that including quantum mechanical well capture and escape rates should improve consistency of the model with experiments.

A numerical model based on the quantum well balance equation including tunneling of electrons, and noise model of electrons is presented by Thibaudau *et al.* [72]. Good agreement is obtained by fitting the dark current and noise of the detector to the experimental results. Ershov *et al.* [73,74] investigated the contact and distributed effects with a similar QWIP model. They explained nonlinear photoconductivity at high photoexcitation powers [75]

Ryzhii *et al.* [77-79] reported self consistent ensemble Monte Carlo simulations to study ultrafast electron transport in QWIPs. They showed that transient photocurrent triggered by a short infrared radiation pulse reveals a sharp peak followed by a relatively slow decay. This photocurrent peak was associated with the electron velocity overshoot effect.

Ryzhii *et al.* [80] presented the results of ensemble Monte Carlo simulation of vertical electron transport and capture process in AlGaAs/GaAs multiple QWIPs. Their Monte Carlo model takes into account various features of the conduction band structure, electron scattering parameters, and the interaction (reflection,

transmission and capture) of free electrons with the quantum wells. They showed that the heating of free electrons and their redistribution over the conduction band valleys under the influence of electric field plays an essential role in both the transport process and the capture into bound states in the quantum wells. They also calculated electron drift velocity and macroscopic capture parameter as functions of the structural parameters and applied electric field.

Ryzhii *et al.* [76] studied transient recharging effects in QWIPs triggered by step-like pulses of infrared radiation through ensemble Monte Carlo simulations. They showed that the excitation recharging waves can strongly affect the transient photocurrent and can result in the formation of stable or pulsating electric-field and charge domain structures.

The above QWIP Monte-Carlo simulations by Ryzhii *et al.* [76-80] were limited in the following way. Instead of including the photoexcitation directly in their work, they assumed current injection from each quantum well whose value depends on photoexcitation cross section, energy of the infrared pulse, photon energy, and sheet electron concentration. In their simulations, they simulated only 3D processes, and they did not take 2D processes into account, which are very important for QWIP operation. In our study, we include both 2D and 3D processes in detail in our Monte Carlo simulation program. We take size quantization both in  $\Gamma$  and L valleys into account, and simulate all the dominant 3D and 2D scattering mechanisms. Capture and photoexcitation are simulated as scattering events without using a phenomenological approach. The 2D scattering rates are calculated by using the wavefunctions obtained through the solution of Schrodinger's equation. Therefore, our results, while being complementary to those reported previously, are expected to be accurate enough to arrive to definite conclusions.

The QWIP ensemble Monte Carlo simulator reported in this thesis work will be described in the following sections.



## 4.2 VERTIGO- The QWIP Ensemble Monte Carlo Simulator

This section explains the developed QWIP simulation code by dividing it into several sections: wavefunction calculation, simulated devices, simulation approach, scattering rates and electron transport.

### 4.2.1 Wavefunction Calculation

The wavefunction calculation is an essential part in quantum device modeling. QWIPs have thin (several tens of angstroms) quantum wells surrounded with thicker (several hundreds of angstroms) large bandgap barriers. Large separation between the quantum wells allows to consider the electrons in the quantum wells as isolated [1]. These conditions constitute a finite quantum well problem which is handled by a numerical 1-D Schrodinger equation solver both in the  $\Gamma$  and L valley quantum wells of the AlGaAs/GaAs QWIP. In this solver, a 1D potential mesh is generated which has cells of length 1 Å. The Schrodinger equation is discretized in the form of a finite difference equation at every point of this mesh, and the finite difference equation is converted into a suitable matrix form. Using FORTRAN matrix solution routines, the eigenvalues and eigenvectors are obtained, which are the subband energy levels and subband wavefunctions of QWIP respectively. The above procedure can be summarized as follows.

The time-independent Schrodinger equation is

$$\left[ -\frac{\hbar^2}{2m^*} \frac{\partial^2}{\partial x^2} + V(x) \right] \varphi(x) = E \varphi(x) \quad (4.1)$$

with the following boundary conditions,

$$\begin{aligned}
\varphi|_{x=0} &= 0 \\
\left. \frac{\partial}{\partial x} \varphi \right|_{x=0} &= 0 \\
\varphi|_{x=L} &= 0 \\
\left. \frac{\partial}{\partial x} \varphi \right|_{x=L} &= 0
\end{aligned} \tag{4.2}$$

where “0” is the beginning of the first barrier and L is the end of the last barrier. The wavefunctions are solved on a single quantum well period of the device. This equation can be discretized in the following finite difference scheme

$$-\frac{\hbar^2}{2m^*} \frac{\varphi_{i+1} + \varphi_{i-1} - 2\varphi_i}{\Delta^2} + V_i \varphi_i = E \varphi_i \tag{4.3}$$

Rearranging the finite difference equation into matrix form, we obtain the following eigenequation

$$-\frac{\hbar^2}{2m^* \Delta^2} \begin{bmatrix} \left(-2 + \frac{2m^* \Delta^2}{\hbar} V_1\right) & 1 & 0 & & & 0 \\ & \dots & & & & \\ & 0 & 1 & \left(-2 + \frac{2m^* \Delta^2}{\hbar} V_i\right) & 1 & 0 \\ & & & \dots & & \\ & & & & 0 & 1 & \left(-2 + \frac{2m^* \Delta^2}{\hbar} V_N\right) \end{bmatrix} \begin{bmatrix} \varphi_1 \\ \vdots \\ \varphi_i \\ \vdots \\ \varphi_N \end{bmatrix} = E \begin{bmatrix} \varphi_1 \\ \vdots \\ \varphi_i \\ \vdots \\ \varphi_N \end{bmatrix} \tag{4.4}$$

This matrix equation is solved to find its eigenvalues (subband levels) and eigenvectors (wavefunctions). The numerical values of the solution is checked with the results of the harmonic quantum well.

#### 4.2.2 Simulated Device Structures and Material Parameters

Two QWIP structures with  $\text{Al}_{0.3}\text{Ga}_{0.7}\text{As}/\text{GaAs}$  (Device A) and  $\text{Al}_{0.15}\text{Ga}_{0.85}\text{As}/\text{GaAs}$  (Device B) material systems are simulated in this thesis (Figure 4.1). In addition,  $\text{Al}_{0.3}\text{Ga}_{0.7}\text{As}/\text{GaAs}$  QWIP structure is also simulated with reduced (halved) barrier effective mass (Device C) and with increased energy separations between the conduction band valleys of the barrier material corresponding to those of InP (Device D). The material parameters are compiled from various references [16,70,81-82].

The  $\text{Al}_{0.3}\text{Ga}_{0.7}\text{As}/\text{GaAs}$  standard QWIP structure is chosen from the work of Gunapala *et. al.* which reported successful operation of  $256 \times 256$  QWIP FPA [20]. The structure is illustrated in Figure 4.1(a). This structure is technologically important because many QWIPs similar to this structure are also demonstrated in other high performance imaging systems [2,3,7].

The energy band diagrams of one period of the simulated QWIP structures are shown in Figure 4.2. In all of the structures  $\Gamma$  and L valleys form quantum wells in the GaAs regions. On the other hand, the X valley forms a barrier in the GaAs well region. In the  $\text{Al}_{0.3}\text{Ga}_{0.7}\text{As}$  barrier region, the L and X valley minima are 33 meV close to each other, and these valleys are strongly coupled via intervalley scattering. Note that in the  $\text{Al}_{0.15}\text{Ga}_{0.85}\text{As}$  barriers the L-X separation is 118 meV.

For the  $\text{Al}_{0.3}\text{Ga}_{0.7}\text{As}$  ( $\text{Al}_{0.15}\text{Ga}_{0.85}\text{As}$ ) structure, the subband levels are calculated to be 89.5 meV (49.3 meV) in the well of  $\Gamma$  valley and 26.5 meV (15.0 meV) in the well of L valley, referenced to the corresponding valley minimum. The L valley wavefunction is more spread than that of  $\Gamma$  valley due to lower well depth in both structures.

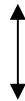
n <sup>+</sup> GaAs top contact	
500Å Al <sub>0.3</sub> Ga <sub>0.7</sub> As barrier, undoped	
44Å GaAs well, N <sub>D</sub> =4x10 <sup>17</sup> cm <sup>-3</sup>	 1 period
500Å Al <sub>0.3</sub> Ga <sub>0.7</sub> As barrier, undoped	
15 repeats of the period	
n <sup>+</sup> GaAs bottom contact	

Figure 4.1(a) Epilayer structure of the simulated Al<sub>0.3</sub>Ga<sub>0.7</sub>As/GaAs QWIP (Device A).


n <sup>+</sup> GaAs top contact	
500Å Al <sub>0.15</sub> Ga <sub>0.85</sub> As barrier, undoped	
60Å GaAs well, N <sub>D</sub> =4x10 <sup>17</sup> cm <sup>-3</sup>	 1 period
500Å Al <sub>0.15</sub> Ga <sub>0.85</sub> As barrier, undoped	
15 repeats of the period	
n <sup>+</sup> GaAs bottom contact	

Figure 4.1(b) Epilayer structure of the simulated Al<sub>0.15</sub>Ga<sub>0.85</sub>As/GaAs QWIP (Device B).

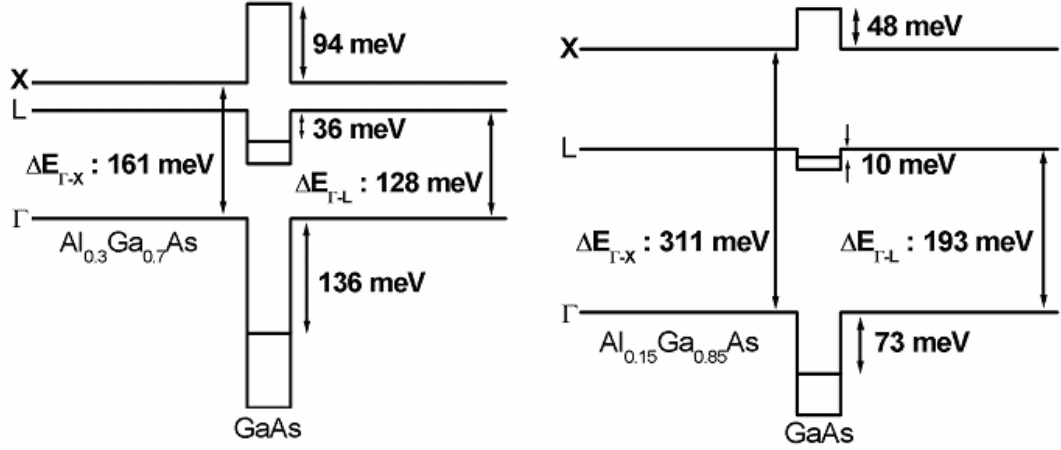


Figure 4.2 Energy band diagram of one period of the simulated  $\text{Al}_{0.3}\text{Ga}_{0.7}\text{As}/\text{GaAs}$  and  $\text{Al}_{0.15}\text{Ga}_{0.85}\text{As}/\text{GaAs}$  QWIP structures.

The additional QWIP structures are chosen to investigate the effect of barrier material parameters on device operation. First of them (Device C) is the above described  $\text{Al}_{0.3}\text{Ga}_{0.7}\text{As}/\text{GaAs}$  QWIP (Device A) with reduced (halved) electron effective mass in the barriers (Table 4.1). The second additional device (Device D) has the  $\text{Al}_{0.3}\text{Ga}_{0.7}\text{As}/\text{GaAs}$  QWIP (Device A) structure with increased barrier conduction band valley energy separations (Table 4.2). The valley separation values are matched to that of InP material to compare the result with the experimental reports on InP/InGaAs QWIPs. In both of the above artificial structures, the other parameters including the energy band discontinuities in  $\Gamma$ , L and X valleys are kept identical to that of the original  $\text{Al}_{0.3}\text{Ga}_{0.7}\text{As}/\text{GaAs}$  material system, in order to isolate the effects of the above parameters on QWIP performance and characteristics.

Each GaAs contact layer is n-doped at a density of  $4 \times 10^{17} \text{ cm}^{-3}$ . Other material parameters such as band nonparabolicity parameters, material E-k plots, dielectric constants, phonon energies and phonon deformation potentials are given in Appendix A.

Table 4.1 Electron effective mass values in  $\Gamma$ , L and X valleys in the barrier material of the simulated device structures.

	Device A and D	Device B	Device C
$m_{\Gamma}^*$	0.0847 $m_0$	0.0759 $m_0$	0.0424 $m_0$
$m_L^*$	0.230 $m_0$	0.226 $m_0$	0.115 $m_0$
$m_X^*$	0.422 $m_0$	0.501 $m_0$	0.211 $m_0$

Table 4.2 Energy separations of the  $\Gamma$ -L and  $\Gamma$ -X valleys in the barrier material of the simulated device structures.

	Device A and C	Device B	Device D
$\Delta E_{\Gamma L}$	128 meV	193 meV	590 meV
$\Delta E_{\Gamma X}$	161 meV	311 meV	931 meV

#### 4.2.3 Simulation Approach

The simulator code is developed in Microsoft FORTRAN Powerstation 4.0 environment. The simulator package consists of many subroutines. The auxiliary codes are explained in the Appendix C. The ensemble Monte-Carlo simulation program's compiled .exe file size is 577 Kilobytes. On a personal computer with 2 GHz central processing unit, running under Windows 2000 operating system, 1 ns simulation time takes approximately 10 computation hours.

Figure 4.3 shows the simplified flow chart of the ensemble Monte-Carlo simulator. The simulation flowchart obeys the structure explained in [83]. The simulation starts by distributing the electrons in the device and initializing the band profile. The simulation progresses with 1 fs time steps. At every time step, excess particles

at the contacts are removed or new particles are injected to keep the contacts charge neutral. Charge distribution in the device is calculated and Poisson's equation is solved to update the band profile and electric field with 20 fs intervals.

The particles are processed one by one during every 1 fs time step of the simulation. The device is divided into 4 Å cells. Each particle's transport time, energy, momentum, and velocity is calculated cell by cell during its free flight time in "Transport Loop" which is indicated in Figure 4.3. Any possible interception to the heterointerface is handled in this loop. When the particle's free flight time is completed, a probability axis from 0 to 1 is generated on which all the possible scatterings occupy a distance proportional to their probability. The total scattering rate, full-scale value on the probability axis, used in this simulation is  $8 \times 10^{14} \text{ s}^{-1}$  for the  $\text{Al}_{0.3}\text{Ga}_{0.7}\text{As}/\text{GaAs}$  structure and  $2 \times 10^{14} \text{ s}^{-1}$  for the  $\text{Al}_{0.15}\text{Ga}_{0.85}\text{As}/\text{GaAs}$  structure. After the probability axis is generated, a random number between 0 and 1 determines the scattering to be executed. In Figure 4.3 the processes shown as "Scattering routine in well material " and "Scattering routine in barrier material" handle the execution of this randomly chosen scattering event.

#### **4.2.4 Electrostatic Calculations, Initial Conditions and Boundary Conditions**

The Poisson's equation is solved on a discrete mesh. The device is divided into 4 Å cells. The simulator uses cloud-in-the-cell (CIC) method to find the charge distribution on this mesh [84]. This charge distribution is used to solve the 1D Poisson equation with 20 fs intervals by successive integration which is explained in Appendix B [85]. In this 1D structure, each superparticle corresponds to  $4 \times 10^8 \text{ cm}^{-2}$  sheet charge density in a 4 Å cell, which is equivalent to  $10^{16} \text{ cm}^{-3}$  volume charge density. Reducing this supercharge value increases the accuracy of the simulation. However, the supercharge value is limited by the maximum number of particles that

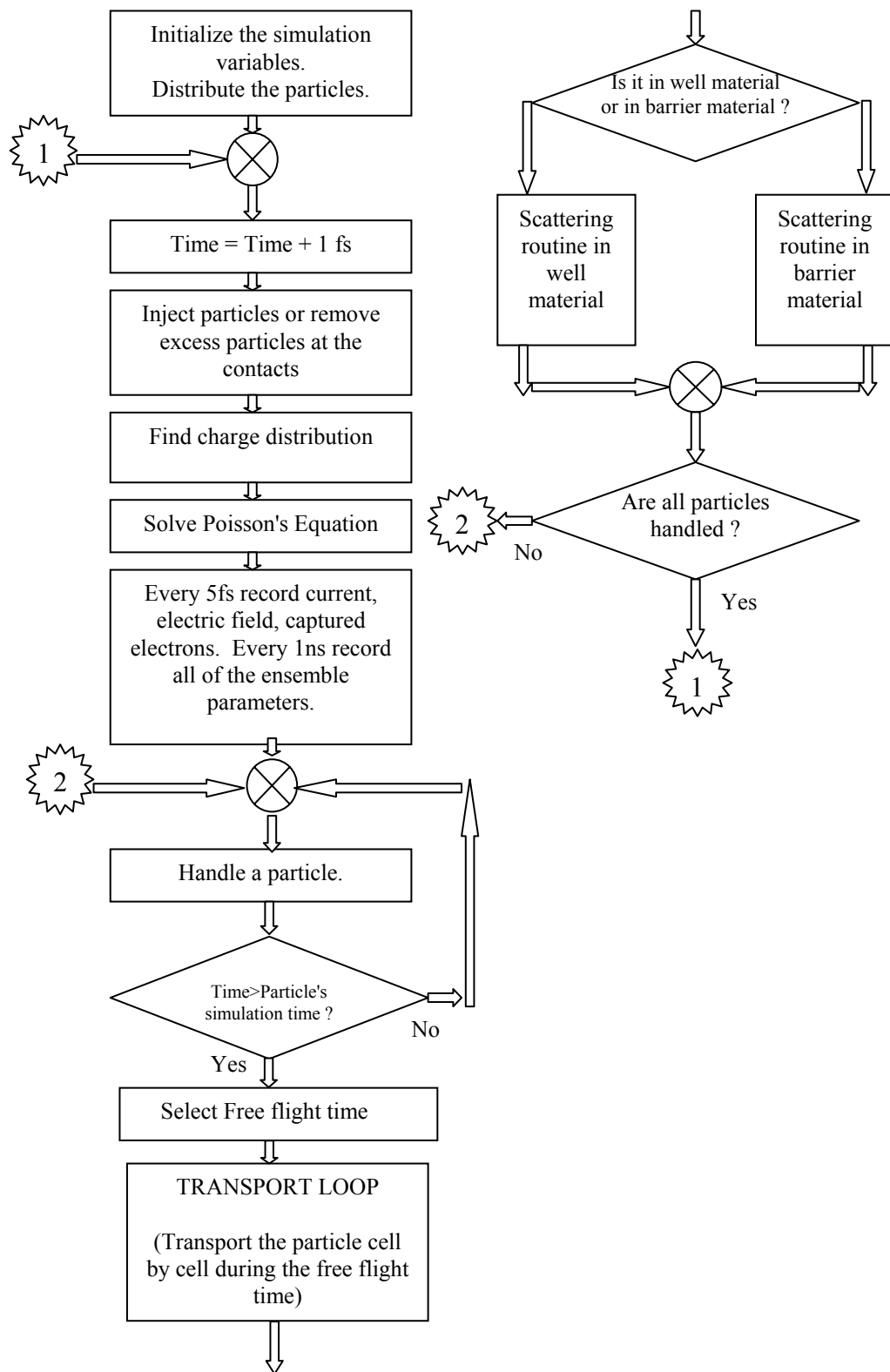


Figure 4.3 Simplified flowchart of the Monte-Carlo simulator.



can be simulated on a personal computer. Simulating the 2D electrons in quantum wells calls for the simulation of approximately 10000 particles. Even under this heavy load, the supercharge value is still comparable to those reported in the literature [77].

The Neumann boundary conditions at the emitter and the collector assumes perfectly neutral ohmic contacts, hence it assumes zero electric field there. Injecting new particles or deleting excess particles every 1 fs satisfies this condition.

Initially the first 500 Å barrier has 200 mV drop on it, the quantum well regions are at zero electric field, and the rest of the potential drop is shared equally among the other barriers. This initial band profile is close to the steady state condition under most of the applied bias voltages, and this decreases the required computational time considerably. The particles are initially distributed according to the doping profile in the device. The barrier electrons are distributed in the  $\Gamma$  valley with randomized momentum vectors with kinetic energy of  $\frac{3}{2}kT \ln(r)$  where  $0 < r < 1$  is a random number [83].

#### **4.2.5 Calculating Particle Trajectory and Ensemble Parameters**

The motion of the particles are calculated using their quasi-momentum vectors and free flight times. In each 4 Å wide cell, the electric field is assumed to be constant and the motion of the electrons is calculated under this constant field in a single cell.

Valley occupancy ratios of electrons,  $P_{\Gamma}$ ,  $P_L$ ,  $P_X$ , in each cell is calculated by dividing the valley free flight time in that cell to the total free flight time all valleys. The velocity of electrons in each valley is calculated at each cell by recording the energy gained or lost by each electron during the free flight time according to the following equation

$$v_j = \frac{-\sum (E_f - E_i)}{qF \sum \tau_j} \quad (4.5)$$

where  $E_f$  and  $E_i$  are the initial and final energies of the electron when it accelerates or decelerates in the 4 Å cell,  $j$  is the valley index and  $F$  is the electric field in the cell.  $\sum \tau_j$  is the total free flight time in  $j^{\text{th}}$  valley of that cell.

The average velocity in each cell is calculated by  $v = v_\Gamma P_\Gamma + v_L P_L + v_X P_X$ . The average energy of the electrons are calculated using the average energies of the particles during the free flight times weighted by the duration of free flight. After determining the average electron energy in each valley, the particle energy in each cell is calculated as  $E = E_\Gamma P_\Gamma + (E_L + \Delta E_{\Gamma L}) P_L + (E_X + \Delta E_{\Gamma X}) P_X$ .

#### 4.2.6 Heterojunction Treatment

The heterojunctions are modeled as abrupt energy steps in the crystal growth direction. Figure 4.4 illustrates different conditions when the electron approaches a heterojunction. When this happens, the following procedure is followed. If the electron's energy associated with the momentum in the crystal growth direction (z-direction) is less than the energy step value, the electron is reflected back by reflecting its momentum in z direction only (Figure 4.4(a,b)). Otherwise, the electron is checked to pass the single heterojunction quantum mechanically. Since this is a particle simulation, the electron's particle wave approaching the quantum well with closely spaced double heterointerfaces cannot be simulated. Instead of this, the transmission probability at a single heterojunction is calculated as [86]

$$T = \frac{4 \frac{k_z'}{k_z} \frac{m^*}{m^{*'}}}{\left(1 + \frac{k_z'}{k_z} \frac{m^*}{m^{*'}}\right)^2} \quad (4.6)$$

where primed variables represent variables in the target layer. This probability is applied to electrons that may be able to pass the heterojunction classically. If this random process does not result in transmission, the electron's z-momentum is reflected back (Figure 4.4(b)). Otherwise, the electron is transferred across the heterojunction, and its z-momentum and energy are updated as follows (Figure 4.4(c))

$$\begin{aligned}
 E' &= E \pm \Delta E \\
 E_{xy} &= \frac{\hbar^2 k_{xy}^2}{2m^{*'}} \\
 k_z' &= \frac{\sqrt{2m^{*'}(E' - E_{xy})}}{\hbar}
 \end{aligned} \tag{4.7}$$

where primed variables again represent the variables in target layer,  $k_{xy}$  is the electron momentum parallel to the heterointerface,  $m^{*'}$  is the electron effective mass in the related conduction band valley of the target material, and  $\Delta E$  is the energy step seen by the electron when it drifts from the source layer to target layer. When the electron passes a heterojunction, the electron momentum parallel to the heterointerface is conserved, however the momentum in crystal growth direction is affected by the heterojunction.

#### 4.2.7 Tunneling at Emitter and X Valley Barrier

Tunneling of electrons at the emitter barrier and X valley barrier is modeled in the simulation using WKB approximation [87]. The electrons hitting these barriers are transmitted to the opposite side of the barrier with the same energy and momentum if the following calculated probability holds :

$$P \cong \exp \left[ -2 \int_{x_1}^{x_2} |k(x)| dx \right] \tag{4.8}$$

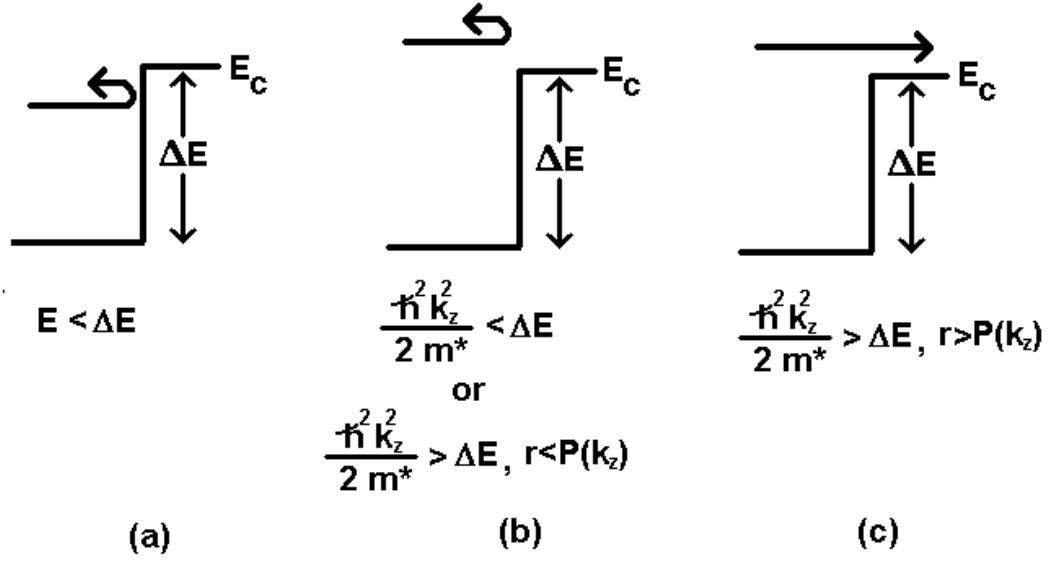


Figure 4.4 When an electron approaches an heterojunction its total energy may not be enough to overcome the energy barrier (a). Also, even if the electron's total energy is larger than the energy step, electron's kinetic energy corresponding to the crystal growth direction may be smaller than the energy step (b). If kinetic energy corresponding to momentum in the growth direction is larger than the barrier, the electron may still be reflected back with the quantum mechanically defined probability (c). Here "r" is a random number and  $P(k_z)$  is the transmission probability. If all of the above conditions are satisfied, the electron is allowed to pass the heterojunction.

where,  $k(x) = \sqrt{2m^*(\phi_b(x) - KE)/\hbar^2}$  is the absolute value of the wave vector of the electron in the barrier,  $x_1$  and  $x_2$  are the initial and final position of the tunneled electron.  $\phi_b$  is the energy barrier seen by the tunneling electron and,  $KE$  is the kinetic energy of the tunneling electron in the growth direction.

#### 4.2.8 Electron Scattering

The electron dynamics in the barriers and in the quantum wells are modeled differently due to the presence of 2D states in the quantum wells. The barrier

electrons are subjected to following purely 3D scattering events [85,88,89]: polar optical phonon scattering, acoustic phonon scattering, equivalent and nonequivalent intervalley scattering, ionized impurity scattering, and alloy scattering. Calculation of these 3D scattering rates are given in Appendix C.

The electrons in the GaAs well regions are subjected to 3D-to-3D, 3D-to-2D and 2D-to-2D scatterings. The  $\Gamma_{2D}$  and  $L_{2D}$  bound states are modeled as purely 2D states while each valley's continuum states are modeled as purely 3D states (named as  $\Gamma_{3D}$ ,  $L_{3D}$ , and  $X_{3D}$ ). Figure 4.5 shows the naming convention of these modeled states.

#### 4.2.9 3D Electrons in the Quantum Well Region

The 3D electrons in the well regions are subjected to the above mentioned 3D barrier scatterings (excluding alloy scattering). The continuum and bound states in the well region interact via 2D $\leftrightarrow$ 3D scattering mechanisms.  $\Gamma_{3D}$  and  $L_{3D}$  electrons can be captured to their own quantum wells by optical phonon scattering [90]. Moreover,  $\Gamma_{3D}$  and  $L_{3D}$  electrons can scatter to  $\Gamma_{2D}$  and  $L_{2D}$  states via non-equivalent intervalley scattering [91]. The major transition paths between the 2D and 3D states are shown in figure 4.6.

#### 4.2.10 2D Electrons in the Quantum Well Region

The 2D electrons in the  $\Gamma_{2D}$  bound state of the quantum well are subjected to 2D-to-3D and 2D-to-2D scatterings.  $\Gamma_{2D}$ -to- $\Gamma_{2D}$  scatterings are modeled as polar optical phonon scattering including dielectric screening [85,88,89,92], remote and background ionized impurity scattering [89], and acoustic phonon scattering. The  $\Gamma_{2D}$ -to- $L_{2D}$  scattering is modeled as intervalley scattering [93]. 2D-to-3D scatterings from  $\Gamma_{2D}$  state occurs by photoexcitation to  $\Gamma_{3D}$  state, optical phonon

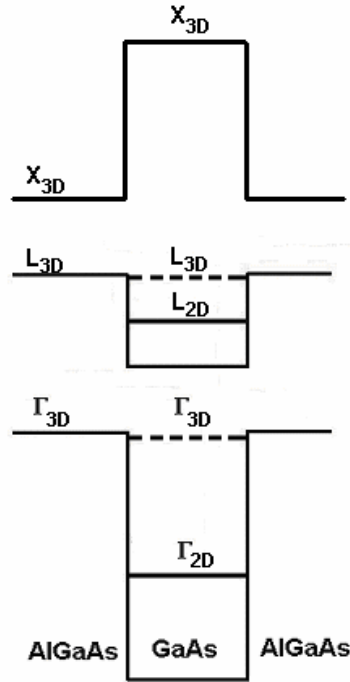


Figure 4.5 Naming convention of the modeled states in the simulated QWIP.  $\Gamma_{3D}$ ,  $L_{3D}$  and  $X_{3D}$  states are purely 3D continuum states while  $\Gamma_{2D}$  and  $L_{2D}$  are modeled as 2D bound states.

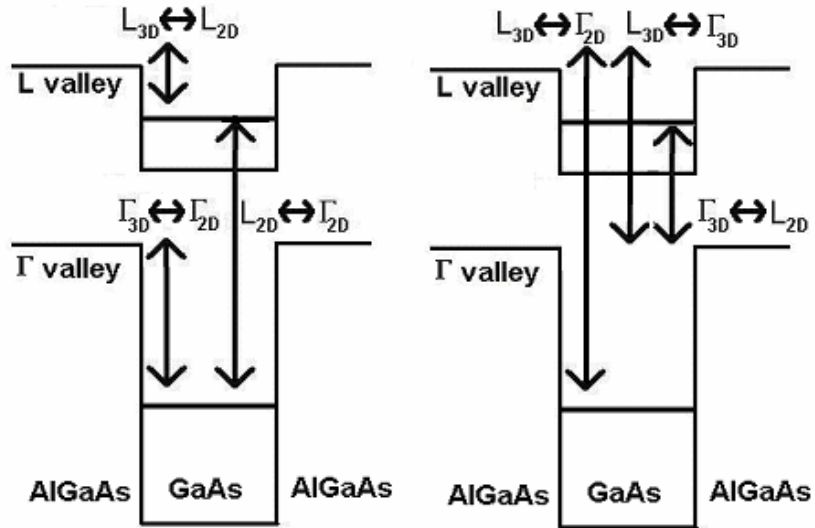


Figure 4.6 Representation of electron scattering between continuum,  $\Gamma_{2D}$ , and  $L_{2D}$  states.

scattering to  $\Gamma_{3D}$  state [90] and intervalley scattering to  $L_{3D}$  state and X valley [91]. The formulations of these scattering rates are given in Appendix C.

The modeling of the L valley bound state is similar to that of the  $\Gamma_{2D}$  state. 2D-to-2D scatterings included for this state are polar optical phonon scattering including dielectric screening [92], acoustic phonon scattering, remote and background ionized impurity scatterings [88-89], equivalent intervalley scattering in  $L_{2D}$  state, and non-equivalent intervalley scattering to  $\Gamma_{2D}$  state [93]. 2D-3D scatterings are optical phonon scattering to  $\Gamma_{3D}$  state [90] and intervalley scatterings to  $\Gamma_{3D}$  state,  $L_{3D}$  state and X valley [91].

The 2D-3D scattering rates are especially important in QWIP operation since they allow ejection of a bound 2D electron into the conduction path. The photoexcitation is also modeled as a scattering event. The photoexcitation rate used in the simulations is  $10^{10} \text{ sec}^{-1}$ . Monte Carlo simulation of QWIPs under very low photoexcitation rates is impractical due to the large amount of time required to reach steady-state. The above photoexcitation rate results in photocurrent much larger than the dark current. However, the selection of this rate is still reasonable, since under the above rate, the barrier electron density remains low enough not to considerably affect the electric field distribution in the device. Under the above photoexcitation rate, the e-field in the main body of QWIP may be slightly smaller than that under near-dark conditions due to larger voltage drop near the emitter contact [94]. However, we do not expect this condition to affect the conclusions of this work. The above rate is also sufficiently below that required for saturation of intersubband absorption [94]. Furthermore, this work focuses on the transport and capture of the excited carriers, and thermally and photoexcited carriers are expected to have similar energy distributions and properties [68].

## CHAPTER 5

### SIMULATION RESULTS AND DISCUSSION

This chapter presents detailed results of QWIP Monte Carlo simulations. The simulations were run with the device structure and the device model explained in the preceding chapter. The advantage of simulating both 3D and 2D electrons in the device allowed us to explore the capture paths preferred by the electrons in the device, an information that was not available in the previously reported QWIP simulators [76-80]. The results of our simulations also allowed better explanations of bias dependency of gain, lifetime, and electron velocity, as well as charge accumulation and domain formation in QWIP [17, 95-96].

#### 5.1 Band Profile and Electric Field Domain Formation

For the simulated  $\text{Al}_{0.3}\text{Ga}_{0.7}\text{As}$  QWIP structure (Device A as described in the preceding chapter), figure 5.1 presents the variation of the energy band diagram with bias, and figure 5.2 shows the bias dependence of the average E-field in each barrier. The charge in each well determines the difference between the E-fields in the barriers neighbouring the well. Under small bias, most of the applied voltage drops on a small region near the emitter, and weak E-fields exist in the rest of the device as previously observed using simpler models [68,73]. The rate of increase of the emitter E-field with bias is decreased as the bias is increased due to the tunnelling nature of injection from the emitter. As a result of the smaller rate of



increase in the emitter E-field when compared with that in the following barriers, the depletion in the first well is decreased with increasing bias. The emitter E-field determines the amount of current injected into the device, while the field in the bulk adjusts itself to carry the same amount of current in the main body of QWIP. Since the current is formed by different physical mechanisms at the contact and at the bulk of QWIP, the rate of change of the emitter field with bias is different than that in the rest of the device [68].

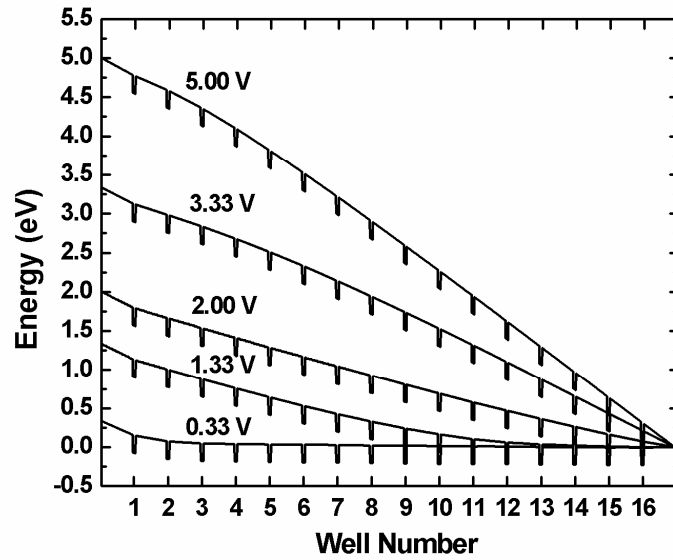


Figure 5.1 Energy band diagrams under various bias voltages [95].

As shown in figure 5.3, the barrier electron velocity (averaged through the barrier) is saturated throughout the entire main body of QWIP under 2V bias. Beyond this bias voltage, uniform and almost bias independent barrier velocity results in uniform barrier electron density that increases with increasing bias to comply with the increasing device current. This also results in increasing well electron concentration with increasing bias, and well accumulation occurs under large bias. Uniform well accumulation in QWIPs under large bias was predicted by Pan and

Fonstad [68], and E-field domain formation was predicted by Schneider *et al* [97]. Our results show that accumulation occurs nonuniformly being highest near the emitter. This accumulation is necessary to keep the emitter field at the proper value required to inject the corresponding current. Under field independent capture probability ( $p_c$ ) as assumed by Pan and Fonstad [68], well accumulation occurs uniformly. When the E-field dependence of  $p_c$  is accounted, the accumulation is observed to occur nonuniformly being highest near the emitter. Assuming that  $p_c$  decreases with increasing barrier E-field in the region of interest, it decreases with distance toward the collector resulting in decreasing well accumulation in the same direction. At a certain location in the device, well accumulation disappears, and the E-field and  $p_c$  remain almost constant beyond this point. While the E-field in this region increases with bias, the wells are kept almost neutral (uniform E-field) in spite of the increasing device current due to decreasing  $p_c$  with increasing E-field.

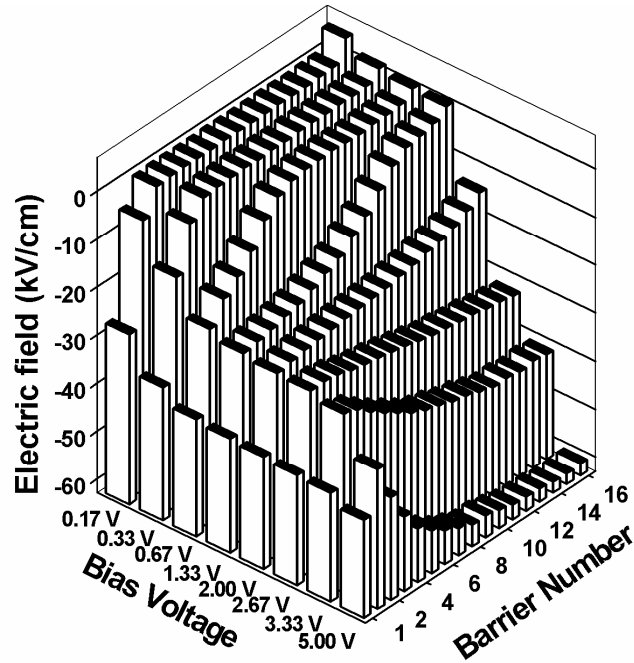


Figure 5.2 Variation of average E-field on each barrier with bias [17].

## 5.2 Barrier electron velocity

It is generally assumed that electrons travel with saturated velocity in the bulk of QWIP under sufficiently large bias. The electron velocity in the barriers under 2 V bias is shown in the inset of figure 5.3, which displays high nonuniformity through the barrier. Figure 5.4 shows the valley occupancies in the barriers under various bias voltages. Significant portion of the barrier electrons reside in the L and X valleys of AlGaAs even under typical bias voltages. Under 2V bias which yields relatively uniform E-field (see figure 5.2), the valley occupancies are nearly periodic as well as the electron velocity as shown in the inset of figure 5.3. The X valley occupancy peaks near the end of the barriers should be understood as an ensemble effect due to the presence of X valley barriers in the QW locations; these peaks are not due to rapid intervalley transfer of individual electrons travelling through the barriers.

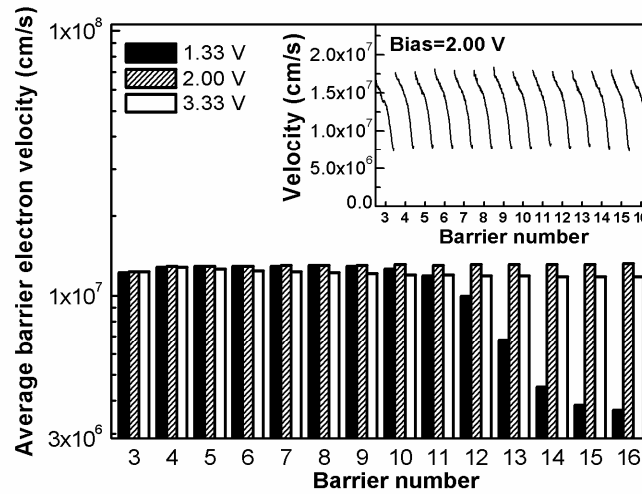


Figure 5.3 Average barrier electron velocity under various bias voltages. The inset shows the electron velocity profile through the barriers under the bias voltage of 2 V [17].

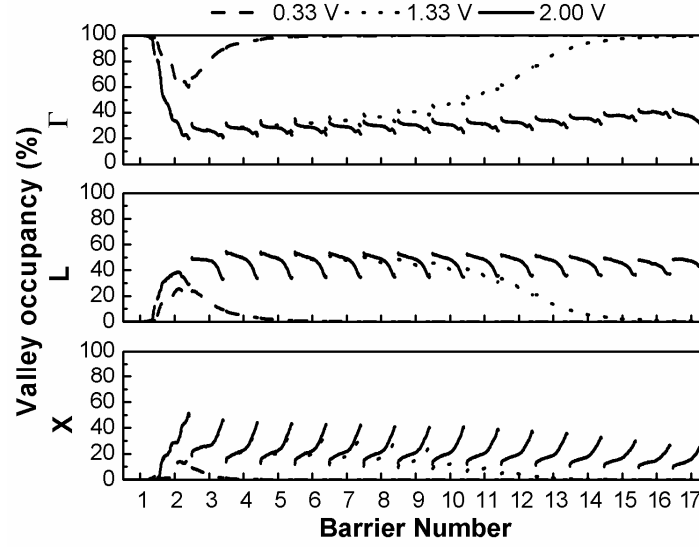


Figure 5.4 Valley occupancies in the barriers under various bias voltages [17].

Figure 5.5 shows the average electron velocity in the 9-12<sup>th</sup> barriers under 3.33 V bias, where the E-field is large enough to saturate the electron velocity in bulk  $\text{Al}_{0.3}\text{Ga}_{0.7}\text{As}$ . The solid line represents the average velocity of the electrons excited from the 8<sup>th</sup> well. The dotted line represents the average velocity of all of the barrier electrons. The 77 K saturated electron velocity in bulk  $\text{Al}_{0.3}\text{Ga}_{0.7}\text{As}$  is also shown in the figure. While the electrons travel with a velocity larger than the saturated velocity through most of the barrier, the electron velocity is significantly degraded near the end of the barrier due to the reflection of the electrons at the AlGaAs/GaAs interfaces. The velocity of the electrons that are excited from the 8<sup>th</sup> well significantly overshoots in the 9<sup>th</sup> barrier, and becomes comparable to the average barrier electron velocity in a distance of two periods. The velocity overshoot in the 9<sup>th</sup> barrier is due to the large E-field faced by the excited electrons, and subsequent scattering of these electrons to higher lying valleys. The valley occupancies of the electrons excited from the 8<sup>th</sup> well are shown in the inset of figure 5.5. The distribution of the photoexcited electrons to conduction band valleys also adopts the periodicity of the QWIP in a distance of two periods from the well of excitation.

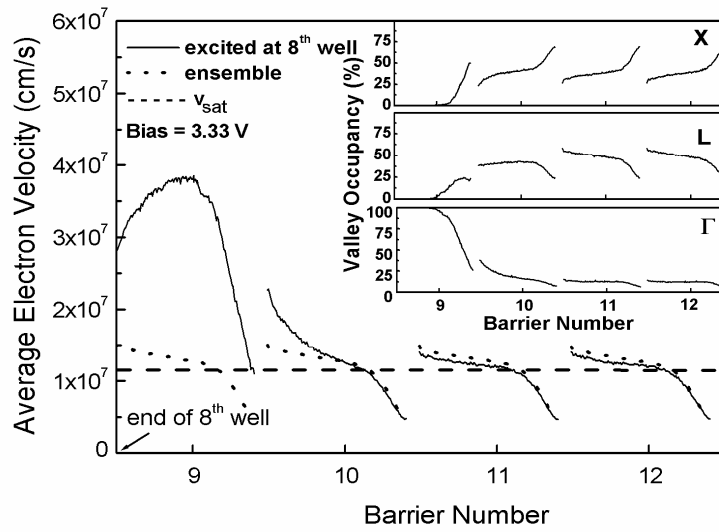


Figure 5.5 Average electron velocity in the barriers 9-2 under 3.33 V bias (dotted line), and average velocity of the electrons in bulk  $\text{Al}_{0.3}\text{Ga}_{0.7}\text{As}$  is shown by the dashed line. The inset shows the valley occupancies of the electrons excited from the eighth well [17].

The important factors that may make the barrier electron velocity in AlGaAs/GaAs QWIP different than the saturated electron velocity in bulk AlGaAs are the velocity overshoot of the electrons excited from the preceding wells and the reflections of the barrier electrons at the AlGaAs/GaAs interfaces. The degree of increase in the average barrier electron velocity due to velocity overshoot depends on the barrier E-field and barrier properties as well as on the photoexcited carrier lifetime. Figure 5.6 shows the average barrier electron velocity versus average barrier E-field obtained through simulations under various bias levels. Figure 5.6 also includes the 77K electron velocity-field characteristic of  $\text{Al}_{0.3}\text{Ga}_{0.7}\text{As}$  calculated from Monte Carlo simulations on bulk material. It should be noted that figure 5.6 may not strictly reflect the field dependence of the barrier electron velocity under very large E-field gradients due to nonlocal heating effects. Under high E-fields, the average barrier electron velocity is close to the saturation velocity in bulk  $\text{Al}_{0.3}\text{Ga}_{0.7}\text{As}$ , and only slight velocity overshoot is observed in the barrier electron velocity-field

characteristic. Similar behaviour can be expected in AlGaAs/GaAs QWIPs with comparable Al mole fractions. The E-field dependence of the barrier electron velocity can be described as

$$v(E) = \frac{\mu E + v_{sat} (E/E_c)^3}{1 + (E/E_c)^3} \quad (5.1)$$

where  $E_c=13$  kV/cm,  $v_{sat}=1.07 \times 10^7$  cm/s and  $\mu=1150$  cm<sup>2</sup>/V-s.

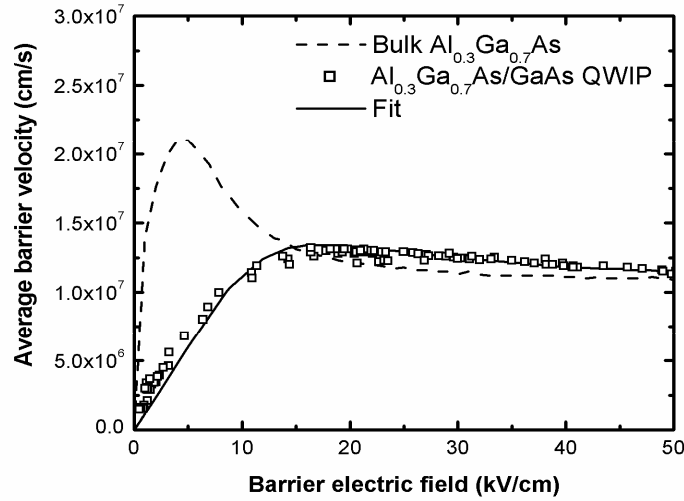


Figure 5.6 Barrier electron velocity (averaged through the barrier) versus average barrier E-field. The data are mapped from the results of simulations performed under various bias voltages. The electron velocity E-field characteristic of bulk  $\text{Al}_{0.3}\text{Ga}_{0.7}\text{As}$  at 77K is shown by the dashed line [17].

It is generally assumed that the electron velocity increases linearly with E-field under low fields ( $v=\mu E$ ), and it is equal to the saturated electron velocity under large fields [68]. Based on the above results, while this approach seems to be

appropriate, at least for QWIPs similar to the one used in this work, the low field electron mobility is significantly lower than that in bulk AlGaAs. Our results are consistent with experimental observations reporting vertical mobilities significantly lower than that in bulk material [95].

### 5.3 Electron capture

The role played by the L valley QW in electron capture is usually ignored in QWIPs [78]. While L valley QW is relatively shallow in LWIR AlGaAs/GaAs QWIPs, considerable portion of the barrier electrons reside in L valley even under typical bias voltages as shown in figure 5.4. Furthermore, POP emission rate in this valley is higher than that in  $\Gamma$  valley, and  $\Gamma$  valley continuum electrons have higher kinetic energy due to faster heating during their transport in the barriers resulting in lower capture probability. Therefore, capture to  $\Gamma$  QW through L valley QW may be an important mechanism limiting the gain of QWIP. In this work, the importance of capture through L-valley has been confirmed through detailed tracking of the electrons reaching the GaAs well regions. Figure 5.7 shows the normalized number of electrons that enter each GaAs well region in  $\Gamma$  and L valleys and are captured in the  $\Gamma$  valley QW in the same region under 1.33 V bias. In the regions of the device where L and  $\Gamma$  valley populations are comparable (see figure 5.4), most of the captured electrons originate from L valley. Most of these electrons are first captured by the L valley QW by 3D $\rightarrow$ 2D phonon emission before they make transition to the  $\Gamma_{2D}$  state. In the regions close to the collector, number of the electrons captured from the  $\Gamma$  valley is larger due to the decreasing L valley population and increasing capture probability of the  $\Gamma$  electrons with decreasing field (see figure 5.2).

The above conclusion is contradictory to the previous approaches relating the capture to the  $\Gamma_{2D}$  state mostly to  $\Gamma_{3D}$  electrons losing energy by polar optical phonon emission [98,78]. In the Monte Carlo simulations by Ryzhii *et al* [98], capture of L-valley electrons into their own QWs was ignored assuming that L-

valley QW electrons are quickly transferred to  $\Gamma$  valley. However, a significant portion of these electrons is scattered to  $\Gamma_{2D}$  state, and quickly lose energy in this state by intra-subband phonon emission, eventually being captured in the  $\Gamma$  QW. Those electrons scattering to the  $\Gamma_{3D}$  states are not unlikely to be captured in the  $\Gamma$  QW due to their relatively small momenta in the crystal growth direction.

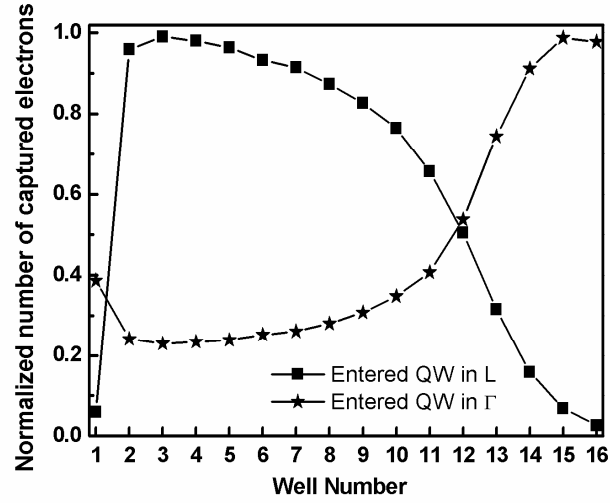


Figure 5.7 Normalized number of electrons that enter the GaAs QW region in  $\Gamma$  and L valleys and are captured into the same QW of the  $\Gamma$  valley under 1.33 V bias [17].

The importance of the role played by the L valley in electron capture suggests that the excited electron lifetime and the gain be considerably dependent on the  $\Gamma$ -L energy spacings in the heterostructure material system forming the QWIP epilayer structure. This issue will be discussed and supported by experimental reports in the following subsection.



## 5.4 QWIP gain

The calculated bias dependence of the gain, the average electron velocity in the device and valley occupancies are shown in figure 5.8. The gain is calculated by dividing the number of electrons injected into the device by the total number of the excited electrons that escape from QWs, which is equal to the total number of captured electrons at steady-state [22].

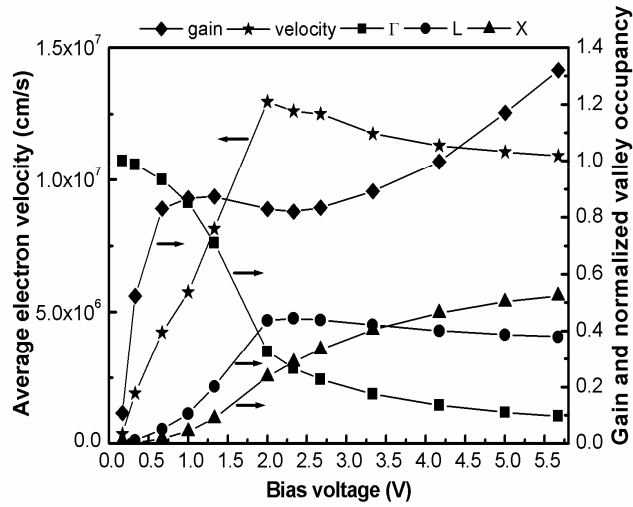


Figure 5.8 Calculated bias dependence of average electron velocity, gain, and valley occupancies [17].

There has been considerable amount of work on the investigation of QWIP gain by extracting it from noise measurements [15,32,97,99-102]. However, the dependence of the gain on bias is still a controversial issue. Levine *et. al.* [15] and Schneider *et. al.* [97] observed strong negative differential change in the gain of 50-well  $\text{Al}_{0.26}\text{Ga}_{0.74}\text{As}/\text{GaAs}$  QWIPs. Levine *et al* [15] attributed the negative differential change in the measured gain to ground state sequential tunnelling, while Schneider *et al.* [97] related it to the degradation of transport properties through intervalley transfer in the barriers. Sequential tunnelling is not included in our simulations.

However, the details of electron transport are incorporated into our simulator, and slight negative differential change is observed in the calculated gain. In a similar QWIP (50-well,  $\text{Al}_{0.25}\text{Ga}_{0.75}\text{As}/\text{GaAs}$ ), Levine *et. al.* [15] observed no negative differential change and saturation of gain around 2 V which is in acceptable agreement with our results, when the bias is scaled.

Experimental results on  $\text{InP}/\text{In}_{0.53}\text{Ga}_{0.47}\text{As}$  and  $\text{GaAs}/\text{In}_x\text{Ga}_{1-x}\text{As}$  QWIPs yielded gains significantly larger than those achievable with  $\text{AlGaAs}/\text{GaAs}$  QWIPs [1,72,94,100,101]. The gain is usually observed to saturate under relatively small bias in  $\text{AlGaAs}/\text{GaAs}$  QWIPs, and much higher gain in  $\text{InP}/\text{In}_{0.53}\text{Ga}_{0.47}\text{As}$  and  $\text{GaAs}/\text{In}_x\text{Ga}_{1-x}\text{As}$  QWIPs is achieved only under large bias [99,101]. Jelen *et. al* [99] reported saturated gain as high as 50 in 20-well  $\text{InP}/\text{In}_{0.53}\text{Ga}_{0.47}\text{As}$  QWIPs under 3V bias. This gain is around 50 times larger than the typical gain in a 20-well  $\text{Al}_x\text{Ga}_{1-x}\text{As}/\text{GaAs}$  QWIP with  $x\sim 0.3$ . The above observations were attributed to high quality binary InP and GaAs barriers and the higher mobility of InP and GaAs compared with AlGaAs [1,99-101]. However, neither the low field nor the high field electron velocity in InP is expected to be 50 times larger than that in device quality  $\text{Al}_{0.3}\text{Ga}_{0.7}\text{As}$ . Based on our results, very large difference between the gains observed in  $\text{AlGaAs}/\text{GaAs}$  and  $\text{InP}/\text{In}_{0.53}\text{Ga}_{0.47}\text{As}$  (or  $\text{GaAs}/\text{In}_x\text{Ga}_{1-x}\text{As}$ ) QWIPs seems to be related with the dissimilarity of the capture dynamics of the electrons through the differences in the conduction band structures of these heterostructure material systems. As an example, both  $\text{InP}/\text{In}_{0.53}\text{Ga}_{0.47}\text{As}$  and  $\text{GaAs}/\text{InGaAs}$  material systems have significantly larger  $\Gamma$ -L energy spacing resulting in a lower L valley occupancy when compared with that in  $\text{Al}_{0.3}\text{Ga}_{0.7}\text{As}/\text{GaAs}$  under the same bias voltage. While a larger  $\Gamma$ -L spacing increases the critical field at which the peak electron velocity is achieved, it also increases the E-field at which the capture path through the L-valley becomes effective. Due to smaller  $\Gamma$ -L energy spacing in  $\text{Al}_x\text{Ga}_{1-x}\text{As}/\text{GaAs}$  QWIPs with  $x\sim 0.3$ , the rate of increase of gain with bias starts to decrease under relatively small bias. Based on the above arguments, considerable improvement in the gain can be expected if the barrier Al mole fraction ( $x$ ) in  $\text{Al}_x\text{Ga}_{1-x}\text{As}/\text{GaAs}$  QWIPs is decreased to have larger  $\Gamma$ -L energy spacing in the

barrier and a shallower L valley QW. Indeed, 50-well  $\text{Al}_{0.1}\text{Ga}_{0.9}\text{As}/\text{GaAs}$  QWIPs yielded gain values [32] higher than that achievable with  $\text{Al}_{0.3}\text{Ga}_{0.7}\text{As}/\text{GaAs}$  QWIPs without displaying saturation in the measurement range of 0-3 V.

It is generally believed that gain saturation occurs due to velocity saturation in QWIPs [15]. However, as shown in figure 5.8, gain peaks well before the average electron velocity in the device peaks. This is an expected result based on the above conclusion. An electron's mobility decreases when it is scattered to L valley. The other effect of transferring to L valley is increased capture probability and decreased electron lifetime. While we observe slight negative differential change in the gain-bias characteristic, stronger negative differential change can be expected in the case of larger rate of increase in the capture probability with increasing bias, which may occur in the presence of stronger capture through the L valley QW. As seen from figure 5.8, gain starts to increase with bias under large bias (above  $\sim 3$  V). Similar behaviour was experimentally observed through noise measurements by other groups [102-104], and the gain rise under large bias was attributed to avalanche multiplication, which is not included in our simulations. Based on our results, this behaviour may, at least partially, be attributed to the increase in the lifetime of the electrons in the satellite valleys as they gain more energy from the increasing E-field.

## **5.5 Dependence of Gain, Electron Velocity and Excited Electron Lifetime on QWIP Material Parameters**

The gain of QWIPs is usually extracted from noise measurements [15,32,97,99, 101,102,105]. The gain can be expressed as  $L_d/L$  where  $L_d$  is the drift distance of the excited electrons, and  $L$  is the total device length. Figure 5.9 compares the drift distances versus average electric field in device extracted from measured gains reported by different groups for various QWIPs [32,94,97,101,103]. The gain of  $\text{Al}_x\text{Ga}_{1-x}\text{As}/\text{GaAs}$  QWIP with  $x \sim 0.3$  usually exhibits negative differential change

beyond  $\sim 2$  V for a 50-well device [15,97]. The negative differential change in the gain was attributed to ground state sequential tunnelling by Levine *et al.* [15] and to the degradation of transport properties through intervalley transfer in the barriers by Schneider *et al* [97]. However,  $\text{Al}_x\text{Ga}_{1-x}\text{As}/\text{GaAs}$  QWIPs with lower barrier Al mole fractions show relatively high gain under large bias without displaying negative differential change [32,102].

Under large bias,  $\text{InP}/\text{In}_{0.53}\text{Ga}_{0.47}\text{As}$  and  $\text{GaAs}/\text{In}_x\text{Ga}_{1-x}\text{As}$  QWIPs yield gains significantly higher than that achievable with  $\text{Al}_x\text{Ga}_{1-x}\text{As}/\text{GaAs}$  QWIPs with  $x \sim 0.3$  [1,94,99,100,101]. These observations were attributed to high quality binary InP and GaAs barriers and to the higher mobility of InP and GaAs when compared with AlGaAs [1,94,100,101]. However,  $\text{InP}/\text{In}_{0.53}\text{Ga}_{0.47}\text{As}$  QWIPs yield relatively low gain under low bias [94,99] contrary to the above suggestion.

Figure 5.10 shows the calculated drift distance versus the average E-field in the device, and Figure 5.11 presents the local capture probability versus the E-field in the barrier preceding the well for the simulated QWIPs. The characteristics obtained with %50 reduced effective masses in the conduction band valleys, and with increased  $\Gamma$ -L energy spacing (equal to those in InP) are also included in Figures 5.10 and 5.11. The drift distance is extracted from the device gain obtained by dividing the number of electrons injected into the device by the total number of the excited electrons that escape from QWs, which is equal to the total number of captured electrons at steady-state [24]. The local capture probability was calculated by dividing the portion of the current captured by a well to the total current incident to the well. It is generally believed that the capture probability monotonically decreases with increasing E-field. However, based on our results, depending on the material properties,  $p_c$  may increase with increasing E-field under moderately large E-field. This behavior is due to the creation of a strong capture path through the L valley QW as the heated  $\Gamma$  valley continuum electrons scatter to the L valley. Under large E-fields,  $p_c$  decreases with increasing field due to the heating of the electrons in the satellite valleys.

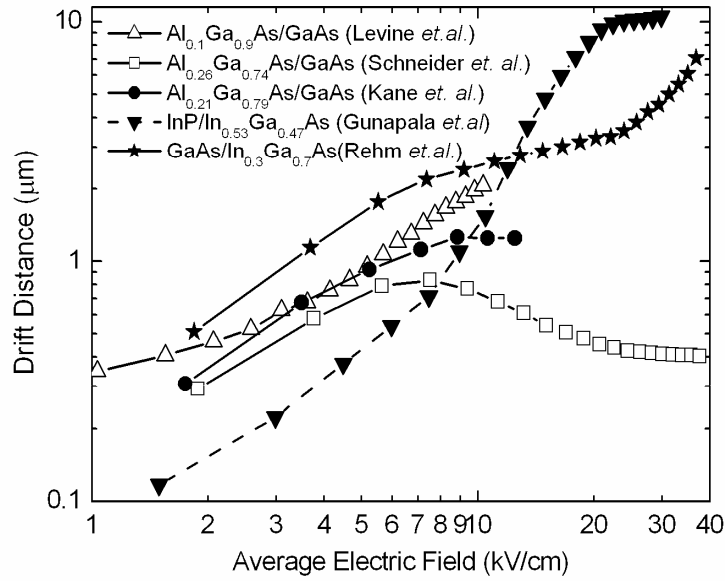


Figure 5.9 Drift distances versus average electric field in device extracted from measured gains reported by different groups for various QWIPs [32,39,95,101,103].

As shown in Figure 5.10, while negative differential change is observed in the drift distance versus E-field characteristic of  $\text{Al}_{0.3}\text{Ga}_{0.7}\text{As}/\text{GaAs}$  QWIP, that of  $\text{Al}_{0.15}\text{Ga}_{0.85}\text{As}/\text{GaAs}$  QWIP does not display saturation or negative differential change in qualitative agreement with the experimental results reported for  $\text{AlGaAs}/\text{GaAs}$  QWIPs with low Al mole fraction [32]. Under moderate and large bias, the average electron velocity in  $\text{Al}_{0.15}\text{Ga}_{0.85}\text{As}/\text{GaAs}$  QWIP is only slightly larger than that of  $\text{Al}_{0.3}\text{Ga}_{0.7}\text{As}/\text{GaAs}$  QWIP, however the gain of former is considerably larger than that of latter due to higher excited electron lifetime in  $\text{Al}_{0.15}\text{Ga}_{0.85}\text{As}/\text{GaAs}$  QWIP. Smaller capture probability in  $\text{Al}_{0.15}\text{Ga}_{0.85}\text{As}/\text{GaAs}$  QWIP is due to shallower L valley QW, as well as to the larger  $\Gamma$ -L energy spacing. In case of increased  $\Gamma$ -L spacing (equal to those in InP), moderate and large bias gains significantly exceed that of  $\text{Al}_{0.3}\text{Ga}_{0.7}\text{As}/\text{GaAs}$  QWIP in agreement with the experimental results.

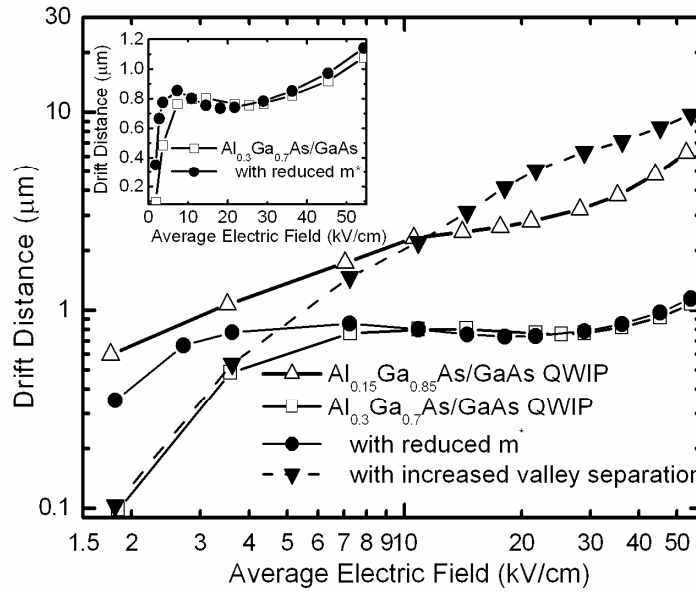


Figure 5.10 Calculated drift distance versus average electric field in device for the simulated QWIPs [95].

Figure 5.12 shows the effects of barrier material properties on the average electron velocity in the device and on the electron lifetime. Electron lifetime is calculated by dividing the average drift distance of the excited electrons by the average velocity of these electrons. The experimental results on the bias dependence of the excited electron lifetime in QWIPs are quite scattered [99,100]. As seen in Figure 5.12(b), bias dependence of the electron lifetime may vary depending on the material properties and the bias range. Lower electron lifetime in the case of reduced electron effective mass (in spite of larger drift distance) is due to considerably higher electron velocity in this case. While, reducing the electron effective masses in the barrier results in a considerable increase in the average electron velocity and in the low bias drift distance, almost no change is observed in the moderate and large bias drift distance as shown in Figure 5.10 .

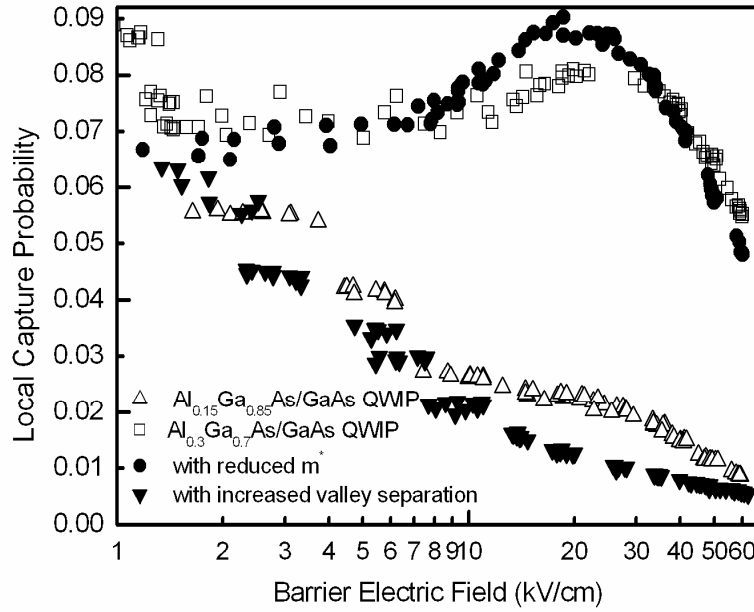


Figure 5.11 Calculated local capture probability versus the electric field in the barrier preceding the capturing quantum well [95].

The increase in the low bias drift distance with reduced electron effective mass results from considerably higher kinetic energy of the  $\Gamma$  valley electrons resulting in lower capture probability in this valley. As the bias is increased, the difference between the drift distances is decreased due to higher rate of increase of the L valley occupancy (and higher rate of increase of  $p_c$ ) in the reduced electron effective mass case (Fig. 5.11). Under moderately large bias, the drift distance (and gain) is decreased with increasing bias in both cases, due to the transfer of the electrons to L valley decreasing the electron lifetime. As can be seen from Figures 5.10 and 5.12, the negative differential change in the gain can not be explained only by the degradation of the electron velocity as a result of intervalley transfer. The drift distance starts to decrease with increasing bias well before the average electron velocity in the device peaks. The negative differential change observed in the gain-bias characteristic of  $\text{Al}_{0.3}\text{Ga}_{0.7}\text{As}/\text{GaAs}$  QWIP is mainly due to the rapid decrease in the excited electron lifetime as the electron transfer to L valley starts and the

capture path through the L valley QW becomes effective. It should also be noted that the drift distance starts to increase with increasing E-field under large bias due to the heating of the satellite valley electrons resulting in lower capture probability. Increase in the QWIP gain with increasing bias was experimentally observed by various groups [102-104], and this was attributed to impact ionization. Based on our results, this may, at least partially, be attributed to the increase in the electron lifetime due to the heating of the satellite valley electrons.

Increased energy difference between the central and satellite valleys (equal to those in InP) results in an improvement in the high bias average electron velocity by a factor of  $\sim 1.5$ , while the excited electron lifetime increases by a factor of  $\sim 6$  resulting in an improvement in the large bias gain by a factor of  $\sim 10$  (Fig. 5.10, 5.12). These results show that the gain improves with increasing energy difference between the central and satellite valleys mainly through the increase in the excited electron lifetime as a result of higher  $\Gamma$  valley occupancy of the continuum electrons with relatively high kinetic energy. The low bias gains obtained with different energy spacings between the central and satellite valleys are almost identical due to the same electron effective masses and QW properties employed in the simulation. Experimental results on InP/InGaAs QWIPs yield low bias gains smaller than those in AlGaAs/GaAs QWIPs due to higher electron effective mass in the  $\Gamma$  valley of InP. However, under large bias, InP/InGaAs QWIPs yield much higher gain due to much larger energy spacing between the central and satellite valleys. Therefore, both large energy separation between the central and satellite valleys and small barrier electron effective mass are necessary to achieve high gain throughout the typical QWIP bias range unless the QWs in the satellite valleys are very shallow. GaAs/In<sub>x</sub>Ga<sub>1-x</sub>As QWIPs and Al<sub>x</sub>Ga<sub>1-x</sub>As/GaAs QWIPs with low  $x$  satisfy the above condition.

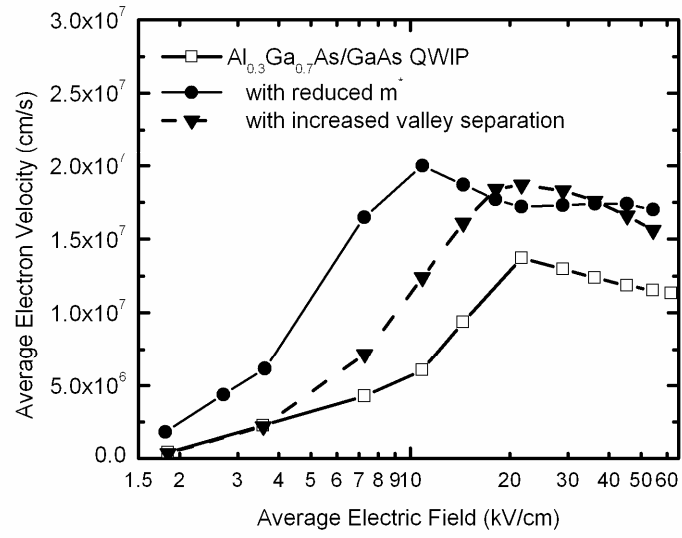
Figure 5.13 shows the spatial distribution of the captured electrons that are excited from various wells in the Al<sub>0.3</sub>Ga<sub>0.7</sub>As/GaAs QWIP under 1.33 V bias which provides nonuniform E-field decreasing toward the collector as shown in Figure



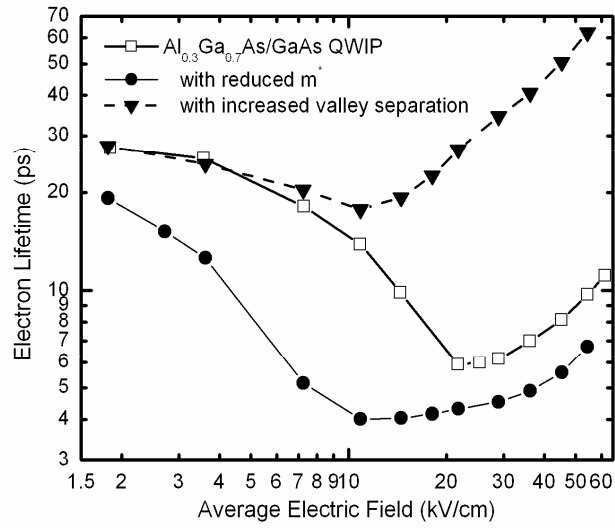
5.2. It is generally assumed that the excited electrons experience the same capture probability in the following wells. As seen in Figure 5.13, depending on the local E-field, electrons excited from a well are captured by the following wells with unequal probability. In the region under moderately high E-field, the first well following the well of excitation captures the least number of electrons, while the 3<sup>rd</sup> well captures the maximum number of electrons. This is due to the heating of the newly excited electrons and their scattering to L valley resulting in an increase in their capture probability as they travel through a distance of approximately three periods from the well of excitation. Under the given E-field strength, newly excited electrons become indistinguishable after traveling through this distance beyond which they exhibit capture characteristics similar to that usually assumed. Under 3.33 V bias, the above distance is reduced to two periods from the well of excitation. It should also be noted that the electrons excited from the wells near the collector (low E-field region) are most likely to be captured by the same well, and they can even be captured by the preceding wells due to the reflections from the heterointerfaces.

## **5.6 Monte-Carlo Simulation of Transient Characteristics of QWIPs**

There have been numerous reports on the transient photocurrent response of QWIPs subjected to short pulses of infrared radiation [77-79,104,106-110]. The QWIP transient photoresponse involves different time constants. The fast part of the transient is completed in picosecond time scale, and the time constant associated with this part is related with the capture and transit times of the photoexcited electrons.



(a)



(b)

Figure 5.12 Average electron velocity (a) and electron lifetime (b) versus the average electric field in device. The figure shows the effects of barrier electron effective mass and energy spacing between the central and satellite valleys on the average electron velocity and electron lifetime in the device [95].

During the slow part of the transient, the E-field at the emitter contact adjusts itself to inject the corresponding photocurrent by recharging of the QWs, and this part of the transient lasts longer. Experimental observation of the details of fast transient response is difficult due to the limited bandwidth of the measurement set up. However, a detailed understanding of QWIP transient photoresponse is essential for employing this high-speed device for high-frequency applications.

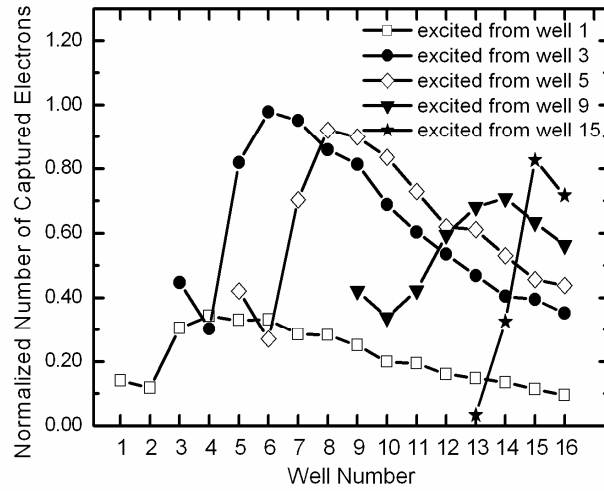


Figure 5.13 Spatial distribution of the captured electrons that are excited from various wells in the  $\text{Al}_{0.3}\text{Ga}_{0.7}\text{As}/\text{GaAs}$  QWIP under 1.33 V.

There have been reports on the investigation of QWIP transient response using continuity equation, Poisson's equation and the rate equations, as well as analytical formulations [107–108,110]. However, even the use of E-field dependent transport and capture parameters does not accurately reveal the non-stationary transport and capture characteristics of the electrons in the device; since these parameters are not instantaneous functions of the E-field. Although being computationally expensive, EMC simulation is a better alternative to the above models for investigating the fast part of the transient. Ryzhii *et. al.* [77–79] investigated the response of QWIP to short pulses of infrared radiation through EMC simulations using a phenomenological capture parameter. They reported photocurrent overshoot

characterized with a time constant depending on intervalley scattering rates of newly photoexcited electrons. In this work, we resolve the details of the fast part of the QWIP transient response under short pulse of infrared radiation using the above described EMC simulations. After steady state is reached, the QWIP is excited by increasing the photoexcitation rate to  $10^{13} \text{ s}^{-1}$  ( $t = 0$ ) for a duration of 250 fs. During the simulation, we sample the current through the collector terminal, which is a directly measurable quantity. Note that the following analysis applies to standard LWIR  $\text{Al}_{0.3}\text{Ga}_{0.7}\text{As}/\text{GaAs}$  QWIP with 16 QWs. The speed of QWIPs with a large number of QWs will be limited with the electron lifetime, which is several picoseconds under moderately large bias for LWIR  $\text{Al}_{0.3}\text{Ga}_{0.7}\text{As}/\text{GaAs}$  QWIP (Fig. 5.12(b)). While special structures with high  $p_c$  can be designed to expand the bandwidth, such structures offer significantly lower responsivity [97]. On the other hand, QWIP response time may be shortened by using a small number of QWs (transit time limited device); however, in this case, the quantum efficiency of the device is degraded.

Figure 5.14 shows the photocurrent of the above described  $\text{Al}_{0.3}\text{Ga}_{0.7}\text{As}/\text{GaAs}$  QWIP under 2V bias, which provides large enough E-field throughout the QWIP to saturate the electron velocity at steady state (see Fig. 5.2). Figure 5.14 also shows the photocurrent transient obtained when the capture to L and  $\Gamma$  valley QWs are turned off. The photocurrent rise time is less than 1 ps, and the transient lasts approximately 10 ps. As shown in Figure 5.14, the photocurrent transient can be divided into three regions. The photocurrent overshoot observed just after the photoexcitation can be attributed to the large E-field gradient faced by the newly photoexcited electrons and subsequent scattering of these electrons to higher-energy conduction band valleys. Photoexcited electrons that can reach the collector contact before intervalley scattering creates the peak in the photocurrent. Considerable photocurrent overshoot is observed only under large bias voltages due to the relatively small electric field near the collector under low bias. Under small bias voltages, electrons excited near the collector are swept out with relatively small velocities, and a small current is observed initially. Later, hot electrons excited in

the high field region reach the low field region near the collector, cool gradually to lower velocities, become accumulated in the low-field domain, and generate monotonously increasing current at the collector. The photoexcitation alters the E-field distribution in the device insignificantly in the time scale of interest. Therefore, the photocurrent overshoot in our case is not due to responsivity nonlinearity effects observed by Letov et al. [105]. The overshoot is followed by a decay due to the capture and dispersion of the excited electrons. The last region is the turn-off stage where a relatively sharp photocurrent decrease is observed as the electrons photoexcited at the emitter side are extracted from the device through the collector contact. Note that turn-off does not occur sharply due to the dispersion of the electrons, and the duration of the turn-off region is considerably long. When the capture is completely turned off, the photocurrent pulse width is increased by  $\sim 15\%$  suggesting that the photoresponse time is mostly determined by the transit time in QWIPs with comparable  $p_c$  and device length.

The bias dependences of the photocurrent pulse width, average transit time and average electron lifetime are shown in Figure 5.15. The average transit time is estimated by dividing the device length to the average steady-state electron velocity in the barriers. Under small bias voltages, pulse width rapidly decreases with increasing bias due to the increase in the average electron velocity. Beyond the bias voltage, under which electron velocity in the entire device is saturated (average E-field  $\sim 20$  kV/cm), the pulse width nearly saturates at  $\sim 10$  ps under large bias being  $\sim 40\%$  larger than the average transit time estimated as described above. In the large bias region, slight increase in the pulse width with increasing bias is due to the combined effects of increasing transit time (decreasing electron saturation velocity) and increasing lifetime. The inset of Figure 5.15 shows the pulse widths of the local photocurrents at various barriers under 2.67 V bias, which provides nearly uniform E-field in the device. The results show that the pulse width increases linearly with increasing device length suggesting transit time limited photoresponse time.

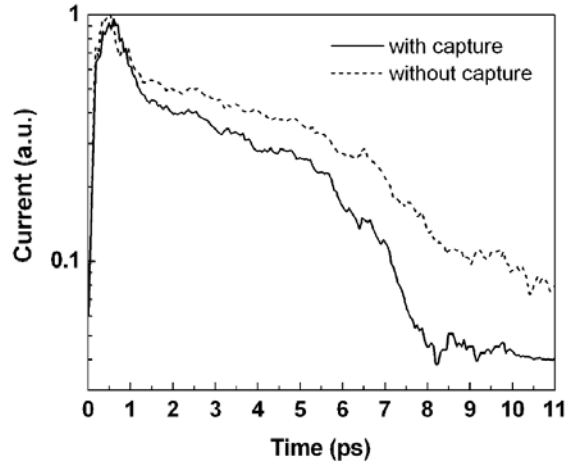


Figure 5.14: Transient photocurrent of Al<sub>0.3</sub>Ga<sub>0.7</sub>As/GaAs QWIP subject to short pulse of IR radiation at 2V [95].

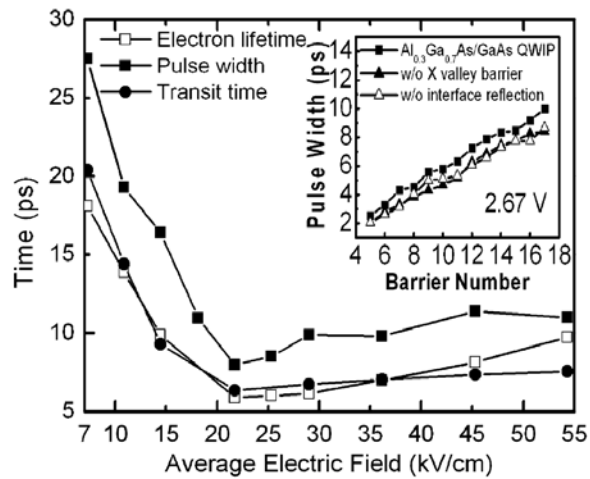


Figure 5.15 Average electron lifetime, pulse width, and electron transit time in Al<sub>0.3</sub>Ga<sub>0.7</sub>As/GaAs QWIP subjected to short pulse of IR radiation under various bias voltages [95].

The inset of Figure 5.15 also shows the photocurrent pulse widths obtained when the X-valley barriers are removed, and electron reflections from heterointerfaces (except the X-valley barriers) are ignored. Under both conditions, the

photoresponse time is decreased by  $\sim 15\%$ , showing that the reflections from heterointerfaces are of considerable importance even under large bias.

## 5.7 Conclusions

The main objective of this work is the investigation of electron transport and capture in QWIPs through detailed ensemble Monte Carlo simulations. Well accumulation is observed to occur non-uniformly, being highest near the emitter under large bias. The barrier electron velocity in  $\text{Al}_{0.3}\text{Ga}_{0.7}\text{As}/\text{GaAs}$  QWIPs is found to be close to the electron saturation velocity in bulk  $\text{Al}_{0.3}\text{Ga}_{0.7}\text{As}$  under large barrier E-field. Under low E-fields, it increases almost linearly with the E-field displaying mobility significantly smaller than the bulk mobility in the barrier material. The L valley is found to play a significant role in electron capture into QWs, and it should be considered in  $\text{Al}_x\text{Ga}_{1-x}\text{As}/\text{GaAs}$  QWIP optimization studies. For barrier Al mole fractions used in those QWIPs in the  $8\text{--}10\ \mu\text{m}$  spectral band ( $x\sim 0.3$ ), the majority of the captured electrons originate from the L valley under typical QWIP bias voltages. It is generally believed that intervalley transfer affects the gain through the decrease in the electron drift velocity. However, according to the results of this study, the effect of the intervalley transfer on the gain is two fold: the decrease in the electron velocity, and the decrease in the excited electron lifetime due to the increase in the capture probability by the creation of an effective capture path. The above observation explains the experimentally observed large difference between the gains of QWIPs fabricated with different material systems, as well as the bias dependence of the gain. To the best of our knowledge, the simulator used in this work is the most detailed QWIP simulator reported to date, and the results of this work complement the previous related work to achieve a deeper understanding of QWIP operation and characteristics.

Above summarized results show that increasing the energy separation between the conduction band valleys results in a remarkable increase in the large bias gain

mainly through the increase in the excited electron lifetime. Based on the above results, experimentally observed large gain in QWIPs based on alternative material systems such as  $\text{InP}/\text{In}_{0.53}\text{Ga}_{0.47}\text{As}$  can mainly be attributed to larger excited electron lifetime instead of higher electron mobility in the binary barrier material.

Fast part of the transient photoresponse is also simulated. The simulation resolves the details of photocurrent decay under short pulses of infrared radiation. The fast part of the  $\text{Al}_{0.3}\text{Ga}_{0.7}\text{As}/\text{GaAs}$  QWIP transient response exhibits three regions with different decay characteristics under a short pulse of infrared radiation. Due to the dispersion of the photoelectrons, the duration of the final region (turn-off stage) has been observed to be considerable when compared with the total duration of the fast transient. The transit time limited photoresponse time rapidly decreases with increasing bias under low bias, and nearly saturates at  $\sim 10$  ps under large bias being  $\sim 40\%$  larger than the average transit time estimated by dividing the device length to the steady-state average electron velocity in the device. The effect of the hetero-interface reflections on the photoresponse time is also simulated. Showing that interface reflections are of considerable importance even under large bias.

As a final remark, the model implemented in this thesis models electron capture into QWs as the transitions of 3D electrons to a single 2D bound state in QW through optical phonon scattering, and successive relaxation of electron energy to a value below the barrier height. While this approach successfully explains the experimental observations on the relative magnitude and the bias dependence of gain in QWIPs fabricated with different material systems, incorporation of electron capture into the simulator in a more detailed manner by including the other scattering mechanisms and other possible transitions would certainly be invaluable to verify of the above findings. However, even with the current formulation of the capture mechanism, the simulation algorithm is significantly complicated and computationally expensive.



## CHAPTER 6

### INP BASED LWIR QWIP TECHNOLOGY

The AlGaAs/GaAs material system has been used as a standard in LWIR QWIP technology due to the mature GaAs processing technology. Its competing technology, InP also offers similar level of maturity and allows different transport properties than GaAs based materials.

In recent years interest in InP based QWIPs is increasing primarily due to rich material system choices which can be grown on InP. However, many of these materials' performance for QWIPs have not been explored fully yet. While only AlGaAs/GaAs and GaInP/GaAs heterostructures can be grown lattice matched on GaAs, ten different heterostructures lattice matched to InP substrate are listed in Table 6.1 [111].

#### 6.1 Previous work on InP based QWIPs

The characteristics of metal–organic molecular beam epitaxy (MOMBE) grown LWIR InP–InGaAs QWIPs were first discussed by Gunapala *et al.* [39] with a conclusion that the responsivity of these QWIPs is much larger than that of AlGaAs–GaAs QWIPs at high bias. A similar observation was reported by

Andersson *et al.* [112] on metal–organic vapor phase epitaxy (MOVPE) grown InP–InGaAs QWIPs. Large gain and responsivity in InP–InGaAs QWIPs were also reported by other groups [84, 113-116], and the first InP–InGaAs QWIP focal plane array (FPA) was reported recently by Jiang *et al.* [117] with a format of 256x256 using metal–organic chemical vapor deposition grown material. InP–InGaAs QWIP responsivity generally increases monotonically with increasing bias. However, in order to utilize this property of the InP/InGaAs QWIP, a reasonably high detectivity must be achieved under bias voltages yielding high responsivity. At the same time, acceptably low nonuniformity over a sufficiently large area is required for obtaining a reasonably low noise equivalent temperature difference (NETD) in InP–InGaAs QWIP FPAs.

Table 6.1 Material systems that can be grown lattice matched to InP substrate. [111]

Material System	E <sub>g</sub> (eV)	ΔE <sub>c</sub> (eV)	ΔE <sub>v</sub> (eV)
AlAsSb/GaInAs	2.45/0.75	1.75	-0.07
Al <sub>x</sub> Ga <sub>1-x</sub> As <sub>y</sub> Sb <sub>1-y</sub> /GaInAs	2.45/0.75	1.75 to -0.3	-0.07 to -0.4
AlInAs/GaInAs	1.45/0.75	0.5	0.19
(Al <sub>x</sub> Ga <sub>1-x</sub> ) <sub>y</sub> InAs <sub>1-y</sub> /GaInAs	1.45-0.9/0.75	0.5 to 0.13	0.19 to 0.063
AlInAsSb/GaInAs	1.8/0.75	0.7	-0.25
InP/InGaAs	1.35/0.75	0.25	0.35
InP/GaAsSb	1.35/0.72	-0.1	0.6
AlInAs/GaAsSb	1.45/0.72	-0.07	0.65
AlAsSb/GaAsSb	2.45/0.72	1.1	0.50
Ga <sub>x</sub> In <sub>1-x</sub> As <sub>y</sub> P <sub>1-y</sub> /GaInAs	1.35 to 0.9/0.75	0.22	0.35

An important disadvantage of InP–InGaAs for QWIP applications is the lack of flexibility in adjusting the peak detection wavelength by changing the barrier/well

material composition, limiting the peak responsivity wavelength to a narrow range around 8  $\mu\text{m}$ . However, it has been shown by Gusakov *et al.* [118] that it is possible to extend the operating wavelength up to 11  $\mu\text{m}$  by utilizing the strain as an additional bandgap engineering parameter. It is also possible to increase the peak responsivity wavelength above 8  $\mu\text{m}$  by using InGaAsP instead of InGaAs as the quantum-well (QW) material [119].

In the MWIR band, it is possible to obtain 3-5  $\mu\text{m}$  spectral response with AlGaAs/GaAs material system. However one has to use high Al mole fraction AlGaAs which has indirect bandgap above 350 meV conduction band discontinuity [120,121]. Figure 6.1 shows the variation of  $\text{Al}_x\text{Ga}_{1-x}\text{As}$  conduction band minima with Al mole fraction .

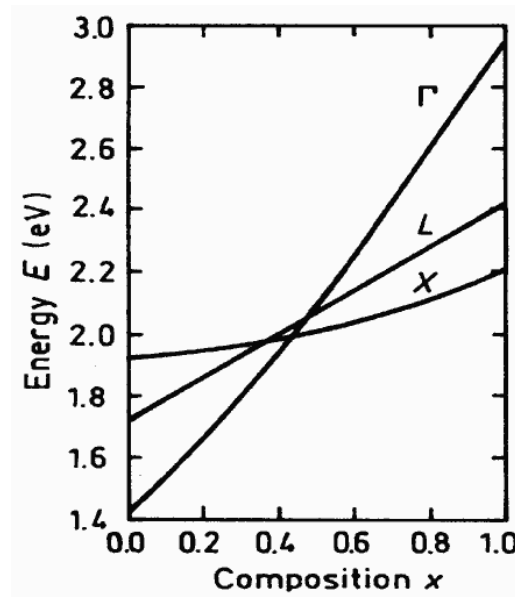


Figure 6.1 Variation of  $\text{Al}_x\text{Ga}_{1-x}\text{As}$  conduction band minima with Al mole fraction. [122]

AlAs like narrow barriers are reported to increase the separation between the QW states, however this method reduces the escape probability of the excited electrons

and results in low photoexcitation into continuum [123]. As an alternative to these methods, strained InGaAs quantum wells between AlGaAs barriers are used in order to have large conduction band discontinuity in n-type QWIPs.[124]. However, difficulty of growing strained layers with high quality is an important problem in production of these devices.

Performance of MWIR InP based QWIPs is not studied in detail in the literature [111,120,125].  $\text{Al}_{0.48}\text{In}_{0.52}\text{As} / \text{In}_{0.53}\text{Ga}_{0.47}\text{As}$  heterostructure is lattice matched to InP and offers approximately 500 meV conduction band discontinuity which is suitable for MWIR QWIP design. Maximum QWIP responsivity reported with this material is 300 mA/W [111], and highest reported specific detectivity is  $1.5 \times 10^{12} \text{ cmHz}^{1/2}/\text{W}$  ( $180^\circ$  FOV, 77K, BLIP) [120]. 256x256 format FPA is fabricated with this material system by BAE systems and reached 32 mK NETD value [111]. AlInAs/InGaAs MWIR QWIP is also interesting due to the possibility to monolithically growth with InP/InGaAsP LWIR QWIP in order to have dual band QWIP.

## 6.2 InP based QWIP Structures

In order to investigate the feasibility of InP based LWIR QWIPs, InP/InGaAs and InP/InGaAsP LWIR QWIP structures are fabricated and characterized in this study. Standard AlGaAs/GaAs QWIPs were also fabricated for relative performance assessment.

The investigated InP/InGaAs, InP/InGaAsP, and AlGaAs/GaAs epilayer structures are shown in Figure 6.2(a)-(c). The InP/InGaAs QWIP epilayer structure consists of twenty  $\text{In}_{0.53}\text{Ga}_{0.47}\text{As}$  (60 Å thick) quantum wells (QWs) sandwiched between 500 Å thick InP barriers, in addition to n-type top and bottom  $\text{In}_{0.53}\text{Ga}_{0.47}\text{As}$  contact layers doped to  $1 \times 10^{18} \text{ cm}^{-3}$ . Central 50 Å thick regions of the QWs are n-type doped at  $5 \times 10^{17} \text{ cm}^{-3}$ . InP/InGaAsP QWIP has the same structure except that the

number of QWs is thirty and the QWs are 56 Å thick  $(\text{In}_{0.532}\text{Ga}_{0.468}\text{As})_{(1-z)}(\text{InP})_z$  (1.55 μm bandgap) material, and QWs are volume n-doped at  $5 \times 10^{17} \text{ cm}^{-3}$ . AlGaAs/GaAs QWIP grown for comparison consists of thirty periods with 40 Å thick GaAs QWs and 500 Å  $\text{Al}_{0.273}\text{Ga}_{0.727}\text{As}$  barriers. QWs are 20 Å center doped at  $8 \times 10^{17} \text{ cm}^{-3}$ .

### InP/ $\text{In}_{0.53}\text{Ga}_{0.47}\text{As}$ QWIP

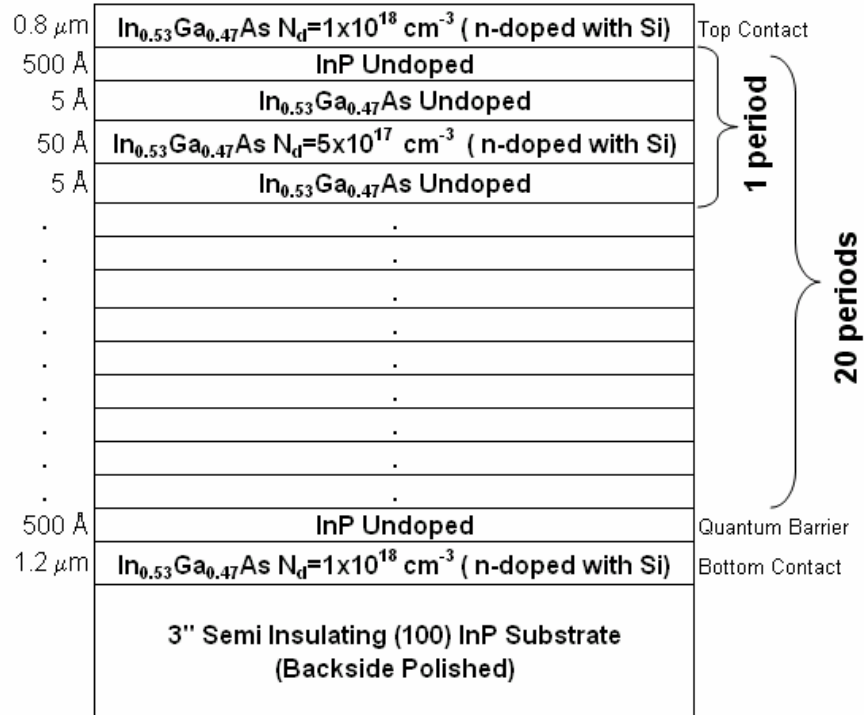


Figure 6.2 (a) InP/InGaAs QWIP structure investigated in this study.

## InP/InGaAsP QWIP

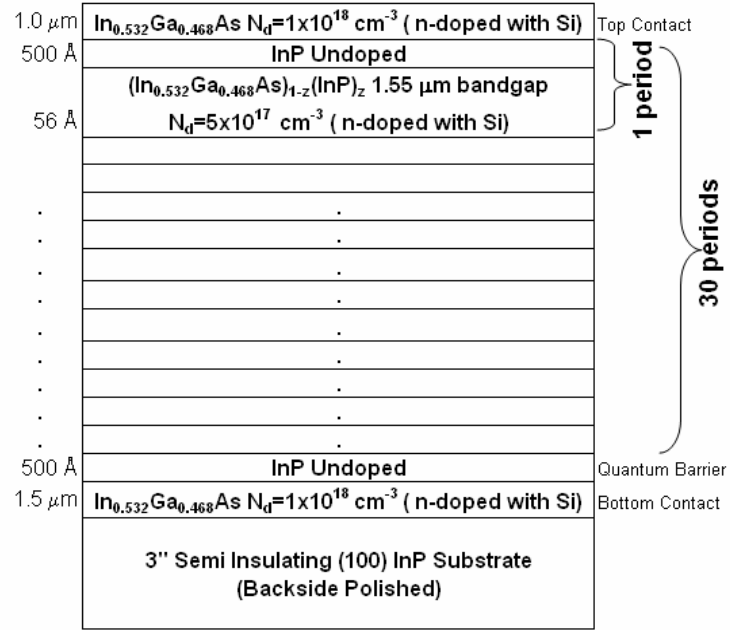


Figure 6.2 (b) InP/InGaAsP QWIP structure investigated in this study.

## $\text{Al}_{0.275}\text{Ga}_{0.725}\text{As}/\text{GaAs}$

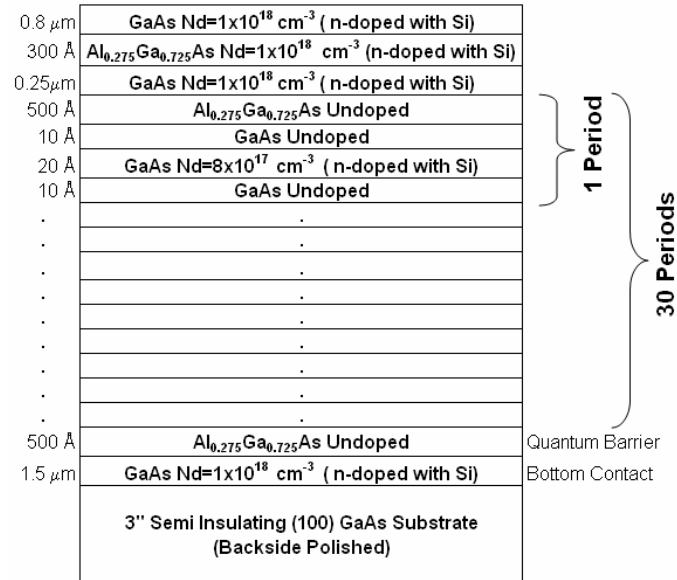


Figure 6.2 (c) AlGaAs/GaAs QWIP structure investigated in this study.

Figure 6.3 shows energy band diagrams of the single quantum wells of the investigated QWIP structures. The material parameters are given in appendix A. AlGaAs/GaAs QWIP structure has quantum wells in both  $\Gamma$  and L valleys with a barrier in X valley. On the other hand InP/InGaAs and InP/InGaAsP QWIP structures have quantum wells in all three valleys. The most important difference in the energy bands is that,  $\Gamma$ -L and  $\Gamma$ -X valley separations in AlGaAs/GaAs QWIP are significantly less than those in the given InP based QWIPs. This large valley separation makes InP QWIPs low capture probability devices as discussed in detail in this thesis.

### 6.3 QWIP Device Fabrication

For the FPA fabrication,  $21\ \mu\text{m} \times 21\ \mu\text{m}$  mesa (with  $25\ \mu\text{m}$  pitch) and lamellar optical grating were defined by standard photolithography and dry etching. Following ohmic contact and reflector formation, passivation, and under-bump metallization, indium bumps were uniformly formed through electro-plating. The FPA was flip-chip bonded to a commercial read-out integrated circuit (ROIC) with a charge capacity of 11 million electrons and noise level of 500 electrons.

After filling the gap between the FPA and the ROIC with an underfill epoxy, the substrate of the FPA was thinned with a high resolution lapping/polishing system, and the FPA/ROIC hybrid was mounted on a 84-pin LCC package for testing. InP/InGaAs test QWIPs with the same size and structure (including optical grating) with the FPA pixels were fabricated with the FPA. The test detectors with indium bumps were coupled to fan-out substrates by flip-chip bonding. Due to the very high electrical resistance of the small size detectors, test detectors were  $5 \times 5$  parallel connected in order to facilitate reliable electrical and optical measurements. After under filling, the substrate of the test detectors was thinned, and the hybrid was mounted on an LCC package for testing in a closed-cycle helium cryostat (Fig. 6.4).

The device fabrication technology development is done together with Dr. Selçuk Özer, and also reported in Ref. 135.

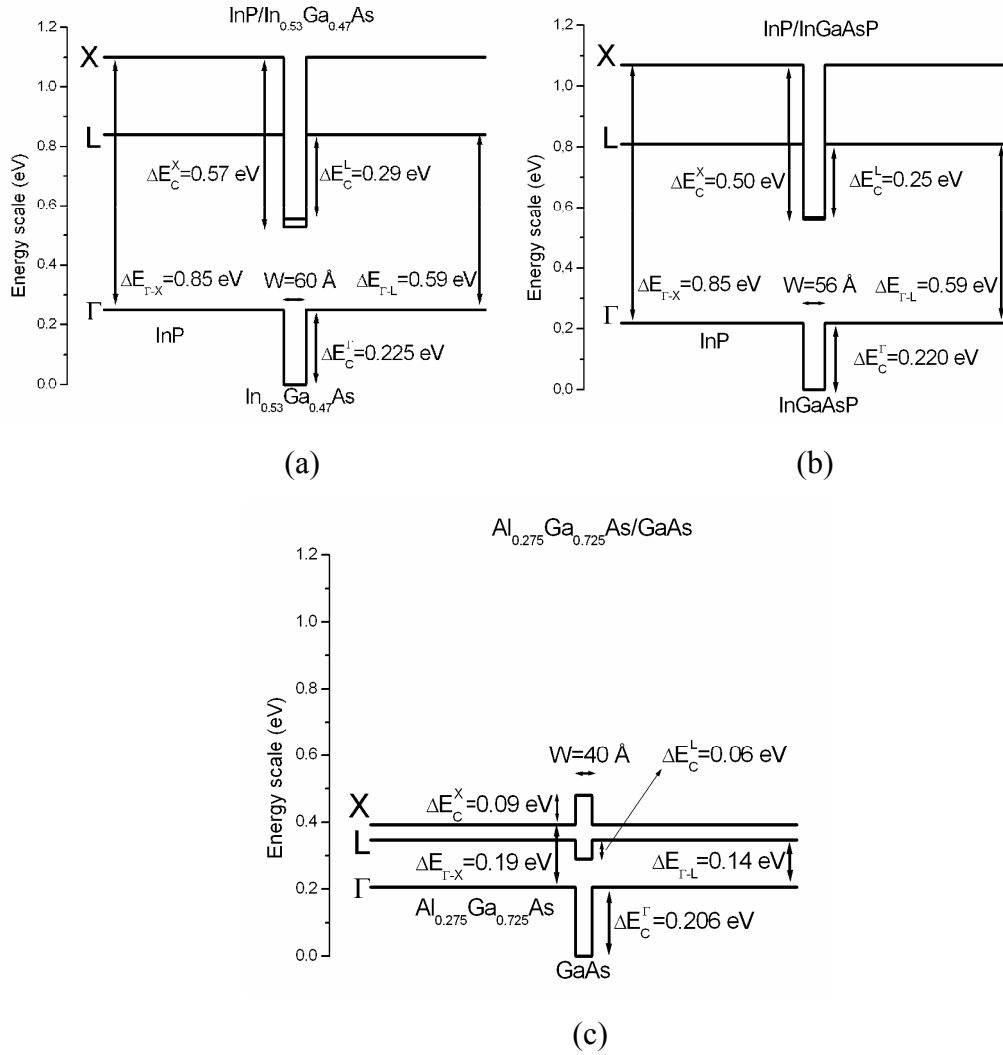


Figure 6.3 Energy band diagrams of single quantum wells of the investigated QWIP structures InP/InGaAs (a), InP/InGaAsP (b), and AlGaAs/GaAs (c) QWIPs.



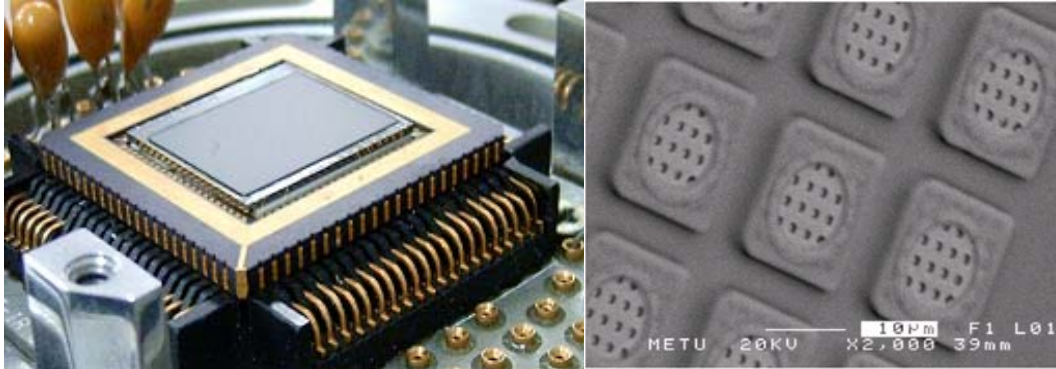


Figure 6.4 Fabricated 640x512 QWIP FPA and SEM picture of pixels with cross grating.

## 6.4 Characterization Set-up

80 K measurements are done in a liquid nitrogen cooled detector test dewar with 72 pin-outs. The field of view (FOV) in this test dewar is 180 degrees without any cold shield. For variable temperature testing the detectors are wire bonded to an LCC-84 pin test package and installed into He cryostat. This He cryostat can be configured for 180 degrees FOV, or  $f/2$  FOV with cold shield, or the detector FOV can be blocked for dark current measurements. In this setup, cold shield has the same temperature with the detector cold finger. Figure 6.5 shows detector cooling set-up. For quick 77 K dark current measurements, the detectors are wire bonded onto alumina substrates with gold pads and immersed into aluminum liquid nitrogen container with cooled cap. I-V characterization of the test detectors are done using Keithley 236 source measure unit under computer control with HP-VEE protocol. Figure 6.6 shows the IV characterization set-up.



Figure 6.5 Test dewar, He cryostat, and inside of the dewar with f/2 cold shield installed.



Figure 6.6 I-V Characterization set-up.

Optical response measurement set-up is illustrated in Figure 6.7. The detector is exposed to a laboratory blackbody source with a heated cavity and an adjustable aperture. The radiation emitted from the blackbody is chopped with a 1 Hz-to-1 kHz adjustable chopper at room temperature and the modulated radiation is collected by the detector. The photocurrent of the detector is buffered and

amplified with a transimpedance preamplifier (Stanford Research Systems SRS 570). The preamplifier is capable of applying low noise bias on the range of -5 V to +5 V. The gain and bandwidth of the preamplifier is adjustable and special care is given to keep the signal above the noise floor, and the gain flat in the measurement frequency range. The output signal from the preamplifier is fed into a digital lock-in amplifier (Stanford Research Systems SRS 830) which is locked to the reference TTL signal from the chopper controller. The digital lock-in amplifier is precise measurement equipment which extracts and measures a weak narrow-band signal at the modulating chopper frequency, from a wide noise floor in frequency domain thanks to its DSP processors. Once the signal is measured with the lock-in amplifier, the responsivity is calculated with the estimated power integrated by the photodetector. In order to calculate detectivity, the blackbody is blocked, the chopper is stopped, and the photodetector is left with the background signal. The noise signal is fed to the lock-in amplifier with exactly same set-up, and the lock-in amplifier measures standard deviation of the sampled signal. The measurement set-up is configured such that the dominant noise mechanism is the photodetector noise. If significant system noise is present, it is measured by disconnecting the detector, and the system noise power is extracted from the measured noise with the detector. Detectivity and noise equivalent power is calculated with this procedure.

Spectral response of the fabricated photodetectors are measured with ORIEL MIR-8000 FTIR system. The system set-up is illustrated in figure 6.8. This FTIR works with collimated light beam which is emitted from a metal filament blackbody. The collimated blackbody radiation is modulated with the Michelson interferometer housed in the FTIR box. The output light of the interferometer falls on the photodetector. The photodetector signal is preamplified with the transimpedance amplifier and fed back into the FTIR system. After the internal A/D converter at the input stage, the system calculates Fourier transform of the time-domain signal from the photodetector. This transform gives spectral response of the photodetector in photon wavelength domain. In order to cancel effects of the non-ideal blackbody radiation, and the absorbance effects in the FTIR system a reference measurement is

done with a pyroelectric detector. This detector has a flat response shape from 1  $\mu\text{m}$  up to 20  $\mu\text{m}$  wavelength and characterizes the background seen by the fabricated photodetector. The FTIR response of the photodetector is normalized with the calibration spectrum of the pyroelectric detector in order to see the real spectral response shape of the detector.

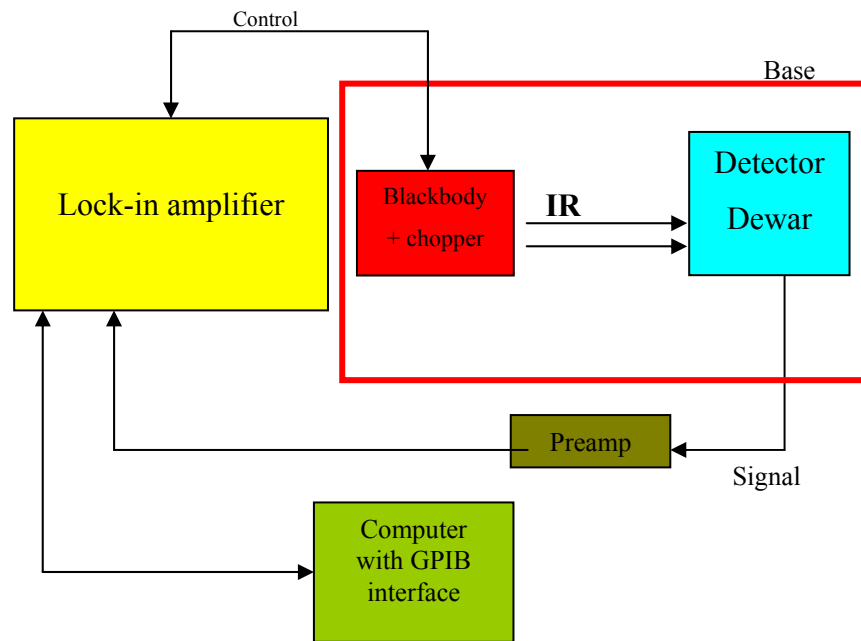


Figure 6.7 Optical response measurement set-up.

The test detectors in this study are flip-chip bonded test detectors which are fabricated on the same substrate with the FPA. They are 64 x 64 pixels arrays and

have the same geometry with the FPA pixels. These test detectors are flip chip bonded on oxide covered silicon substrate or on a semi-insulating GaAs substrate which are patterned with the fan-out metal paths. These paths connect 5x5 parallel connected pixels to wiring pads. Parallel connection of pixels is necessary in order to decrease the impedance of the detectors for testing purposes. The flip-chip bonded test detectors are lapped and backside illuminated. Figure 6.9 shows a flip-chip bonded test detector.

## 6.5 Characterization Results

Figure 6.10 shows the measured spectral response curves of InP/InGaAsP and InP/InGaAs QWIPs. InP/InGaAsP QWIP response peaks at 8.36  $\mu\text{m}$  wavelength with 7.74 and 8.91  $\mu\text{m}$  %50 cut-off wavelength, corresponding to %14  $\Delta\lambda/\lambda_p$ .  $\lambda_p$  of InP/InGaAs is at 7.85  $\mu\text{m}$  with a  $\Delta\lambda/\lambda_p$  of 11%, and  $\text{Al}_{0.273}\text{Ga}_{0.727}\text{As}/\text{GaAs}$  QWIP responsivity peaks at 7.74  $\mu\text{m}$  with a  $\Delta\lambda/\lambda_p$  of 15%.

Fig. 6.11 shows the dark current versus bias characteristics of the InP/InGaAs QWIP for various temperatures and that of AlGaAs/GaAs QWIP at 77 K detector temperature. Dark current comparison of InP/InGaAs and the AlGaAs/GaAs QWIP is meaningful since these detectors have similar peak responsivity wavelengths. 77 K photocurrent obtained with f/2 aperture under 300 K background is also displayed for the InP/InGaAs QWIP showing that the device is BLIP under low bias voltages at 77 K, while the background limited performance extends up to -3.2 V at 70 K detector temperature. Under low reverse bias, 77 K dark current of InP/InGaAs QWIP is considerably lower than that of AlGaAs/GaAs QWIP. However, the 77 K dark current of the InP/InGaAs QWIP exceeds that of AlGaAs/GaAs QWIP by nearly an order of magnitude under larger reverse bias voltages. This can be attributed to much faster rate of increase of the InP/InGaAs QWIP gain with increasing bias under moderately large bias voltages. While the InP/InGaAs QWIP dark current is smaller under positive bias, the spectral response

is considerably narrower and the responsivity is lower than those under negative bias in agreement with the observation by Gunapala *et. al.* [94].

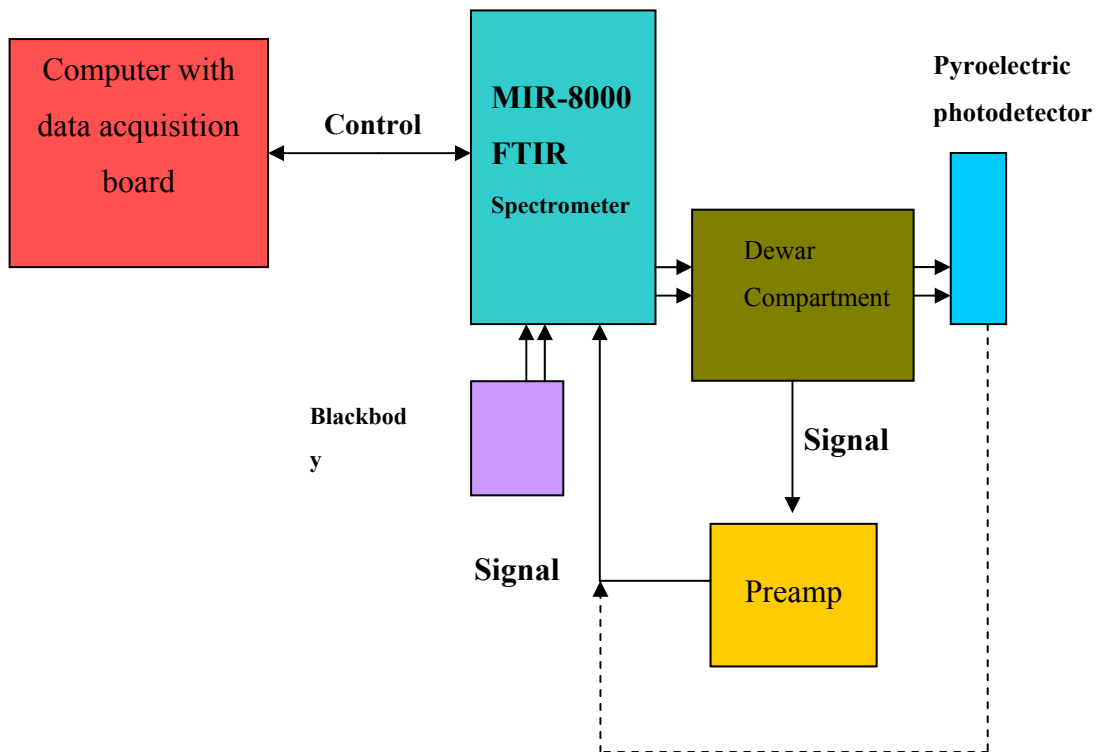


Figure 6.8 Spectral response measurement set-up with FTIR.

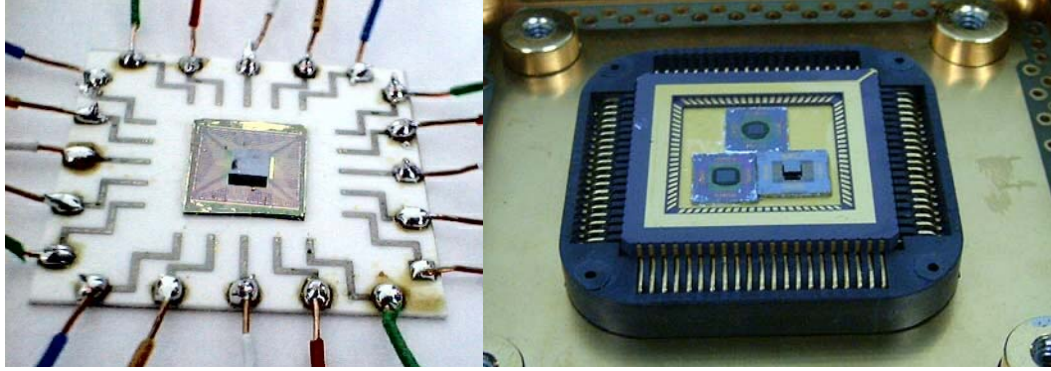


Figure 6.9 Flip-chip bonded test detector on a silicon fan-out substrate and then wire-bonded to alumina substrate or LCC-84 package.

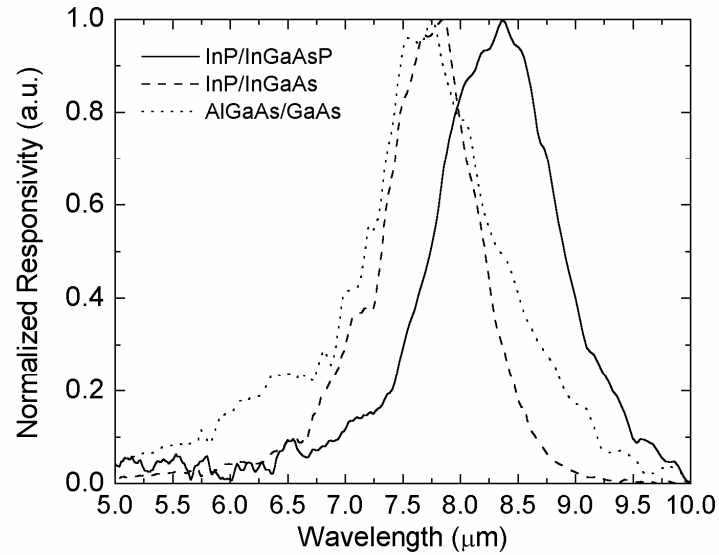


Figure 6.10 Spectral response of  $21 \times 21 \mu\text{m}^2$  InP/InGaAsP, InP/InGaAs and AlGaAs/GaAs QWIPs under  $-17 \text{ kV/cm}$  average electric field at 80 K.

Figure 6.12 shows dark current characteristics of InP/InGaAsP QWIP. Measured low bias BLIP temperatures of the InP/InGaAs QWIP is 77K, and that of InP/InGaAsP QWIP is 71 K. The InP/InGaAsP QWIP remains in BLIP region up to a reverse bias of 3V at 73 K. BLIP temperature of the longer wavelength InP/InGaAsP QWIP is less than the shorter wavelength InP/InGaAs QWIP which is

BLIP at 77K. This is expected since longer wavelength photodetectors have higher thermionic emission rate from the QWs due to lower activation energy.

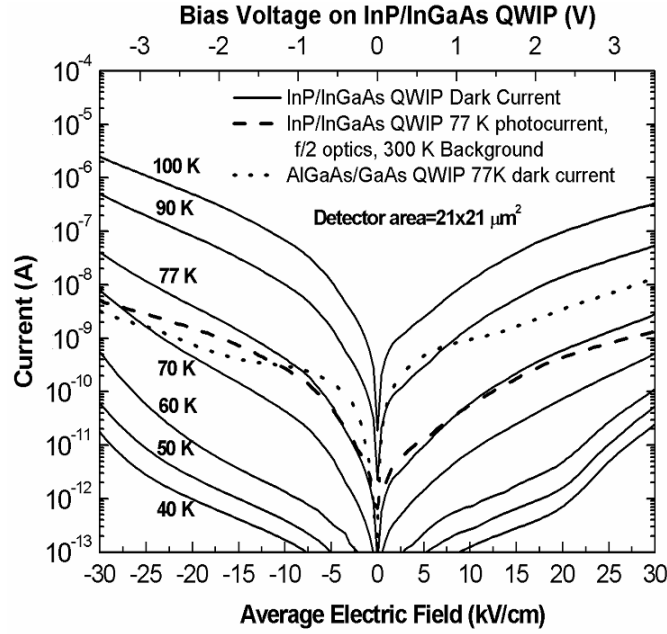


Figure 6.11 Bias dependence of the dark current of InGaAs/InP QWIP at various temperatures. 77 K photocurrent with f/2 optics and 300 K background is also shown [96].

The activation energy of the two devices can be deduced from the variation of dark current with detector temperature. Figure 6.13 shows the comparison of the activation energies for the InP/InGaAs and InP/InGaAsP in the 70K - 77K temperature range. Around -5 kV/cm average e-field, activation energy of InP/InGaAs QWIP is 152 meV which corresponds to 8.2  $\mu\text{m}$  cut-off wavelength photon energy. Activation energy of InP/InGaAsP QWIP is 130 meV which corresponds to 9.5  $\mu\text{m}$  cut-off wavelength photon energy. These values are consistent with measured spectral response of these QWIPs (Fig. 6.10). The ratio of the activation energies of these devices is 1.17. Assuming that dark current is mainly due to thermionic emission from the QWs the similar relation applies to BLIP temperatures. This corresponds to 12 K difference in device BLIP temperatures which is in acceptable agreement with  $\sim 7$  K measured difference.



The decrease of dark current activation energy with increasing electric field is related to electric field assisted tunneling of bound quantum well electrons through quantum barrier tip.

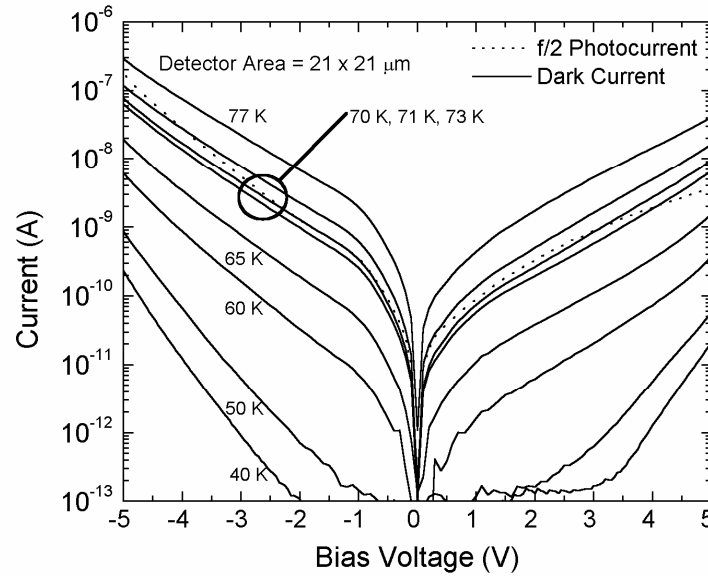


Figure 6.12 Bias dependence of the dark current density of InP/InGaAsP QWIP at various temperatures and 77 K photocurrent with f/2 optics and 300 K background.

Fig. 6.14 compares the 77 K dark current density of InP/InGaAs test QWIPs with various mesa perimeter/area ratios indicating that the dark current is independent of surface effects in the entire bias region of interest.

Fig. 6.15 compares the 77 K peak responsivities of InP/InGaAs, InP/InGaAsP, and AlGaAs/GaAs QWIPs. The highest responsivity obtained with the AlGaAs/GaAs QWIP is around 0.1 A/W under typical bias voltages. InP/InGaAs QWIP yields more than an order of magnitude higher responsivities reaching 2.9 A/W at -3 V bias corresponding to %46 external quantum efficiency.

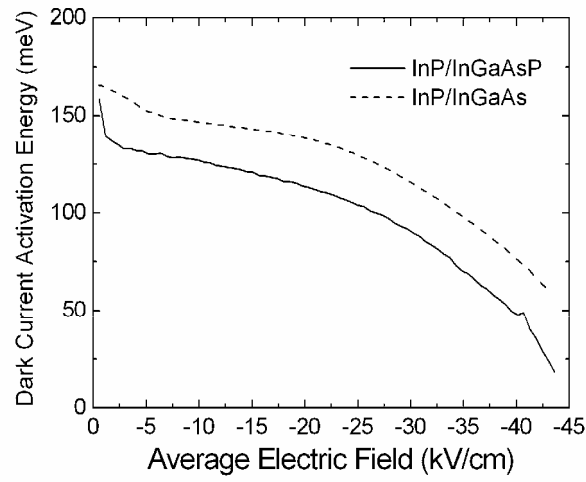


Figure 6.13 Dark current activation energy of InP/InGaAs and InP/InGaAsP QWIPs on 70K – 77K temperature range.

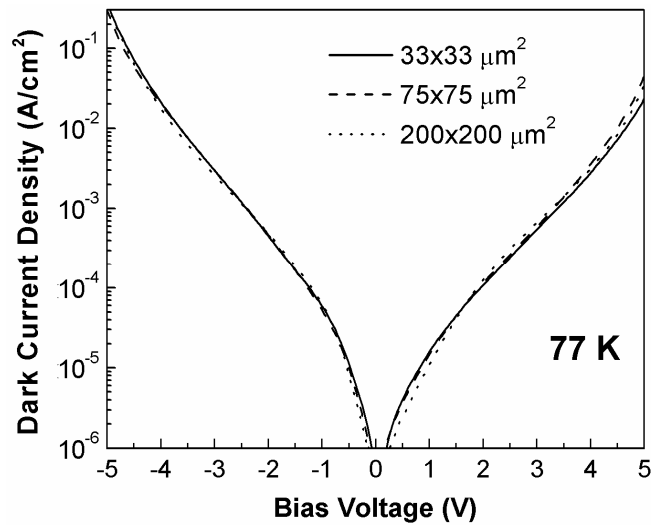


Figure 6.14 Dark current density of InP/InGaAs test QWIPs with various mesa sizes at 77 K.

While the higher responsivity in InP/InGaAs QWIP was attributed to better transport properties in the binary barrier material InP, as well as to impact ionization by other groups, Monte Carlo simulations presented in this study suggest that it mainly results from much higher electron lifetime in InP/InGaAs QWIPs

[96], at least under moderately large bias voltages. It should also be noted that the peak detectivity of InP/InGaAs QWIP is still higher than  $1 \times 10^{10} \text{ cmHz}^{1/2}/\text{W}$  under the bias voltages ( $\leq 3 \text{ V}$ ) yielding this high responsivity. InP/InGaAsP QWIP responsivity is between the responsivities of InP/InGaAs and AlGaAs/GaAs QWIPs. It reaches  $2 \text{ A/W}$  at  $30 \text{ kV/cm}$  average e-field. The energy band profile of the single QWIPs were given in Fig. 6.3. It is seen that conduction valley profiles of InP/InGaAs and InP/InGaAsP QWIPs are very similar. The difference between responsivities of these QWIPs can be attributed to photoconductive gain and absorption quantum efficiency difference, as explained in the following paragraphs. Stronger bound-to-continuum character of InP/InGaAsP QWIP results in broader spectral response, and this gives integrated blackbody responsivity which is %35 higher than that of InP/InGaAs QWIP.

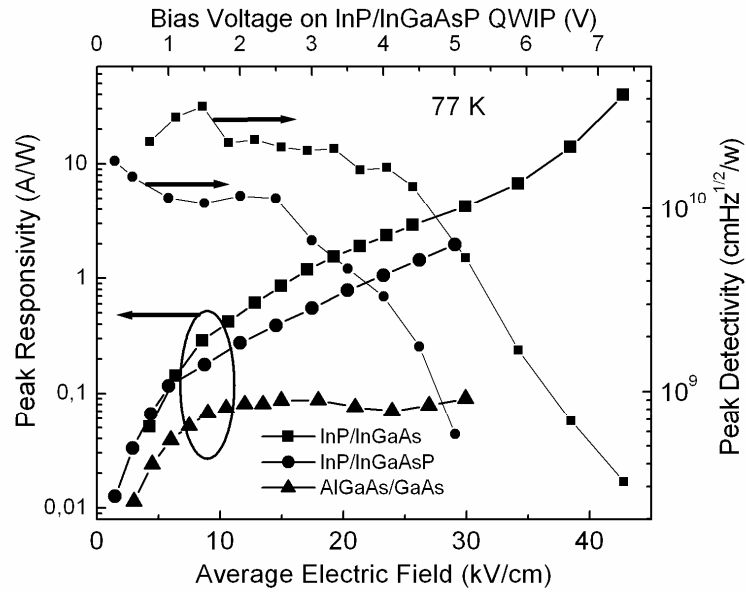


Figure 6.15 Peak responsivities of the investigated QWIPs, and the peak detectivity of the investigated InP based QWIPs (no cold shield) at 77 K.

Fig. 6.16 compares the 77 K noise gain obtained through noise and dark current measurements with the photoconductive gain in InP/InGaAs QWIP. The photoconductive gain is extracted from the responsivity measurements by assuming that the noise gain is equal to the photoconductive gain under moderately large bias voltages. This method calculates the absorption quantum efficiency ( $\eta$ ) of the InP/InGaAs QWIP to be 5.8%. The bias dependence of the noise gain follows that of the responsivity until the bias reaches  $\sim 3$  V. Assuming that the quantum efficiency does not significantly depend on bias in the bias region of interest, it can be concluded that the bias dependence of the noise gain is similar to that of the photoconductive gain. This shows that the impact ionization in LWIR InP/InGaAs QWIPs does not set in until the average electric field in the device reaches  $\sim 25$  kV/cm. Beyond this electric field, the rate of increase of the noise gain with bias is apparently much higher than that of the photoconductive gain. Similar observation was reported on GaAs/InGaAs QWIPs by Rehm *et. al.* [103].

Fig. 6.16 also shows the multiplication factor,  $M$ , [126,127] defined as the ratio of the noise gain to the photoconductive gain if the capture probability,  $p_c \ll 1$ , which is a good assumption for InP/InGaAs QWIPs as we have verified through ensemble Monte Carlo simulations [95]. While  $M \sim 1$  under low and moderately large bias, it rapidly increases with bias for bias voltages exceeding 3 V and becomes as high as  $\sim 200$  under 5 V. This observation is not consistent with that of Aslan *et. al.* [116] who reported the bias dependence of  $M$  in chemical beam epitaxy grown 20-well dual band InP/InGaAs QWIPs up to 3 V and observed the saturation of  $M$  around 2 for bias voltages exceeding 2 V. The rapid increase of  $M$  with increasing bias was also reported by Rehm *et. al.* for 20-well GaAs/InGaAs QWIPs for bias voltages exceeding  $\sim 3$  V. At comparable electric fields,  $M$ , in our case, seems to be larger when compared with that in GaAs/InGaAs QWIPs. As seen in the inset of Fig. 6.7, the activation energy becomes as low as  $\sim 60$  meV under large electric-fields, suggesting that the thermionic emission is not the dominant dark current generation mechanism under large bias. As shown in Fig. 6.4, the dark current density is independent of the detector dimensions implying that the additional generation

mechanism is not related with the surface effects. While it can be attributed to impact ionization, we believe that this phenomenon needs further investigation.

Figure 6.17 shows the noise and photoconductive gains of 20 QW InP/InGaAs and 30 QW InP/InGaAsP QWIPs. Again using the equality of the noise gain and photoconductive gain at low and medium electric fields, the quantum efficiency of InP/InGaAsP and InP/InGaAs QWIP are calculated to be %3.3 and %5.8 respectively. Lower peak absorption quantum efficiency of the InP/InGaAsP QWIP can be attributed to the stronger bound to continuum character which results in lower oscillator strength.

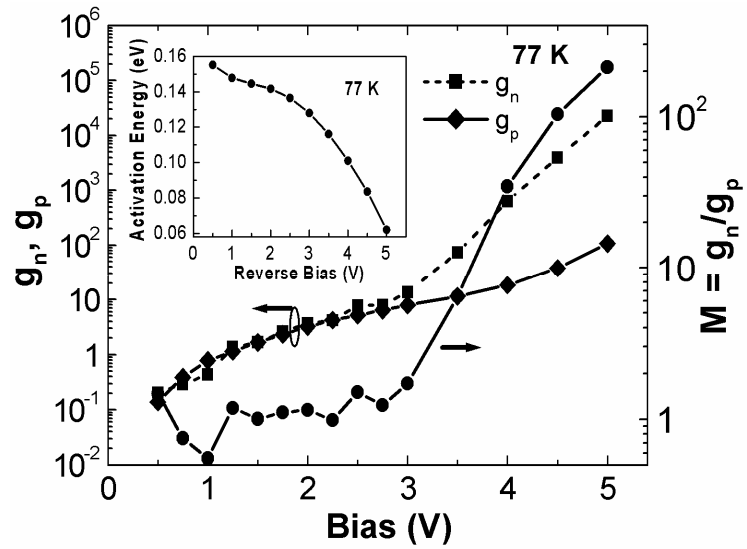


Figure 6.16 Noise and photoconductive gains of InP/InGaAs QWIP versus the bias voltage at 77 K. The activation energy extracted from the dark current measurements at different temperatures is shown in the inset [96].

Unexpectedly, 30 QW InP/InGaAsP QWIP shows higher photoconductive gain at low bias voltages. Stronger bound to continuum character of InP/InGaAsP QWIP results in lower wavefunction overlap between the ground state and excited state. Resulting smaller oscillator strength causes smaller capture probability and higher

photoconductive gain. This treatment is valid at these low electric field strengths where electrons are fully occupied in the  $\Gamma$  valley. Similar observation is observed in AlGaAs/GaAs QWIPs. As the bound-to-continuum character of the device becomes dominant the photoconductive gain increases. (See figure 2.5) [128].

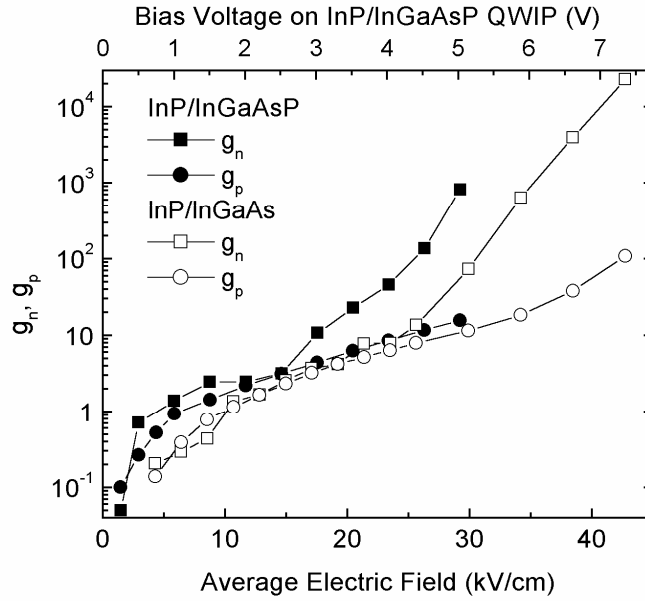


Figure 6.17 Noise and photoconductive gains of InP/InGaAs and InP/InGaAsP QWIP versus the bias voltage at 77 K.

As the applied reverse bias is increased, noise gain of InP/InGaAsP QWIP deviates from behavior of the photoconductive gain around near 15 kV/cm average electric field. This excess noise does not set-up until 22 kV/cm average electric field for the InP/InGaAs QWIP. Both of the devices have similar level of doping sheet density in QWs. The activation energy difference of 22 meV cannot be responsible from the 10 kV/cm threshold e-field which corresponds to 1.17 V potential difference through the 20 QW device. In these high gain ( $g_p \gg 1$ ) devices, an average electron injected from the contact reaches the collector without any capture. Hence, the probability for carrier multiplication becomes proportional to device active length.

The ratio of the length of the InP/InGaAsP QWIP to the length of InP/InGaAs QWIP is 1.47. Where the ratio of the multiplication threshold voltages 22 kV/cm and 15 kV/cm is 1.46. This result suggests that the device length can be effective in determining the multiplication threshold e-field.

Comparison of the experimental results with the Monte-Carlo simulations resulted in acceptable agreement, and allowed better explanation of carrier multiplication in QWIP. Figure 6.18 shows average drift distance of the electrons vs. average e-field relation. Drift distance is calculated by multiplying the photoconductive gain with device active length. Full squares represent the results of the simulations on  $\text{Al}_{0.3}\text{Ga}_{0.7}\text{As}$  QWIPs, and the full circles represent the drift distance characteristic obtained when the barrier material intervalley energy spacings are artificially increased to be equal to those in InP. There is reasonable agreement between the experimental and theoretical results up to the onset of impact ionization, which was not included in the simulations. The above results suggest that the drift distance strongly depends on the energy spacing between central and satellite valleys in the conduction band of the barrier material.

One of the important conclusions that can be drawn from the above observations is that the InP–InGaAs QWIPs operate with reasonably high responsivity and detectivity under moderately large bias up to an average E-field of 25 kV/cm. While the higher responsivity in InP/InGaAs QWIPs in this bias region was attributed to better transport properties in the binary barrier material [119], our recent MC simulations suggest that it mainly results from higher excited electron lifetime [17, 95]. Due to the larger energy separations between the  $\Gamma$  and satellite valleys in InP when compared with those in  $\text{Al}_{0.3}\text{Ga}_{0.7}\text{As}$ , the excited electrons in InP/InGaAs QWIP can achieve higher kinetic energy under moderate and large bias, which makes electron capture less probable [95]. InP/InGaAsP QWIP offers high responsivity and similar characteristics with InP/InGaAs QWIP, together with peak responsivity wavelength in LWIR band. InP/InGaAsP QWIP has %35 higher integrated blackbody responsivity than that of InP/InGaAs QWIP. Measured 71 K

BLIP temperature of InP/InGaAsP QWIP, and  $1 \times 10^{10} \text{ cm.Hz}^{1/2}/\text{W}$  detectivity makes this device promising for thermal imaging applications.

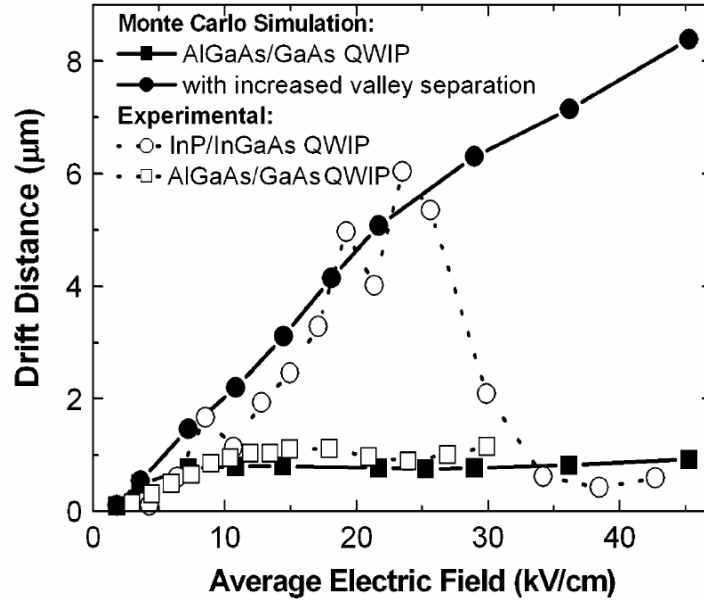


Figure 6.18 Comparison of the observed drift distance with the results of ensemble Monte-Carlo Simulator [96].

## 6.6 Low Temperature/Low Background Characterization of InP/InGaAs QWIP

Operation of QWIPs at temperatures much lower than 77 K may be essential in low background space based applications. An example to these applications is space based strategic applications to detect outer atmosphere missiles. Under these conditions, conventional AlGaAs/GaAs QWIPs display anomalous behavior such as long DC current time-constant [129], zero-bias offset [130-131], and responsivity roll-off at high optical signal frequencies [131-132]. Long response time-constant observed in AlGaAs/GaAs QWIPs may create problems in infrared imagers with direct injection read-out scheme where the DC bias on the detector monotonously



decreases as the integration capacitor is filled with the detector current. Hence, a long time constant creates a residual voltage on the pixel, and the variation of this residual voltage from pixel to pixel may create spatial non-uniformity on the imaging array resulting in NETD degradation. A comparison of the characteristics of AlGaAs/GaAs and InP/InGaAs QWIPs under low temperature/low background conditions is done experimentally in this study.

Figure 6.19 shows the 77 K responsivity spectrum and the 40 K dark currents of InP/InGaAs and AlGaAs/GaAs QWIPs. Both QWIPs display peak responsivity wavelength near 8  $\mu\text{m}$  with the 40 K dark current of InP/InGaAs QWIP lower than that of the AlGaAs/GaAs QWIP significantly. Experimental observations have suggested that both QWIPs are of the bound to quasi bound type.

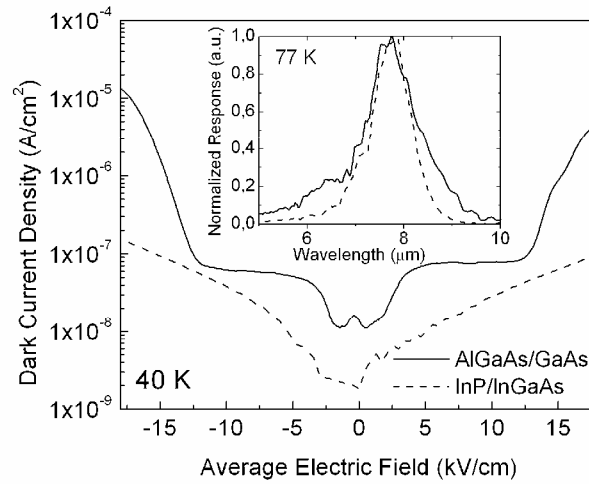


Figure 6.19 77 K responsivity spectrum and the 40 K dark currents of InP/InGaAs and AlGaAs/GaAs QWIPs.

The photodetectors are installed in He cryostat with  $f/2$  cold shield. For low background measurements detectors are exposed to the cryostat cold shield without aperture where the shield is at the same temperature with the sample. For 300K background measurements, radiation ( $92 \mu\text{W}/\text{cm}^2$ ) from the blackbody source is

modulated with a chopper. The signal from the QWIP is preamplified with a low noise transimpedance amplifier, and the signal at the chopping frequency is measured with a lock-in amplifier. Figure 6.20 shows the measured optical signal versus chopper frequency plot for both QWIPs under various electric field strengths.

The responsivity of AlGaAs/GaAs QWIP rolls-off strongly with chopper frequency under low and moderate e-fields, and weaker roll-off is observed at  $-18$  kV/cm. Interestingly, insignificant roll-off is observed in InP/InGaAs QWIP under all e-field strengths used in this study. Figure 6.21 shows I-V sweep results of the detectors at 40 K. Applied bias on the detectors is swept with 0.9 kV/cm steps with 1 ms measurement delay after each bias change. AlGaAs/GaAs QWIP I-V characteristic displays considerably larger zero-bias offset and stronger hysteresis effect.

Figure 6.22 shows the measured dynamic resistivity of the test detectors. The detectors have similar dynamic resistivities below the electric field strength of 12 kV/cm. Similar tunneling characteristics are expected for the two structures.

The QWIP circuit model developed by Singh and Cardimona [130] models each period with a barrier resistance ( $R_b$ ) in parallel with series connected quantum well capacitance ( $C_{QW}$ ) and tunneling resistance ( $R_t$ ). Determination of the individual effects of various parameters of the QWIP on the above described anomalous behavior is quite difficult. The results presented in this section show that InP/InGaAs QWIPs with lower dark currents and similar dynamic resistances offer wider bandwidth and smaller zero bias offsets when compared with AlGaAs/GaAs QWIPs under low temperature/low background conditions.

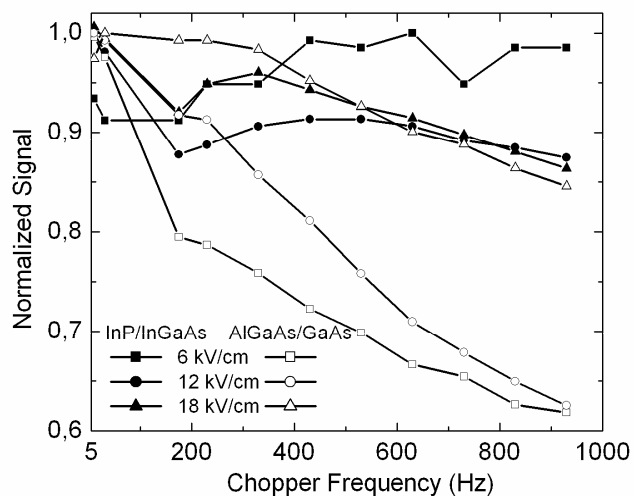


Figure 6.20 InP/InGaAs QWIP and AlGaAs/GaAs QWIP optical signal dependence on chopper frequency at 40 K.

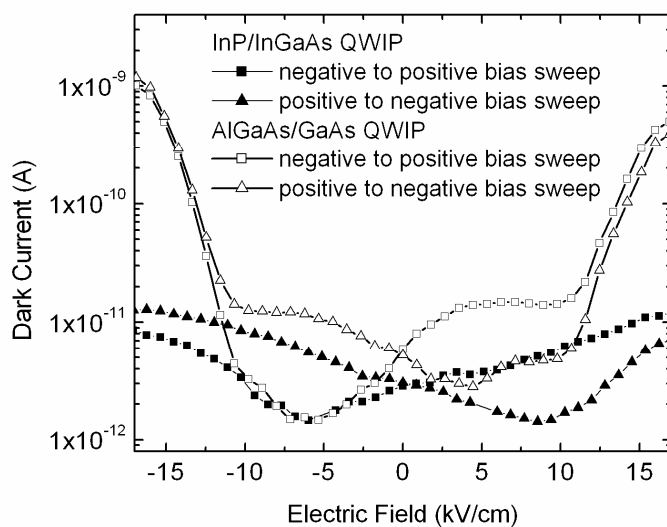


Figure 6.21 Voltage applied onto the test detectors are swept in both directions. AlGaAs/GaAs QWIP zero-bias offset and hysteresis character is stronger than that of InP/InGaAs QWIP

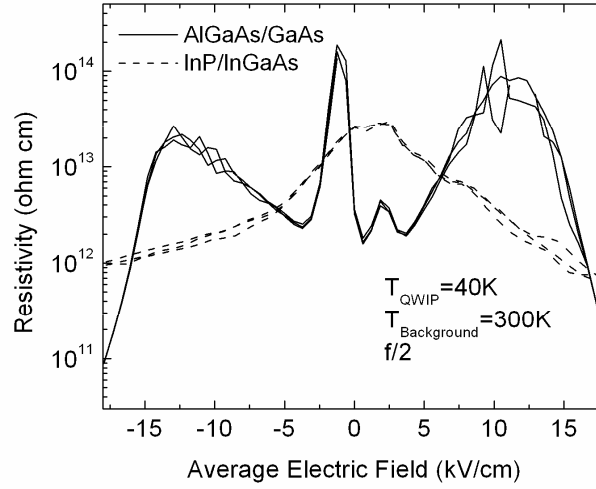


Figure 6.22 Measured resistivity of AlGaAs/GaAs QWIP and InP/InGaAs QWIP test detectors at 40K under f/2 300K background.

It should also be noted that InP/InGaAs QWIPs display a roll-off characteristic quite similar to that of AlGaAs/GaAs QWIPs at 18 kV/cm e-field where the dynamic resistance of InP/InGaAs QWIP is one order of magnitude higher. The considerable difference in the responsivity roll-off characteristics of AlGaAs/GaAs and InP/InGaAs QWIPs with similar dynamic resistance may also be due to the presence of DX centers in AlGaAs. Although GaAs QWs are center doped to avoid dopant diffusion into barriers, impurities in the AlGaAs may create optically active DX centers which introduce carrier trapping/release processes with long time constant [129]. While a very detailed investigation is necessary to clarify this issue, the results of this work suggest that InP/InGaAs QWIPs offer an important advantage for low temperature/low background applications.

## 6.7 Conclusions

This section included detailed characterization results of 21  $\mu\text{m}$  x 21  $\mu\text{m}$  sized InP/InGaAs, InP/InGaAsP, and AlGaAs/GaAs QWIP test detectors. At 70 K, the

InP /InGaAs based QWIPs show background limited performance ( $f/2$ ) with a detectivity above  $10^{10}$  cmHz<sup>1/2</sup>/W up to 3 V reverse bias where the responsivity (2.9 A/W) is an order of magnitude higher than that of AlGaAs/GaAs QWIPs. The results suggest that the impact ionization does not start until the average E-field in the device reaches 25 kV/cm in InP/InGaAs QWIPs, and the relatively high responsivity for lower E-fields is due to the large photoconductive gain. InP/InGaAsP QWIP operation is multiplication free until average e-field of 15 kV/cm and the device offers 1 A/W peak responsivity at this point. In addition to the other advantages of the InP/InGaAs material system over AlGaAs/GaAs, this property of InP based LWIR QWIPs can be utilized for thermal imaging applications requiring high responsivity and shorter integration times together with higher noise floor.

Space based strategic applications require operation at low temperatures and low background conditions. Standard AlGaAs/GaAs QWIPs show anomalous behavior at low temperature and low background conditions which may be related to trapping states in barrier material. It is shown that InP/InGaAs QWIP has advantages over AlGaAs/GaAs QWIP by offering higher frequencies at 40K operating temperature. Moreover, InP/InGaAs QWIP show weaker hysteresis character to bias voltage sweeping under low background conditions when compared with AlGaAs/GaAs QWIP.

From system level point of view, there are two cases that make InP based LWIR QWIPs advantageous over standard QWIP AlGaAs/GaAs technology. One of them is low background applications where signal level is low due to low background photon flux. In this case, signal can interfere with system noise floor. In another case, if the operating environment increases system noise floor, then even with high backgrounds, detector signal can be buried into system noise. In both of these cases high signal and high noise floor InP LWIR QWIPs are easier to operate with reduced effect of system noise. For thermal imaging applications, this issue is explained in more detail in the following chapter.

## **CHAPTER 7**

### **InP BASED LWIR QWIP FOCAL PLANE ARRAY PERFORMANCE**

In the preceding chapter, the performance of the fabricated test detectors of InP/InGaAs, InP/InGaAsP, and AlGaAs/GaAs QWIPs were discussed. This chapter presents a discussion of the performance of the fabricated 640x512 format focal plane array performance. The fabrication process is summarized and the FPA test procedure is explained. The NETD and uniformity of the fabricated FPAs are compared at different operating conditions.

#### **7.1 FPA Fabrication**

The 640x512 QWIP FPA fabrication process starts with unprocessed 26mm x 26 mm pieces diced from 3" epiwafers which are grown at commercial epiwafer foundries. Bare QWIP epilayer pieces are processed to form 640x512 format matrices of photodetectors to couple them to a commercial 640x512 ROIC. The fabrication steps of QWIP FPA are (Figure 7.1) :

- i. Alignment mark deposition
- ii. Grating etching
- iii. Mesa etching
- iv. Ohmic contact deposition and annealing
- v. Reflector coating
- vi. Passivation coating and etching
- vii. Under-bump metallization coating
- viii. Indium electroplating
- ix. ROIC post-processing
- x. Flip-chip bonding
- xi. Underfill injection
- xii. Substrate thinning

Above summarized large format FPA fabrication process was developed in collaboration with Dr. Selçuk Özer who completed his Ph.D. study in 2005 under the scope of the same research project. Dr. Selçuk Özer developed the FPA fabrication process starting with 128x128 format FPAs with different types of p-i-n and QWIP photodetectors. He contributed to development of mesa etch, grating etch, ohmic contacts, reflector coating, passivation, under-bump metallization, indium electroplating, ROIC post-processing, and flip-chip bonding processes for different type of photodetectors [133]. Under the scope of this Ph.D. study, contributions are done to the design and fabrication of optical gratings, indium electroplating, passivation layer coating, device characterization, wet etching and RIE etching, ohmic contacts, underfilling, substrate lapping processes of AlGaAs/GaAs, InP/InGaAs, and InP/InGaAsP QWIPs. In addition, Ümit Tümkaya, and Burak Aşıcı contributed to the IR FPA fabrication technology development work. Related to the topics presented in this thesis study Ümit Tümkaya contributed to the QWIP FPA lithography mask design and substrate lapping processes. Burak Aşıcı performed flip-chip bonding of the InP/InGaAsP QWIP FPA and its test detectors. Due to confidential nature of the process development study, the details of the fabrication process will not be reported in this

thesis. The following sections will concentrate on the FPA characterization results of scientific value. The first step of fabrication is depositing gold alignment marks followed by grating etching in order to couple normally incident light to QWs. QWIP mesa etching is done by RIE in order to obtain vertical mesa side wall profile for better fill factor. Ohmic contacts to each mesa are obtained by evaporating AuGe/Ni/Au metal stack and subsequent annealing. In order to passivate the mesa sidewall, and to isolate the FPA, a suitable passivation layer is coated and openings are etched onto the top of each mesa. Before indium hybridization, under bump metallization (UBM) is done onto each mesa contact area together with necessary electrical short for electroplating. Indium electroplating is done by creating thick photoresist mold onto the FPA surface. Electroplated indium is grown in the mold until necessary total bump thickness is reached. Removing the mold and the electrical short cut remains the FPA ready for flip chip bonding. The ROIC circuit is prepared and flip-chip bonding is done with the intention of illuminating the FPA from backside. For mechanical strength, an underfill epoxy is injected through the gap between the FPA and the ROIC. FPA substrate thinning is necessary to avoid thermal stress and reduced lifetime as well as to decrease optical crosstalk and increase absorption quantum efficiency. The substrate thinning is done mechanically with abrasive lapping.

## **7.2 FPA Characterization Set-up**

Characterization of the fabricated FPAs were done by wire bonding the ROIC-FPA hybrid onto an 84 pin LCC package and installing them into a laboratory test camera (Fig. 7.2). The camera houses commercial infrared camera electronics specially configured for the ISC9803 ROIC. The camera has liquid nitrogen cooled test dewar with a fanout board. The dewar is connected to proximity electronics with 4 channel 14 bit A/D conversion capability.



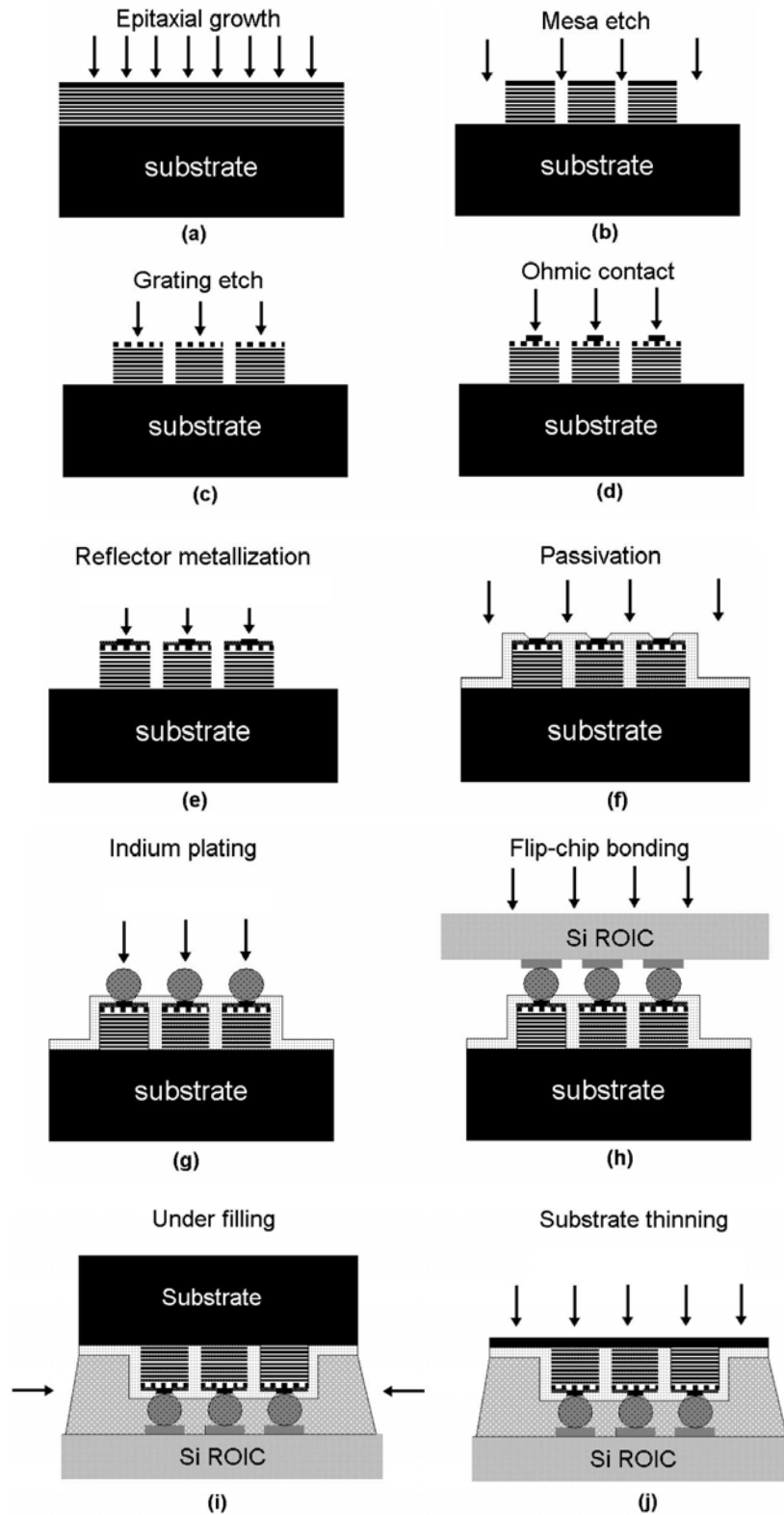


Figure 7.1 Fabrication steps of IR QWIP staring FPA.[133]

The proximity board is an interface between the DSP board and the sensor. The DSP board generates necessary timing patterns and acquires the digital image data from the proximity board. Real time two point nonuniformity correction is done on this board with the stored tables in the E<sup>2</sup>PROM.

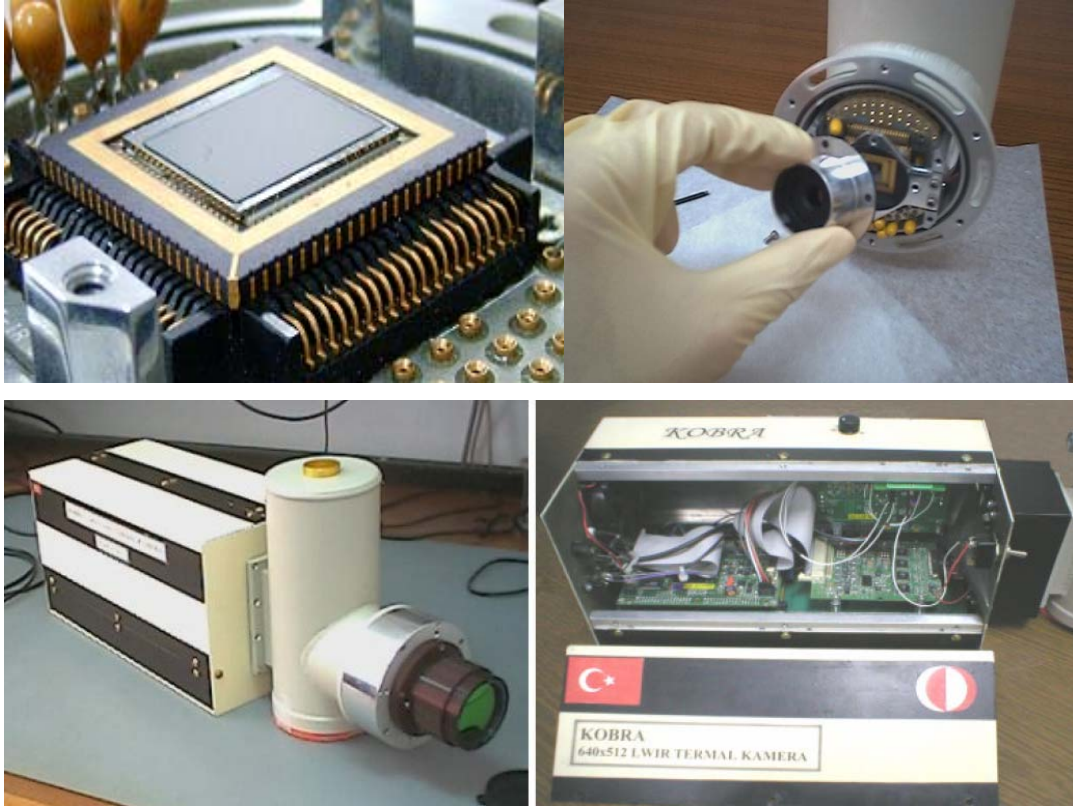


Figure 7.2 QWIP focal plane array wire bonded onto 84 pin LCC package and installed into thermal camera with liquid nitrogen cooled FPA test dewar.

### 7.2.1 Camera

The liquid nitrogen cooled dewar has a bayonet mount which holds the exterior exit pupil 50 mm commercial thermal imaging lens. The 640x512 QWIP FPA with 25  $\mu\text{m}$  pitch has image size of 16 mm x 12.8 mm and diagonal of 20.5 mm. The lens

has maximum image diameter of 21 mm (Fig. 7.3). The effective focal length is 50 mm which corresponds to 18° horizontal FOV and 15° vertical FOV. The transmission window of the lens is 7  $\mu\text{m}$  – 12  $\mu\text{m}$  with typical transmission of %95. The lens assembly is outside the vacuum chamber where the interface between the optics and the vacuum chamber is a 1" x 1 mm Ge dewar window with optical transmission of %92. Since QWIP is a narrow band photodetector, a cold filter is not used. The cold stop of the dewar (Figure 7.2) defines the background flux collected from the dewar. Due to mechanical limitations, the cold shield is set to f/1.5. The lens f/# is 2, which corresponds to 38  $\mu\text{m}$  diffraction blur spot at 8  $\mu\text{m}$  wavelength which is common in similar pitch staring infrared cameras.

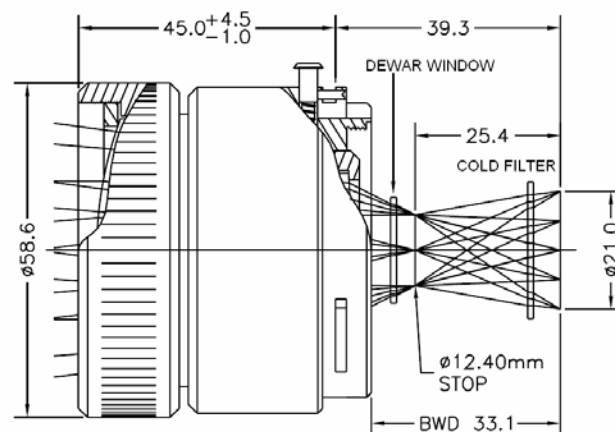


Figure 7.3 LWIR thermal imaging lens with 50 mm effective focal length.

### 7.2.2 Read-out Integrated Circuit

The ROIC is ISC9803 640x512 read out integrated circuit from FLIR Systems (Indigo Systems Operations). The ROIC technical specifications is in table 7.1. The ROIC has aluminum indium bonding pad openings at each pixel center, and the electrical common connection to the detector array is done via five column indium

bonding pads surrounding the ROIC. The photocurrent injection circuit of the ROIC is of direct injection type and its schematic is given in Figure 7.4 [134]. The detector bias is done via  $V_{\text{detcom}}$  pad indicated in the figure. The maximum reverse bias on the photodetector is limited to 3.5 V due to ROIC limitations.  $V_{\text{bias\_adj}}$  pin indicated in the figure is intended for low bias photovoltaic detector applications and set to maximum in this study. Nominal injection current of the ROIC is specified to be 1 nA and the integration capacitor storage capacity is 11 million electrons. This allowed integration times up to 15 ms as presented in the following sections. All of the detector pixels fabricated during this study gave dynamic resistance at least on the order of  $10^8 \Omega$  (Figure 7.4) which results in charge injection efficiency approaching %100, in agreement with reported results in the literature[62,20]. The ROIC input referred noise is specified to be 550 electrons without any injection into the circuit.

Table 7.1: Technical Specifications of ISC9803 ROIC [134]

<b>Format</b>	640 x 512
<b>Pixel Pitch</b>	25 $\mu\text{m}$
<b>Storage Capacity</b>	11 $\text{Me}^-$
<b>Operability</b>	>%99.99
<b>Dynamic Range</b>	>72 dB
<b>Read-out Noise</b>	<500 electrons
<b>Non-Linearity</b>	< %0.5
<b>Cross Talk</b>	< %0.1
<b>Input Polarity</b>	p on n
<b>Integration Time</b>	> 9.6 $\mu\text{s}$ , adjustable
<b>Outputs</b>	4
<b>Output Signal Swing</b>	2.5 volts
<b>Power Consumption</b>	< 180 mW at 107 Hz 4 outputs
<b>Maximum Frame Rate</b>	107 Hz 4 outputs
<b>Video Output</b>	NTSC or PAL

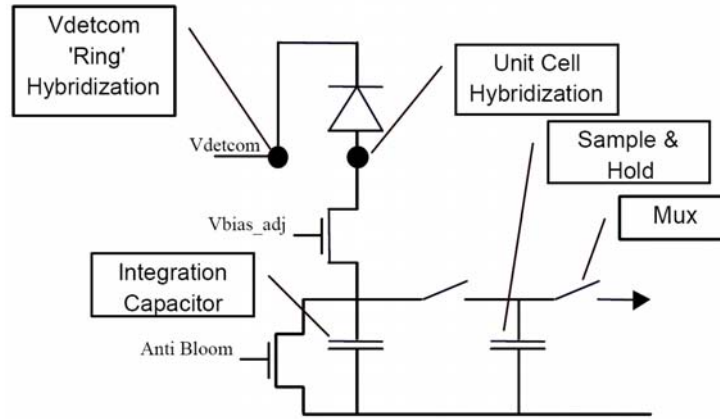


Figure 7.4 Direct injection type input circuit of ISC9803 ROIC [134].

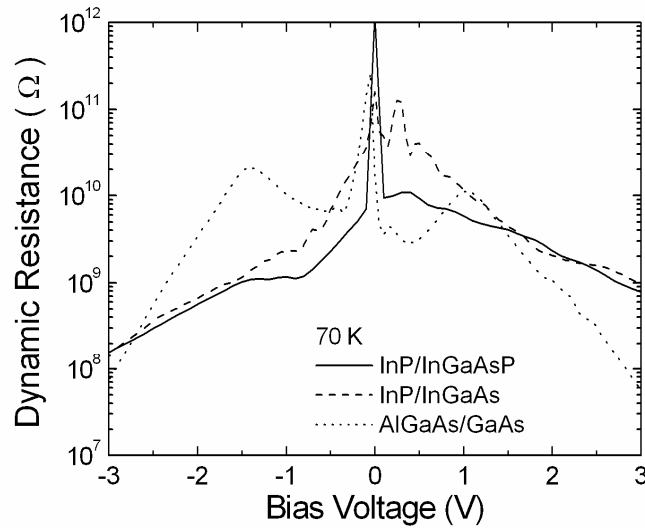


Figure 7.5 Dynamic resistance of the FPA pixels at 70 K operating temperature and 300 K background.

Worst case number of noise electrons injected into the ROIC can be calculated by assuming photoelectron generation-recombination noise is dominant. Experimentally measured noise gain of the test detectors which have the same size and properties with the FPA pixels is used in the calculations. Table 7.2 shows summary of this calculation. During frame integration, the detector bias voltage monotonously decreases as the direct injection ROIC integration capacitor is filled.

The specified bias voltage is the approximate bias value at the beginning of the integration.

Table 7.2 Noise electrons of QWIP at the ROIC integration capacitor, with ~10 ms integration time at 70K. Calculations assume near unity ROIC injection efficiency.

Device	Total Current	$g_n$	$i_n^{GR}$ (fA)	$R_d$ (G $\Omega$ )	$i_n$ (Johnson noise)	G-R noise electrons	Johnson noise electrons	Total noise electrons
InP/InGaAsP @ -0.25 V	40 pA	0.05	25	4.5	6.6 fA	1560	413	<b>1613</b>
InP/InGaAs @ -0.5 V	30 pA	0.20	14	6.9	5.3 fA	875	331	<b>936</b>
AlGaAs/GaAs @ -0.5 V	38 pA	0.01 1	3.6	6.9	5.3 fA	225	331	<b>400</b>

InP based QWIPs offer the same level of NETD with standard AlGaAs/GaAs QWIPs. As table 7.2 shows same SNR level is obtained with higher detector noise floor. Specified ROIC noise is 550 electrons with minimum ROIC gain to allow maximum integration time. The example AlGaAs/GaAs QWIP investigated in this study has 400 electrons noise which is competing with the system noise at the input node. The ROIC noise power is %65 of the total noise power at the ROIC output. On the other hand InP/InGaAs LWIR QWIP have noise level of 936 electrons and offer similar level of SNR with standard QWIPs as shown in the following sections. The ROIC noise power is only %25 of the total noise power in the case of InP/InGaAs QWIP which is at an acceptable level. This situation is similar to MWIR FPA systems which suffer from low background signal level, and high system noise floor. When external system noise is an important issue, InP LWIR QWIPs offer better tolerance to keep the whole system “detector limited” since it offers good SNR with higher signal, and higher noise floor.

### 7.2.3 FPA Characterization Method

In order to evaluate the signal and noise response of the FPA to different background temperature levels, 14-bit digital data from the camera electronics is acquired to the computer. The system is capable of real time data acquisition from the camera. A calibrated wide area blackbody is used to expose the FPA to variable temperature background. The blackbody surface is set to a differential temperature with respect to a unity emissivity room temperature plate (Figure 7.6).

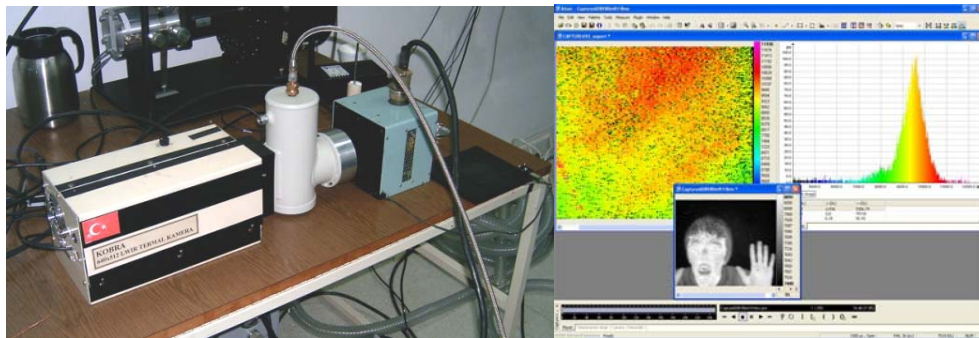


Figure 7.6 FPA Characterization set-up with camera exposed to wide area blackbody, and snapshot screen from data acquisition software.

In order to measure NETD, the FPA is exposed to uniform room temperature background and 128 frame real time movie is recorded without any correction. Following this, 128 frame real time movie is recorded while the FPA is exposed to blackbody target which is maintained 10 K above room temperature. Taking time average of these films gives “hot” and “cold” average frames. Differencing these average frames, and dividing to 10 K results in responsivity frame. Responsivity frame is an 640x512 frame where at each pixel location, that pixel’s signal to 1 K background difference is recorded. Another 128 frame real time movie is recorded

when the FPA is exposed to blackbody target which is maintained 5 K above room temperature. In time axis, taking standard deviation of each pixel's value gives noise of that pixel. Collecting these in 640x512 format frame results in “noise frame”. Pixel by pixel dividing noise frame to responsivity frame results in NETD frame.

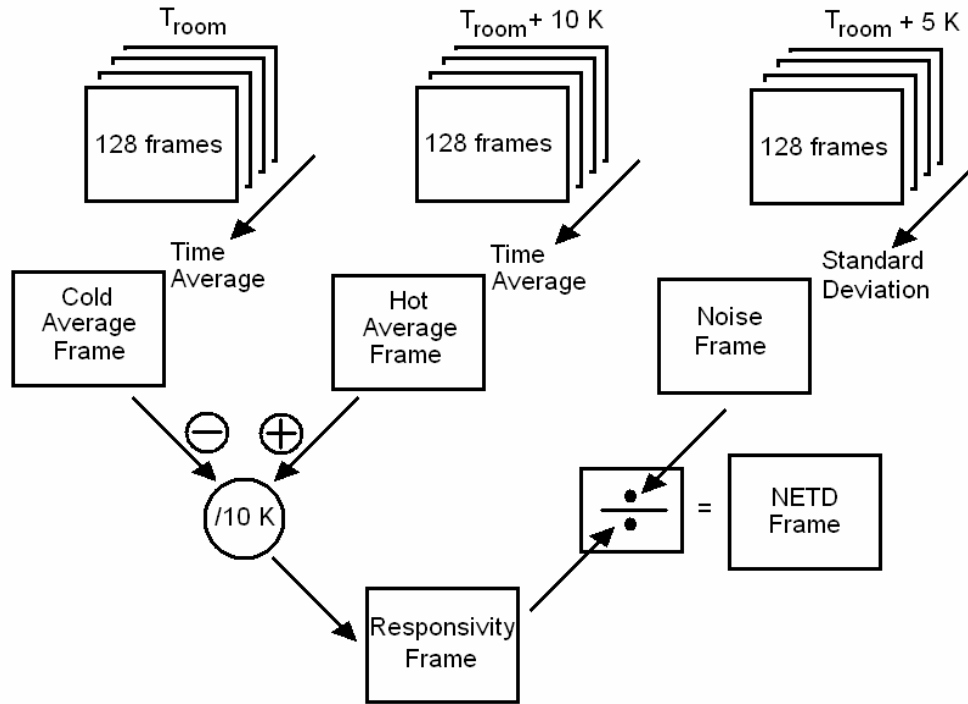


Figure 7.7 NETD measurement method using variable temperature blackbody

Calculated NETD with this procedure can be expressed as in Equation 7.1. In the equation  $\rho_{i,j,k}^{\text{cold}}$  represents the signal value of pixel at row  $i$  and column  $j$  of frame  $k$  when the FPA is exposed to plate at room temperature. “hot” means FPA is exposed to plate which is 10 K above room temperature, and “warm” means FPA is exposed to plate which is 5 K above room temperature.



$$NETD_{i,j} = \frac{noise_{i,j}}{d\rho_{Average}/dT_{Background}} = \frac{\sqrt{\frac{1}{N} \sum_{k=1}^N \left( \rho_{i,j,k}^{warm} - \frac{1}{N} \sum_{k=1}^N \rho_{i,j,k}^{warm} \right)^2}}{\frac{1}{T_{Hot} - T_{Cold}} \left[ \frac{1}{N} \sum_{k=1}^N \rho_{i,j,k}^{hot} - \frac{1}{N} \sum_{k=1}^N \rho_{i,j,k}^{cold} \right]} \quad (7.1)$$

Using the histogram of corrected/uncorrected hot and cold average frames, corrected/uncorrected DC signal uniformity is obtained. Pixels with negative response or NETD value above 500 mK are assumed to be dead in these calculations.

In imaging applications, at a fixed set bias voltage, the integration time is adjusted to keep the integration capacitors at %50 value of their capacity. This allows imaging objects with maximum dynamic range. For special cases, integration time can be further increased in order to decrease noise bandwidth and improve NETD. In this case dynamic range is sacrificed.

### 7.3 Focal Plane Array Performance

Figure 7.8. shows the mean NETD of the 640x512 InP/InGaAs QWIP FPA versus the detector bias at 70 and 77 K with half filled ROIC capacitors and f/1.5 optical aperture. Due to a small misalignment during flip-chip bonding, a small percentage of the pixels (gathered at one corner) had no electrical connection with the corresponding ROIC pixels. These pixels and those with NETD values above 500 mK were excluded in the calculation of the mean NETD. The total number of bad pixels was smaller than ~3%. It should be noted that the FPA yields reasonably low NETD ( $\leq 83$  mK) at 70 K even under moderately large bias voltages which offer very high responsivity. From 0.25 V to 3 V bias, NETD increases monotonically, while the detectivity stays almost constant (Fig. 6.15). This deviation from the detectivity limited NETD can be attributed to increase in noise bandwidth with decreasing integration time.

Figure 7.9 shows the variation of NETD of InP/InGaAs QWIP with the integration time (half filled ROIC capacitors, f/1.5 optics). At 70K with %50 filled integration capacitors, NETD reaches 36 mK at 11.5 ms integration time, while 77 K measured NETD is 40 mK at 16.5 ms. At 70 K, the FPA yields reasonably low NETD with sub-millisecond integration times, and, as expected, the NETD is nearly proportional to the inverse of the square root of the integration time up to  $\sim 1$  ms. For larger integration times, the decrease in NETD with increasing integration time is slower.

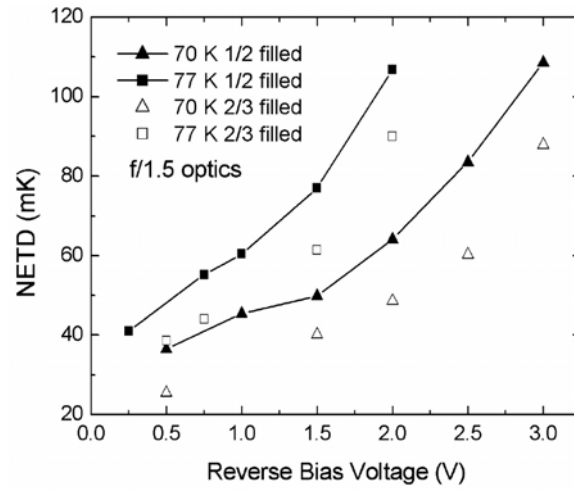


Figure 7.8 Mean NETD of the 640x512 InP/InGaAs QWIP FPA versus bias voltage.

640x512 InP/InGaAsP QWIP FPA fabrication resulted in %71 yield in flip-chip bonding connections due to a planarity error during flip-chip bonding process. Hence %99 operational lower right 320x256 window of the FPA is investigated by using windowing option of the ROIC. NETD characterization of InP/InGaAsP QWIP is only done at 70 K FPA temperature since the detector is not BLIP at 77 K. Figure 7.10 shows the variation of NETD with reverse bias voltage. NETD of InP/InGaAsP QWIP is higher as expected since it is a longer wavelength

photodetector with lower detectivity. However the device reaches 56 mK NETD value at 8 ms integration time with f/1.5 optics which is reasonably low.

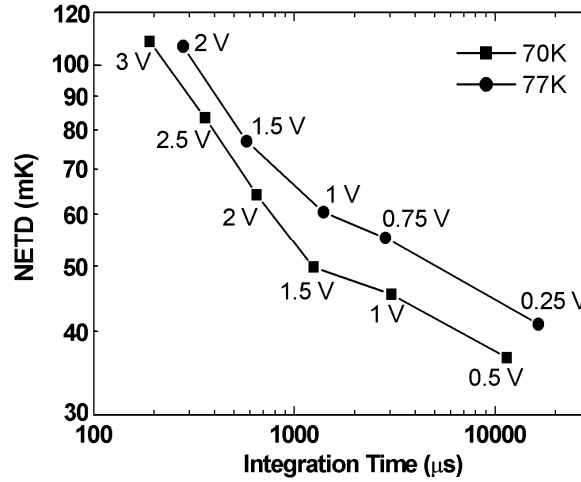


Figure 7.9 Mean NETD of the 640x512 InP/InGaAs QWIP FPA versus integration time when integration capacitors are half filled.

Figure 7.11 shows NETD variation of the investigated InP based QWIPs with integration time. When integration capacitor is %50 filled, longer wavelength InP/InGaAsP QWIP can reach 8 ms integration time at 10 mV reverse bias, and shorter wavelength InP/InGaAs QWIP can reach 15.9 ms integration time. The sensitivity of these FPAs can be improved by at least 30% if anti-reflection coating is used, the fill factor (71%) is increased, and the optical grating is optimized in which case the NETD performance of the FPA becomes comparable to the state of the art 640x512 LWIR AlGaAs/GaAs QWIP FPAs while offering higher frame rates [135].

Figure 7.12 shows the uncorrected NETD histogram of the InP/InGaAs QWIP FPA. The NETD nonuniformity ( $\sigma/\text{mean}$ ) is 17% which is comparable to that of LWIR AlGaAs/GaAs QWIP FPAs with the same format [135].

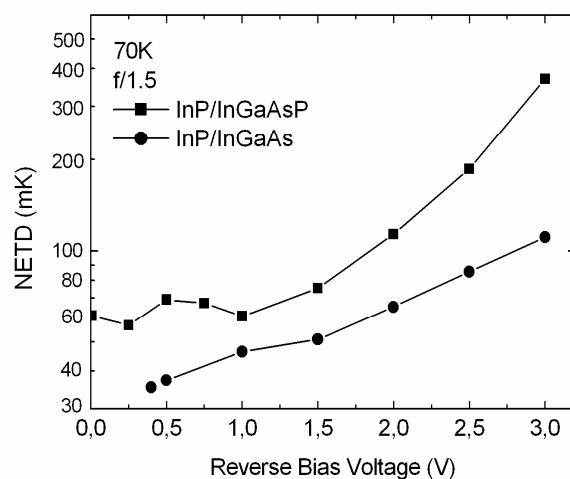


Figure 7.10 Mean NETD of the 640x512 InP/InGaAs and 320x256 window of 640x512 InP/InGaAsP QWIP FPA at 70K with f/1.5 aperture when the integration capacitors are %50 full.

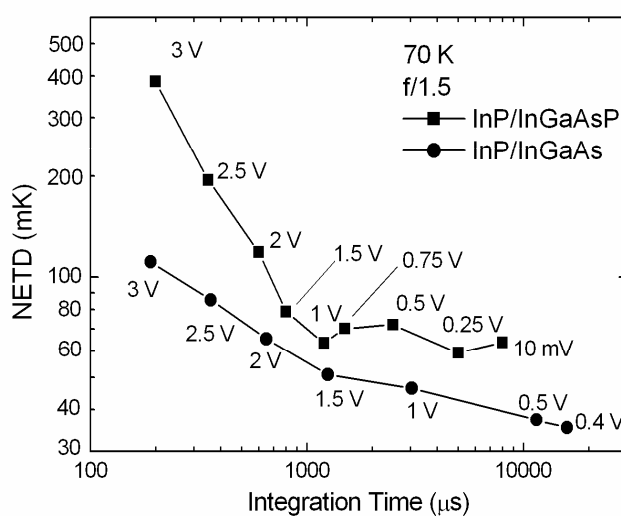


Figure 7.11 Mean NETD of the 640x512 InP/InGaAs QWIP FPA and 320x256 window of 640x512 InP/InGaAsP QWIP FPA at 70K with f/1.5 aperture, when the integration capacitors are %50 full.

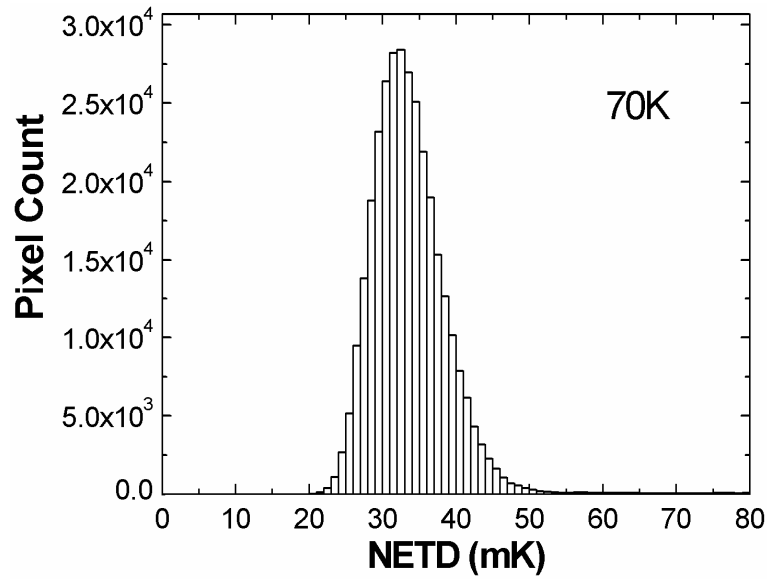


Figure 7.12 Uncorrected NETD histogram of the 640x512 InP/InGaAs QWIP FPA at 70 K with 0.5 V bias when integration capacitors are %50 full [96].

Figure 7.13 shows uncorrected NETD histogram of 320x256 windowed InP/InGaAsP QWIP FPA at 0.25 V reverse bias with 5 ms integration time. The histogram peak is around 38 mK showing potential of this material for high quality imaging. The average NETD is calculated reported to be 59 mK. This discrepancy between histogram peak and average NETD is due to defected pixels whose NETD is far from the main histogram peak. %1 of the pixels have NETD above 500 mK, however %12 of the pixels in the window have NETD value above 100 mK which is the reason of higher average NETD.

Figures 7.14 and 7.15 show corrected DC signal uniformity of InP/InGaAs and InP/InGaAsP QWIP FPA structures. Both devices have two point corrected DC signal uniformity on the order of  $10^{-4}$ . Although InP/InGaAsP QWIP FPA is windowed to its  $\frac{1}{4}$  size (320x256) this uniformity level is promising for future FPA prototyping.

Detectivity limited noise equivalent temperature difference (NETD) is given as [20]

$$NETD = \frac{(4f^2 + 1) \cdot \sqrt{A \Delta f}}{D_B^* \cdot \frac{dP_B}{dT}} \quad (7.1)$$

where  $\Delta f$  is the noise bandwidth,  $D^*$  is the blackbody detectivity,  $A$  is the active pixel area,  $dP_B/dT$  is the background temperature derivative of integrated blackbody power at 300 K background temperature, and  $f=1.5$  is the f-number of the dewar aperture. This calculation estimates a detectivity limited NETD of 25 mK for InP/InGaAs, and 50 mK for InP/InGaAsP QWIP. These calculations are in reasonable agreement with measured NETD values.

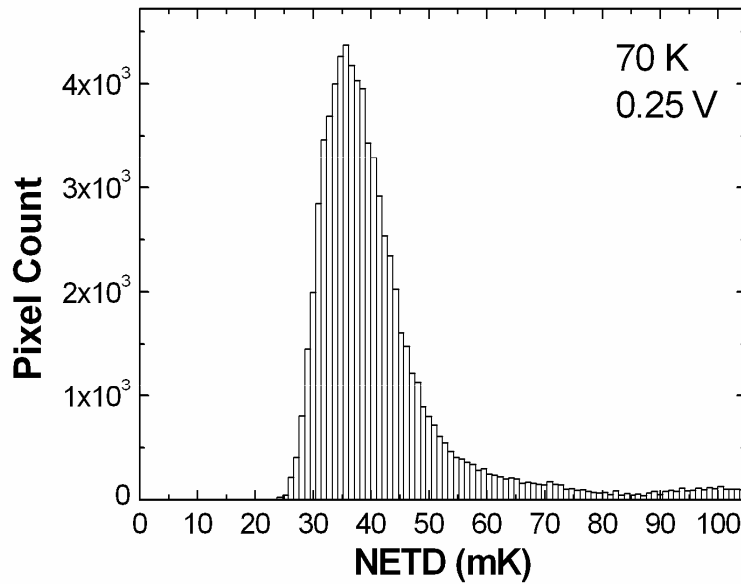


Figure 7.13 Uncorrected NETD histogram of the 320x256 window of InP/InGaAsP QWIP FPA at 70 K with 0.25 V bias, 5 ms integration time, and %50 filled integration capacitors.

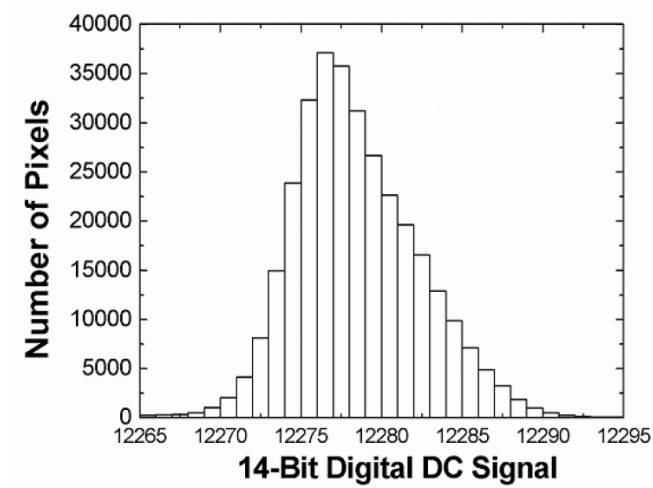


Figure 7.14 Corrected digital output of the 640x512 InP/InGaAs FPA at 77K temperature and 307 K background, demonstrating uniformity level of  $10^{-4}$ . [136]

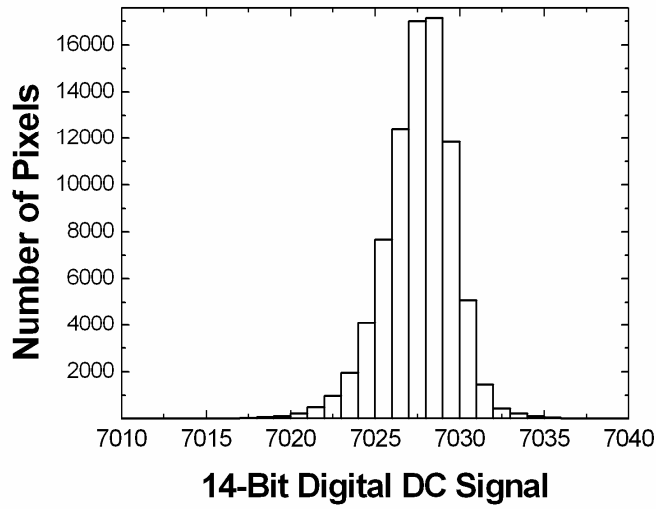


Figure 7.15 Corrected digital output of the 640x512 InP/InGaAsP FPA with lower right 320x256 windowing at 70K temperature and 300 K background, demonstrating uniformity level of  $10^{-4}$ .

Figures 7.16 and 7.17 show indoor and outdoor thermal images taken with the 640x512 InP/InGaAs QWIP FPA at a sensor temperature of 70 K using 50 mm

effective focal length thermal imaging lens. The field of view in this case is  $18.2^\circ \times 14.6^\circ$ . In order to eliminate the bad pixels ( $<3\%$ ) gathered at the top right corner, the images are windowed with the format of  $640 \times 448$ . The integration times for indoor and outdoor images are 4 and 7.5 ms, respectively. The outdoor image was taken at a winter night when the outside temperature was  $-6^\circ\text{C}$ .

Figures 7.18 and 7.19 show  $640 \times 512$  full window thermal images obtained with InP/InGaAs QWIP using 150 mm effective focal length thermal imaging lens. The field of view with this lens is  $6.1^\circ \times 4.9^\circ$ . The images are recorded in December 2005 at near zero centigrade ambient temperature. Low background flux allowed long integration time of 17 ms in this case.

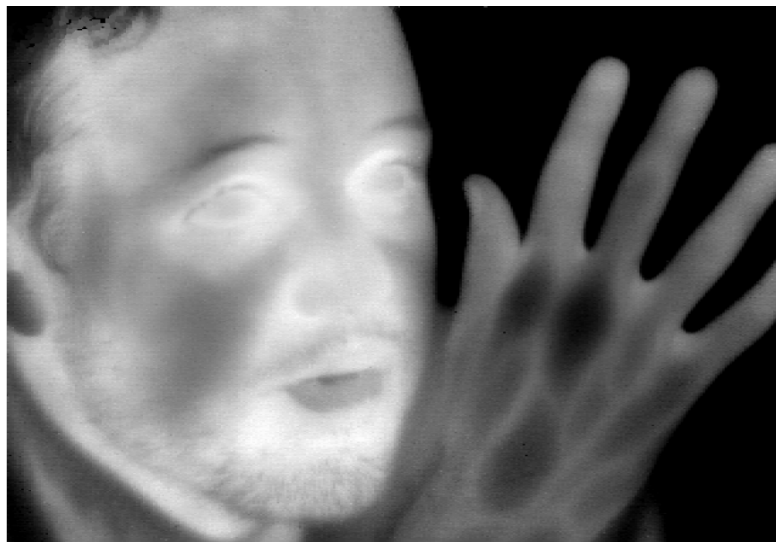


Figure 7.16 Windowed  $640 \times 448$  image of InP/InGaAs QWIP FPA at 70K with 4 ms integration time using 50 mm effective focal length lens [96].

InP/InGaAs QWIP FPA has mean NETD value approaching 40 mK at 77 K operating temperature. Figures 7.20 and 7.21 show recorded 77 K thermal images with 50 mm imaging lens. Figure 7.21 shows thermal image of a parking lot



recorded in a summer midnight. The colder regions shaded by the parked cars during the day time are clearly seen in the image.



Figure 7.17 Windowed 640x448 image of InP/InGaAs QWIP at 70K with 7.5 ms integration time using 50 mm effective focal length lens [96].



Figure 7.18 Thermal image obtained with 640x512 InP/InGaAs QWIP at 70 K with 17 ms integration time using 150 mm effective focal lens.

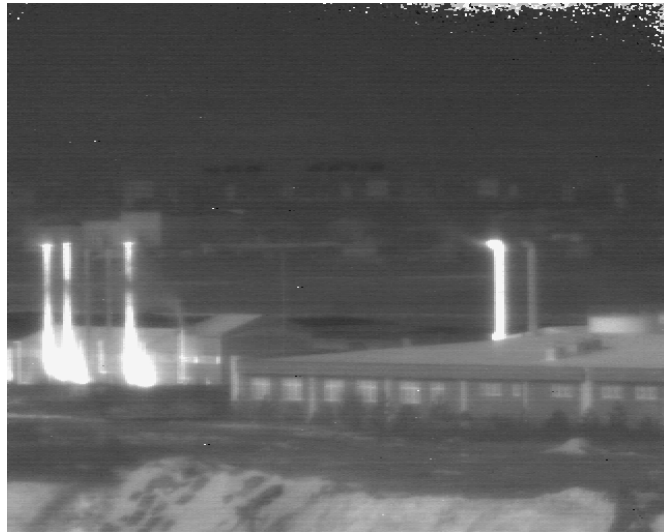


Figure 7.19 Thermal image obtained with 640x512 InP/InGaAs QWIP at 70K with 17 ms integration time using 150 mm effective focal lens.



Figure 7.20 640x512 thermal image obtained with InP/InGaAs QWIP at 77 K using 50 mm effective focal length lens [136].



Figure 7.21 Windowed 640x448 image of InP/InGaAs QWIP at 77 K using 50 mm effective focal length lens.

Figure 7.22 shows thermal image obtained with 320x256 windowed InP/InGaAsP QWIP FPA at 70K. The integration time is 12 ms, and the imaging lens has 50 mm effective focal length.



Figure 7.22 Windowed 320x256 image of InP/InGaAsP QWIP at 70 K using 50 mm effective focal length lens.

## 7.4 Conclusions

This thesis reported the MBE grown 640x512 InP/InGaAs and InP/InGaAsP QWIP FPAs, as well as a comparison of the detector characteristics with that of LWIR AlGaAs/GaAs QWIPs displaying similar spectral response. At 70 K, the InP/InGaAs and InP/InGaAsP QWIPs show background limited performance. 640x512 InP/InGaAs QWIP FPA reached 36 mK average NETD value with ~10 ms integration time at 70 K FPA temperature with peak wavelength of 7.85  $\mu\text{m}$ . 8.36  $\mu\text{m}$  peak wavelength InP/InGaAsP QWIP FPA on the other hand yielded 38 mK NETD histogram peak with ~5 ms integration time (f/1.5, 70K) on a 320x256 window of the 640x512 FPA showing potential for very large format FPAs.

Major advantage of these InP based LWIR QWIPs is that they offer high signal level together with higher system noise floor tolerance. As shown with test detector characterizations, InP based QWIPs can offer noise floor of an order of magnitude higher than AlGaAs/GaAs QWIPs, still having similar signal to noise ratio. While the characterized AlGaAs/GaAs QWIP in this study have %65 ROIC noise power level, InP based QWIPs offer %25 or lower ROIC noise power level with <40 mK NETD performance (f/1.5, 70K). These InP based FPAs can be used in high noise environment applications or with very high frame rates.

## CHAPTER 8

### CONCLUSION AND FURTHER WORK

Infrared imaging technology continuously demands improvement in device and system performance. As a contribution to these worldwide efforts, this thesis investigated details of QWIP operation, and focused on improving the performance by using alternative material systems.

In order to understand the electron transport in QWIP, a novel ensemble Monte-Carlo simulator is designed and implemented. The features of this simulator code and the most important conclusions can be summarized as :

- Capture and escape into and from quantum wells are not treated by assuming a reservoir QW model. Instead, detailed capture and escape mechanisms are simulated.  $2D \leftrightarrow 3D$  and  $2D \leftrightarrow 2D$  scattering rates are realistically evaluated.
- For technologically important AlGaAs/GaAs QWIP, quantization in L valley is considered for the first time, which guided us to discover an important capture mechanism.
- Capture paths of electrons to quantum wells are simulated in detail and dominant capture mechanisms are pointed in QWIP operation. It is discovered that at medium and high e-fields L valley QW is a trap for electrons which keeps the photoconductive gain low in AlGaAs/GaAs QWIPs as the e-field is increased.

- Electron velocity vs. e-field, and electron velocity vs. position in QWIP are investigated and the dependence of velocity to barrier material properties is explained. It is shown that negative differential change observed in photoconductive gain and inverse capture parameter is not only due to velocity effects but also due to electron lifetime, where, electron lifetime is related to capture dynamics in higher conduction band valleys in QWIP.
- It is shown that high photoconductive gain observed in InP/InGaAs and GaAs/InGaAs QWIPs is not due to good transport properties of binary barrier material but due to larger  $\Gamma$ -L valley energy separation.
- Transient response of QWIP to an infrared photoexcitation pulse is simulated with the developed MC simulator. When the response is transit time limited, it is shown that the measured photocurrent pulse width is %40 larger than the transit time estimated by dividing the device length to average barrier electron velocity.

This work on ensemble Monte-Carlo simulation of QWIPs provided invaluable information on the capture processes and electron transport in QWIPs. It is seen that changing  $\Gamma$ -L energy spacing of QWIP barrier material offer major changes in QWIP characteristics. InP/InGaAs and InP/InGaAsP material systems are used to experimentally test this conclusion and to investigate the feasibility of QWIPs using these alternative materials. These studies concluded us to the following :

- InP/InGaAs and InP/InGaAsP QWIPs offer specific detectivity values above  $10^{10}$  cm.Hz<sup>1/2</sup>/W and BLIP operation (f/2) at 70 K temperature. The responsivities of the investigated InP based LWIR QWIPs are an order of magnitude higher than the standard AlGaAs/GaAs QWIP technology. InP/InGaAs and InP/InGaAsP QWIPs operate without excess avalanche noise until 25 kV/cm, and 15 kV/cm average e-field respectively. Until set-up of carrier multiplication, InP/InGaAs QWIP offers 2.9 A/W, and InP/InGaAsP QWIP offers 1 A/W responsivity. Together with a reasonably high detectivity, the high responsivity offers higher allowable system noise

floor and higher frame rates when compared with standard AlGaAs/GaAs QWIP technology.

- Experimentally measured bias dependence of photoconductive and noise gains of the InP/InGaAs and AlGaAs/GaAs QWIPs are explained. It is concluded that device conduction band structure has strong effect on photoconductive gain, responsivity, and noise of the QWIP.
- For strategic applications requiring low temperature/low background operation, standard AlGaAs/GaAs QWIP technology has some limitations. At 40 K operation temperature, test pixels of InP/InGaAs QWIP did not show responsivity roll-off while AlGaAs/GaAs QWIP had. Under swept bias voltage, low background current of the InP/InGaAs QWIP showed smaller zero bias offset and weaker hysteresis character than that of AlGaAs/GaAs QWIP. This shows the advantage of InP based LWIR QWIPs over standard AlGaAs/GaAs QWIPs for strategic applications.

Above summarized important conclusions led the study to fabricating focal plane arrays with InP based LWIR QWIPs. In this effort 640x512 InP/InGaAs and 640x512 InP/InGaAsP QWIP FPAs are demonstrated. The following conclusions can be drawn from this work:

- InP/InGaAs QWIPs offer 36 mK average NETD value. On 640x512 format array with ~10 ms integration time at 70 K FPA temperature with peak wavelength of 7.85  $\mu\text{m}$ . 8.36  $\mu\text{m}$  peak wavelength InP/InGaAsP QWIP on the other hand yielded 38 mK NETD histogram peak with ~5 ms integration time (f/1.5, 70K) on a 320x256 window of the 640x512 FPA showing the potential of this material for very large format FPAs.
- The NETD uniformity level obtained with InP/InGaAs 640x512 FPA is %17 where corrected DC signal uniformity is %5.7 without correction and drops to the  $10^{-4}$  order after two point correction, which is at the same level with competing standard AlGaAs/GaAs QWIPs FPAs. While the reported

640x512 InP/InGaAsP QWIP FPA is 320x256 windowed, this FPA showed same level of uniformity with the InP/InGaAs FPA.

- InP based LWIR QWIP FPAs are less prone to system noise due to higher responsivity. As shown with test detector characterizations, InP based QWIPs can offer noise floor of an order of magnitude higher than AlGaAs/GaAs QWIPs, still having similar signal to noise ratio. While the characterized AlGaAs/GaAs QWIP in this study have %65 ROIC noise power level, InP based QWIPs offer %25 or lower ROIC noise power level with <40 mK NETD performance (f/1.5, 70K). For high system noise or high frame rate applications demanding large format LWIR imaging, InP based LWIR QWIPs seem to be a good choice.

Future studies complementing these results would include investigating feasibility of dual band InP based QWIPs. Dual/multi-band thermal imaging is one of the most promising application of QWIPs. Until today, only GaAs based AlGaAs/GaAs and AlGaAs/InGaAs multiband QWIP structures are investigated. GaAs substrate does not practically allow further lattice matched material combinations. Many possible lattice matched or strained material systems on InP substrate call for further research on InP based QWIPs.

Research on carrier transport in photoconductors gained remarkable improvement with the advent of QWIP. QWIP is the first photoconductor that utilizes bandgap engineering together with quantum size effects. For nearly 20 years, capture/escape of electrons at discrete quantum wells, interaction of e-field of incident photons with electron wavefunctions, and vertical transport through heterostructures have been investigated in detail with the development of QWIP technology. This wealth of information probably will not be limited only to QWIPs but will be invaluable for future's devices such as superlattice structures, carbon-nanotubes, quantum cascade photodetectors, and other kinds of nanostructures that utilize carrier transport through heterostructures.



## REFERENCES

- [1] B. F. Levine, "Quantum-well infrared photodetectors", *Journal of Applied Physics*, vol. 74, pp. R1-R81, 1993.
- [2] B. F. Levine, C. G. Bethea, K. G. Glogovsky, J. W. Stayt, R. E. Leibenguth, "Long-wavelength 128x128 GaAs quantum well infrared photodetector arrays", *Semiconductor Science and Technology*, vol. 6, pp. C114-C119, 1991.
- [3] L. J. Kozlowski, G. M. Williams, G. J. Sullivan, C. W. Farley, R. J. Anderson, J. Chen, D. T. Cheung, W. E. Tennant, R. E. DeWames, "LWIR 128x128 GaAs/AlGaAs multiple quantum well hybrid focal plane array", *IEEE Transactions on Electron Devices*, vol. 38, pp. 1124-1130, 1991.
- [4] P.N.J. Dennis, *Photodetectors*, Plenum Press, New York, 1986.
- [5] P.W. Kruse, *Uncooled Thermal Imaging*, SPIE Press, Bellingham, 2001.
- [6] H. Schneider, C. Schonbein, M. Walther, K. Schwarz, J. Fleissner, P. Koidl, "Photovoltaic quantum well infrared photodetectors: The four-zone scheme", *Applied Physics Letters*, vol. 71, pp. 246-248, 1997.
- [7] H. Schneider, M. Walther, C. Schonbein, R. Rehm, J. Fleissner, W. Pletschen, J. Braunstein, P. Koidl, G. Weimann, J. Ziegler, W. Cabanski, "QWIP FPAs for high performance thermal imaging", *Physica E*, vol. 7, pp. 101-107, 2000.
- [8] W. A. Cabanski, W. Rode, J. Wendler, J. Ziegler, J. Fleißner, F. Fuchs, R. Rehm, J. Schmitz, H. Schneider, M. Walther, "Third generation focal plane array IR detection modules and applications (Invited Paper)", *Proceedings of SPIE-Infrared Technology and Applications XXXI*, vol. 5783, pp.340-349, 2005.
- [9] Maintenance Resources, "An overview of Infrared Technology", <http://www.maintenanceresources.com/ReferenceLibrary/InfraredThermography/infraredglossary.htm>, 1 May 2006.

- [10] L. C. West, S. J. Eglash, "First observation of an extremely large-dipole infrared transition within the conduction band of a GaAs quantum well", *Applied Physics Letters*, vol. 46, pp. 1156-1158, 1984.
- [11] "Quantum Well Infrared Photodetector (QWIP) Focal Plane Arrays", edited by H. C. Liu, F. Capasso, *Semiconductors and Semimetals*, vol. 62, Academic Press, 1999.
- [12] B. F. Levine, K. K. Choi, C. G. Bethea, J. Walker, R. J. Malik, "New 10  $\mu\text{m}$  infrared detector using intersubband absorption in resonant tunneling GaAlAs superlattices", *Applied Physics Letters*, vol. 50, pp.1092-1094, 1987.
- [13] B. F. Levine, C. G. Bethea, G. Hasnain, J. Walker, R. J. Malik, "High detectivity  $D^*=1.0 \times 10^{10} \text{ cm}^2/\text{Vs}$  GaAs/AlGaAs multiquantum well  $\lambda=8.3 \mu\text{m}$  infrared detector", *Applied Physics Letters*, vol. 53, pp. 296-298, 1988.
- [14] B. F. Levine, C. G. Bethea, G. Hasnain, V. O. Shen, E. Pelve, R. R. Abbott, S. J. Hsieh, "High sensitivity low dark current 10  $\mu\text{m}$  GaAs quantum well infrared photodetectors", *Applied Physics Letters*, vol. 56, pp. 851-853, 1990.
- [15] B. F. Levine, A. Zussman, S. D. Gunapala, M. T. Asom, J. M. Kuo, and W. Hobson, "Photoexcited escape probability, optical gain, and noise in quantum well infrared photodetectors", *Journal of Applied Physics*, vol. 72, pp.4429-4443, 1992.
- [16] Brown E. R., Eglash S. J., and McIntosh K. A. 1996 *Optoelectronic Properties of Semiconductors and Superlattices* edited by Razeghi M (Amsterdam: Gordon and Breach Science Publishers), pp. 1-353.
- [17] O. O. Celtek, and C. Besikci, "Detailed investigation of electron transport, capture and gain in  $\text{Al}_{0.3}\text{Ga}_{0.7}\text{As}/\text{GaAs}$  quantum well infrared photodetectors", *Semiconductor Science and Technology*, vol. 19, pp.183-190, 2004.

- [18] S D Gunapala, B. F. Levine, L. Pfeiffer, and K. West, "Dependence of the performance of GaAs/AlGaAs quantum well infrared photodetectors on doping and bias" *Journal of Applied Physics*, vol. 69, pp.6517-6520, 1991.
- [19] K. K. Choi, B. F. Levine, R. J. Malik, J. Walker, C. G. Bethea, "Periodic negative conductance by sequential resonant tunneling through an expanding high-field superlattice domain", *Physical Review B*, vol. 35, pp. 4172-4175, 1987.
- [20] S. D. Gunapala, S. V. Bandara, J. K. Liu, E. M. Luong, N. Stetson, C. A. Shott, J. J. Bock, S. B. Rafol, J. M. Mumolo, M. J. Mckelvey, "Long-Wavelength 256 X 256 GaAs/AlGaAs Quantum Well Infrared Photodetector (QWIP) Palm-Size Camera", *IEEE Transactions on Electron Devices*, vol. 47, pp. 326-332, 2000.
- [21] H. Schneider, M. Walther, C. Schonbein, R. Rehm, J. Fleissner, W. Pletschen, J. Braunstein, P. Koidl, G. Weimann, J. Ziegler, W. Cabanski, "QWIP FPAs for high performance thermal imaging", *Physica E*, vol. 7, pp. 101-107, 2000.
- [22] W. A. Beck, "Photoconductive gain and generation-recombination noise in multiple-quantum-well infrared detectors", *Applied Physics Letters*, vol. 63, pp. 3589-3591, 1993.
- [23] H. C. Liu, "Photoconductive gain mechanism of quantum-well intersubband infrared detectors", *Applied Physics Letters*, vol. 60, pp. 1507-1509, 1992.
- [24] K.K. Choi, "Reduction of photoconductive gain in quantum well infrared photodetectors", *Journal of Applied Physics*, vol. 80, pp. 1257-1259, 1996.
- [25] H. Schneider, "Optimized performance of quantum well intersubband infrared detectors: Photovoltaic versus photovoltaic operation", *Journal of Applied Physics*, vol. 74, pp. 4789-4791, 1993.
- [26] C. Schonbein, H. Schneider, R. Rehm, M. Walther, "Noise gain and detectivity of n-type GaAs/AlAs/AlGaAs quantum well infrared photodetectors", *Applied Physics Letters*, vol. 73, pp. 1251-1253, 1998.
- [27] B. F. Levine, "Comment on ‘ Noise gain and detectivity of n-type GaAs/AlAs/AlGaAs quantum well infrared photodetectors ‘ [*Applied*

- Physics Letters* 73, 1251(1998)]", *Applied Physics Letters*, vol. 74, p. 892, 1999.
- [28] G. Sarusi, B. F. Levine, S. J. Pearton, K. M. S. Bandara, R. E. Leibenguth, "Improved performance of quantum well infrared photodetectors using random scattering optical coupling", *Applied Physics Letters*, vol. 64, pp. 960-962, 1994.
  - [29] T. R. Schimert, S. L. Barnes, A. J. Brouns, F. C. Case, P. Mitra, L. T. Claiborne, "Enhanced quantum well infrared photodetector with novel multiple quantum well grating structure", *Applied Physics Letters*, vol. 68, pp. 2846-2848, 1996.
  - [30] K. K. Choi, C. J. Chen. D. C. Tsui, "Corrugated quantum well infrared photodetectors for material characterization", *Journal of Applied Physics*, vol. 88, pp. 1612-1623, 2000.
  - [31] B. F. Levine, S. D. Gunapala, R. F. Kopf, "Photovoltaic GaAs quantum well infrared detectors at 4.2  $\mu\text{m}$ ", *Applied Physics Letters*, vol. 58, pp. 1551, 1991.
  - [32] B.F. Levine, A. Zussman, J. K. Kuo and J. de Jong, "19 $\mu\text{m}$  cutoff long-wavelength GaAs/ $\text{Al}_x\text{Ga}_{1-x}\text{As}$  quantum well infrared photodetectors", *Journal of Applied Physics*, vol. 71, pp. 5130-5135, 1992.
  - [33] M. Z. Tidrow, X. Jiang, S. S. Li, K. Bacher, "A four-color quantum well infrared photodetector", *Applied Physics Letters*, vol. 74, pp.1335-1337, 1999.
  - [34] K. K. Choi, S. V. Bandara, S. D. Gunapala, W. K. Liu, J. M. Fastenau, "Detection wavelength of InGaAs/AlGaAs quantum wells and superlattices", *Journal of Applied Physics*, vol. 91, pp. 551-564, 2002.
  - [35] M. Sundaram, S. C. Wang, M. F. Taylor, A. Reisinger, G. L. Milne, K. B. Reiff, R. E. Rose, R. R. Martin, "Two-color quantum well infrared photodetector focal plane arrays", *Infrared Physics and Technology*, vol. 42, pp. 301-308, 2001.
  - [36] S. M. Sze, "Physics semiconductor devices", John Wiley & Sons, 1981.

- [37] S. D. Gunapala, K. M. S. V. Bandara, "Very long wavelength  $\text{In}_x\text{Ga}_{1-x}\text{As}/\text{GaAs}$  quantum well infrared photodetectors", *Applied Physics Letters*, vol. 64, pp. 2288-2290, 1994.
- [38] S. D. Gunapala, B.F. Levine, R. A. Logan, T. Tanbun-Ek, D. A. Humphrey, "GaAs/GaInP multiquantum well long-wavelength infrared detector using bound-to-continuum state absorption", *Applied Physics Letters*, vol. 57, pp.1802-1804, 1990.
- [39] S. D. Gunapala, B. F. Levine, D. Ritter, R. Hamm, and M. B. Panish, "InGaAs/InP long wavelength quantum well infrared photodetectors", *Applied Physics Letters*, vol. 58, pp. 2024-2026, 1991.
- [40] M. O. Watanabe, Y. Ohba, "Interface properties for GaAs/InGaAlP heterojunctions by capacitance voltage profiling technique", *Applied Physics Letters*, vol. 50, pp. 906-908, 1987.
- [41] S. D. Gunapala, J. K. Liu, J. S. Park, M. Sundaram, C. A. Shott, T. Hoelter, T. Lin, S. T. Massie, P. D. Maker, R. E. Muller, and G. Sarusi, "9- $\mu\text{m}$  cutoff 256x256 GaAs/ $\text{Al}_x\text{Ga}_{1-x}\text{As}$  quantum well infrared photodetector handheld camera", *IEEE Transactions on Electron Devices*, vol. 44, pp. 51-57, 1997.
- [42] A. Goldberg, T. Fischer, S. Kennerly, W. Beck, V. Ramirez, K. Garner, "Laboratory and field imaging test results on single-color and dual-band QWIP focal plane arrays", *Infrared Phys. and Tech.*, vol. 42, pp. 309-321, 2001.
- [43] D. Sengupta, V. Jandhyala, S. Kim, W. Fang, J. Malin, P. Apostolakis, K.C. Hsieh, Y. C. Chang, S. L. Chuang, S. Bandara, S. Gunapala, M. Feng, E. Michielssen, and G. Stillman, "Redshifting and Broadening of Quantum-Well Infrared Photodetector's Response via Impurity-Free Vacancy Disorder", *IEEE J. of Selected Topics in Quantum Electronics*, vol. 4, pp. 746-757, 1998.
- [44] A. Manissadjian, P. Tribolet, P. Chorier, P. Costa, "Sofradir infrared detector products: the past and future", *Proceedings of SPIE-Infrared Technology and Applications XXVI*, vol. 4130, pp.480-495, 2000.

- [45] AIM Infrared Module GmbH, "Products and Services", <http://www.aim-ir.de/pages/products/?lan=en>, 1 May 2006.
- [46] QWIP Technologies Inc. , "Products", <http://www.qwip.com>, 1 May 2006.
- [47] E. Costard, Ph. Bois, X. Marcadet, A. Nedelcu, "QWIP Products and Building Blocks for High Performance Imaging Systems", *Proceedings of SPIE-Infrared Technology and Applications XXX*, vol. 5406, pp. 646-653, 2004.
- [48] A. Rogalski, "Quantum well infrared photoconductors in infrared photodetector technology", *Journal of Applied Physics*, vol. 93, pp. 4355-4391, 2003.
- [49] R. Rawe, A. Timlin, M. Davis, J. Devitt, M Greiner, "Advanced large format InSb IR FPA maturation at CMC Electronics", *Proceedings of SPIE-Infrared Technology and Applications XXX* , vol. 5406, pp. 152-162, 2004.
- [50] S. D. Gunapala, S. V. Bandara, J. K. Liu, S. B. Rafol, C. Hill, J. Mumolo, J. Thang, M. Tidrow, and P. D. LeVan, "Mid-wavelength infrared 1024x1024 pixel QWIP focal plane array", *Proceedings of SPIE-Infrared Technology and Applications XXX*, vol. 5406, pp. 600-604, 2004.
- [51] J. Little, S. Svensson, A. Goldberg, S. K. T. Hongsmatip, M. Winn, P. Uppal, K. Olver, "Type II superlattice infrared focal plane arrays: Optical, electrical, and mid-wave infrared imaging characterization" 2006 APS March Meeting, 2006.
- [52] C. A. Kukkonen, M. Levy, P. LeVan, and M. A. Fauci, "Quantum well infrared photodetector research and development at Jet Propulsion Laboratory", *Infrared Physics and Technology*, vol. 42, pp. 267-282, 2001.
- [53] J. L. Tissot , "Advanced IR detector technology development at CEA/LETI", *Infrared Phys. and Tech.*, vol. 43, pp. 223-228, 2002.
- [54] R. D. Rajavel, *et. al.* , "High performance HgCdTe two-color infrared detectors grown by molecular beam epitaxy", *Journal of Crystal Growth*, vol. 175-176, pp.653-658, 1997.
- [55] Photonics.com, "1998 Photonics Applications Handbook", p. H-153, <http://www.photonics.com/directory/hb/index.asp>, 1 May 2006

- [56] W. L. Wolfe, "Infrared System Design (SPIE Tutorial Texts in Optical Engineering vol. TT24.)", SPIE Press, 1996.
- [57] M. Tepegöz, "A 64x64 CMOS Integrated Readout Circuit for Infrared Photodetector Focal Plane Arrays", M.S. Thesis, Middle East Technical University, August 2003.
- [58] J. F. Johnson, "Direct Injection Readout Circuit Model", *Proceedings of SPIE - Infrared Readout Electronics II*, vol. 2226, pp. 120-129, 1994.
- [59] R.F. Cannata, "Design and analysis of IR Readout Integrated Circuits", *SPIE Short Course Lecture Notes*, 2000.
- [60] C. C. Hsieh, C. Y. Wu, F. W. Jih, T. P. Sun, "Focal Plane Arrays and CMOS Readout Techniques for Infrared Imaging Systems", *IEEE Transactions on Circuits and Systems for Video Technology*, vol. 7, pp. 594-605, 1997.
- [61] Rockwell Scientific, "Rockwell Scientific", <http://www.rockwellscientific.com>, 1 May 2006
- [62] N. Yoon, B. Kim, H. C. Lee, and C. K. Kim, "High injection efficiency readout circuit for low resistance infra-red detector" *Electronics Letters*, vol. 35, pp. 1507-1508, 1999
- [63] H. Kulah and T. Akin "A Current Mirroring Integration Based Readout Circuit for High Performance Infrared FPA Applications" *IEEE Transactions on Circuits and Systems*, vol. 50, pp. 181-186, 2003
- [64] P. Bois, E. Costard, X. Marcadet, E. Herniou, "Development of Quantum Well Infrared Photodetectors in France", *Infrared Physics and Technology*, pp. 291-300, 2001.
- [65] R. Westervelt, H. Abarbanel, R. Garwin, R. Jeanloz, J. Kimble, J. Sullivan, E. Williams, "Imaging Infrared Detectors II", The Mitre Corporation, Virginia, 2000.
- [66] G.C. Holst, "Testing and Evaluation of Infrared Imaging Systems", SPIE Optical Engineering Press, Bellingham, 1998.
- [67] G.C. Holst, "Electro-Optical Imaging System Performance", 4<sup>th</sup> Ed., SPIE Optical Engineering Press, Bellingham, 2005.

- [68] J. L. Pan, C. G. Fonstad, "Physical model of depletion and accumulation in quantum well infrared photodetectors", *IEEE Journal of Quantum Electronics*, vol. 35, p. 1673-1684, 1999.
- [69] V. Ryzhii, "Characteristics of quantum well infrared photodetectors", *Journal of Applied Physics*, vol. 81, pp. 6442-6448, 1997.
- [70] K. K. Choi, "Detection wavelength of quantum-well infrared photodetectors", *Journal of Applied Physics*, vol. 73, p. 5230-5236, 1993.
- [71] Artaki and Kizilyalli, "Quantum well infrared photodetectors: Monte Carlo simulations of transport", *Applied Physics Letters*, vol. 58, p. 2467-2469, 1991.
- [72] L. Thibaudau, P. Bois and J. Y. Duboz , "A self-consistent model for quantum well infrared photodetectors", *Journal of Applied Physics*, vol. 79, pp. 446-454, 1996.
- [73] M. Ershov, V. Ryzhii, C. Hamaguchi, "Contact and distributed effects in quantum well infrared photodetectors", *Applied Physics Letters*, vol. 67, pp. 3147-3149, 1995.
- [74] M. Ershov, "Transient photoconductivity in quantum well infrared photodetectors", *Applied Physics Letters*, vol. 69, pp. 3480-3482, 1996.
- [75] M. Ershov, H. C. Liu, L. Li, M. Buchanan., Z. R. Wasilewski, V. Ryzhii, "Unusual capacitance behavior of quantum well infrared photodetectors", *Applied Physics Letters*, vol. 70, pp. 1828-1830, 1997.
- [76] M. Ryzhii, V. Ryzhii, "Monte Carlo Modeling of Transient Recharging Processes in Quantum-Well Infrared Photodetectors", *IEEE Transactions on Electron Devices*, vol. 47, pp. 1935-1942, 2000.
- [77] M. Ryzhii, V. Ryzhii, "Monte Carlo analysis of ultrafast electron transport in quantum well infrared photodetectors", *Applied Physics Letters*, vol. 72, pp. 842-844, 1998.
- [78] M. Ryzhii, I. Khmyrova, V. Ryzhii, "Influence of electron velocity overshoot effect on high-frequency characteristics of quantum well infrared photodetectors", *Japanese Journal of Applied Physics*, vol. 37, pp. 78-83, 1998.



- [79] M. Ryzhii, V. Ryzhii, M. Willander, "Monte Carlo modeling of electron velocity overshoot effect in quantum well infrared photodetectors", *Journal of Applied Physics*, vol. 84, pp. 3403-3408, 1998.
- [80] M. Ryzhii, V. Ryzhii, "Monte Carlo Modeling of Electron Transport and capture processes in AlGaAs/GaAs Multiple Quantum Well Infrared Photodetectors", *Japanese Journal of Applied Physics*, vol. 38., pp. 5922-5927, 1999.
- [81] S. Adachi, "GaAs, AlAs, and  $\text{Al}_x\text{Ga}_{1-x}\text{As}$  Material Parameters for use in research and device applications", *Journal of Applied Physics*, vol. 58, p. R1-R29, 1985.
- [82] I. Vurgaftman, J. R. Meyer, L. R. Ram-Mohan, "Band-parameters for III-V compound semiconductors and their alloys", *Journal of Applied Physics*, vol. 89, pp. 5815-5875, 2001.
- [83] K. Tomizawa, "Numerical simulation of submicron semiconductor devices", Norwood: Artech House, 1993.
- [84] R.W. Hockney and J. W. Eastwood, "*Computer Simulation Using Particles*", Bristol and New York: Adam Hilger, 1988.
- [85] A. T. Bakir, "Advanced Monte Carlo Modeling of III-V Field-Effect Transistors", M.S. Thesis, Middle East Technical University, 1999.
- [86] R. L. Liboff, "Introductory quantum mechanics", Addison Wesley Longman, 1997.
- [87] S. M. Sze, "Physics of Semiconductor Devices", John Wiley & Sons, 1981.
- [88] E. Öncü, "Detailed investigation of bound to quasibound quantum well infrared photodetectors : An advanced Monte Carlo study," M.S. Thesis, Middle East Technical University, 1999.
- [89] S. Özer, "Performance Assessment of Pseudomorphic MODFETs Through Monte Carlo Simulations", *M.S. Thesis*, Middle East Technical University, 2000.
- [90] M. A. Khalil M. Goano, A. Champagne, and R. Maciejko, "Capture and escape in quantum wells scattering events in Monte Carlo simulation", *IEEE Photonics Technology Letters*, vol. 8, pp. 19-21, 1996.

- [91] J. L. Educato, J. P. Leburton, J. Wang, D. W. Bailey, "Intervalley shunting of electrons in modulation-doped multiple-quantum-well structures" *Physical Review B*, vol. 44, pp. 8365-8368, 1991.
- [92] C. Besikci, A. T. Bakir and B. Tanatar, "Dielectric Screening Effects on Electron Transport in  $\text{Ga}_{0.51}\text{In}_{0.49}\text{P}/\text{In}_x\text{Ga}_{1-x}\text{As}/\text{GaAs}$  Quantum Wells", *Journal of Applied Physics*, vol. 88, pp.1504-1510, 2000.
- [93] S. M. Goodnick, P. Lugli, "Effect of electron-electron scattering on nonequilibrium transport in quantum-well systems" *Physical Review B*, vol. 37, pp. 2578-2588 , 1988.
- [94] Gunapala, B. F. Levine, D. Ritter, R. Hamm, and M. B. Panish, "InGaAs/InP long wavelength quantum well infrared photodetectors", *Applied Physics Letters*, vol. 58, pp. 2024-2026, 1991.
- [95] O. O. Cellek, S. Memis, U. Bostanci, S. Ozer, C. Besikci, "Gain and transient photoresponse of quantum well infrared photodetectors: a detailed ensemble Monte Carlo study", *Physica E*, vol. 24, pp. 318-327, 2004.
- [96] O. O. Cellek, S. Ozer, C. Besikci, "High Responsivity InP-InGaAs Quantum-Well Infrared Photodetectors: Characteristics and Focal Plane Array Performance", *IEEE Journal of Quantum Electronics*, vol.41, pp. 980-985, 2005.
- [97] H. Schneider, C. Mermelstein, R. Rehm, C. Schonbein, A. Sa'ar, M. Walther , "Optically induced electric-field domains by bound-to-continuum transitions in n-type multiple quantum wells", *Physical Review B*, vol. 57, p. R15096-15099, 1998.
- [98] M. Ryzhii and V. Ryzhii, "Monte Carlo modeling of electron transport and capture processes in AlGaAs/GaAs multiple quantum-well infrared photodetectors", *Physica E*, vol. 7, p. 120-123, 2000.
- [99] C. Jelen, S. Slivken, T. David, M. Razeghi, G. Brown, "Noise performance of InGaAs-InP quantum-well infrared photodetectors", *IEEE Journal of Quantum Electronics*, vol 34, pp. 1124-1128 , 1998.
- [100] S. D. Gunapala, K. M. S. V. Bandara, B. F. Levine, G. Sarusi, J. S. Park, T. L. Lin, W. T. Pike, and K. K. Liu, "High performance InGaAs/GaAs

- quantum well infrared photodetectors", *Applied Physics Letters*, vol. 64, pp. 3431-3433, 1994.
- [101] M. J. Kane, S. Millidge, M. T. Emeny, D. R. P. Guy, D. Lee and C. R. Whitehouse, "Electron mobilities and photoelectron lifetimes in AlGaAs/GaAs and InGaAs/GaAs quantum-well infrared detectors" *Journal of Applied Physics*, vol.73, pp. 7966-7968, 1993.
  - [102] G. Sarusi, S. D. Gunapala, J. S. Park, B. F. Levine, "Design and performance of very long-wavelength GaAs/Al<sub>x</sub>Ga<sub>1-x</sub>As quantum well infrared photodetectors", *Journal of Applied Physics*, vol. 76, pp. 6001-6008, 1994.
  - [103] R. Rehm, H. Schneider, M. Walther, P. Koidl, "Influence of the recharging process on the dark current noise in quantum-well infrared photodetectors", *Applied Physics Letters*, vol. 80, pp. 862-864, 2002.
  - [104] R. Rehm, H. Schneider, K. Schwarz, M. Walther, P. Koidl, G. Weimann, "Responsivity and gain of InGaAs/GaAs-QWIPs and GaAs/AlGaAs-QWIPs: A comparative study", *Proceedings of SPIE-Photodetectors: Materials and Devices VI*, vol. 4288, pp. 379-385, 2001.
  - [105] S. Ehret, H. Schneider, J. Fleissner, P. Koidl, G. Bohm, "Ultrafast intersubband photocurrent response in quantum well infrared photodetectors", *Applied Physics Letters*, vol. 71, pp. 641-643, 1997.
  - [106] M. Ershov, "Non-equilibrium high frequency noise and responsivity in quantum well infrared photodetectors", *Journal of Applied Physics*, vol. 89, pp. 6253-6259, 2001.
  - [107] M. Ershov, S. Satou, Y. Ikebe, "Analytical model of transient photoresponse of quantum well infrared photodetectors", *Journal of Applied Physics*, vol. 86, pp. 6442-6450, 1999.
  - [108] S. Steinkogler, H. Schneider, R. Rehm, M. Walther, P. Koidl, "Electron transport studies on In<sub>0.3</sub>Ga<sub>0.7</sub>As/GaAs quantum well infrared photodetectors using time-resolved photocurrent measurements", *Applied Physics Letters*, vol. 81, pp. 3401-3403, 2001.

- [109] V. Ryzhii, I. Khmyrova, M. Ryzhii, “Impact of transit-time and capture effects on high-frequency performance of multiple quantum-well infrared photodetectors”, *IEEE Transactions on Electron Devices*, vol. 45, pp. 293-298, 1998.
- [110] V. Letov, M. Ershov, S.G. Matsik, A.G.U. Perera, H.C. Liu, Z.R. Wasilewski, M. Buchanan, “Transient photocurrent overshoot in quantum well infrared photodetectors”, *Applied Physics Letters*, vol. 79, pp. 2094-2096, 2001.
- [111] Fathimulla A., Hier H., Aina L., “InP-based Multi-Wavelength QWIP Technology”, *Proceedings of SPIE-Infrared Technology and Applications XXX*, vol. 5406, pp. 589-599, 2004.
- [112] J. Y. Andersson, L. Lundqvist, Z. F. Paska, K. Streubel, and J. Wallin, “Long-wavelength quantum-well infrared detectors based on intersubband transitions in InGaAs/InP quantum wells”, *Proceedings of SPIE-Infrared Technology XVIII*, vol. 1762, pp. 216–226, 1992.
- [113] D. K. Sengupta, S. L. Jackson, A. P. Curtis, W. Fang, J. I. Malin, T. U. Horton, Q. Hartman, H. C. Kuo, S. Thomas, J. Miller, K. C. Hsieh, I. Adesida, S. L. Chuang, M. Feng, G. E. Stillman, Y. C. Chang, W. Wu, J. Tucker, H. Chen, J. M. Gibson, J. Mazumder, L. Li, and H. C. Liu, “Growth and characterization of n-type InP/InGaAs quantum well infrared photodetectors for response at 8.93  $\mu\text{m}$ ,” *Journal of Electronic Materials*, vol. 26, pp. 1376–1381, 1997.
- [114] H. C. Liu, C. Song, E. Dupont, P. Poole, P. H. Wilson, B. J. Robinson, and D. A. Thompson, “Near and middle infrared dual band operation of InGaAs/InP quantum well infrared photodetector,” *Electronics Letters*, vol. 35, pp. 2055–2056, 1999.
- [115] J. Jiang, C. Jelen, M. Razeghi, and G. J. Brown, “High detectivity GaInAs-InP quantum-well infrared photodetectors grown on Si substrates,” *IEEE Photonics Technology Letters*, vol. 14, pp. 372–374, 2002.
- [116] B. Aslan, H. C. Liu, A. Bezinger, P. J. Poole, M. Buchanan, R. Rehm, and H. Schneider, “High responsivity, dual-band response and intraband

- avalanche multiplication in InGaAs/InP quantum well photodetectors” *Semiconductor Science and Technology*, vol. 19, pp. 442–445, 2004.
- [117] Jiang, K. Mi, R. McClintock, M. Razeghi, G. J. Brown, and C. Jelen, “Demonstration of 256\_256 focal plane array based on Al-Free GaInAs-InP QWIP,” *IEEE Photonics Technology Letters*, vol. 15, pp. 1273–1275, Sep. 2003.
  - [118] Y. Gusakov, E. Finkman, G. Bahir, and D. Ritter, “The effect of strain in InP/InGaAs quantum-well infrared photodetectors on the operating wavelength,” *Applied Physics Letters*, vol. 79, pp. 2508–2510, 2001.
  - [119] S. D. Gunapala, B. F. Levine, D. Ritter, R. Hamm, and M. B. Panish, “Lattice-matched InGaAsP/InP long-wavelength quantum well infrared photodetectors,” *Applied Physics Letters*, vol. 60, pp. 636–638, 1992.
  - [120] Hasnain G., Levine B.F., Sivco D.L., Cho A.Y., “Mid-infrared detectors in the 3-5  $\mu\text{m}$  band using bound to continuum state absorption in InGaAs/InAlAs multiquantum well structures”, *Applied Physics Letters*, vol. 56, pp.770-772, 1990.
  - [121] Levine B.F., Gunapala S.D., Kopf R.D., “Photovoltaic GaAs quantum well infrared photodetectors at 4.2  $\mu\text{m}$  using indirect  $\text{Al}_x\text{Ga}_{1-x}$  barriers”, *Applied Physics Letters*, vol.58, pp. 1551-1553, 1991.
  - [122] K. Saxena, *Journal of Physics C*, 13, pp. 4323-4334, 1980.
  - [123] H. C. Liu, M. Buchanan, and Z. R. Wasilewski, “Short wavelength (1-4  $\mu\text{m}$ ) infrared detectors using intersubband transitions in GaAs-based quantum wells”, *Journal of Applied Physics*, vol. 83, pp. 6178-6181, 1998
  - [124] M.Z. Tidrow, “Three-well one and two-color quantum well infrared photodetectors”, *Materials Chemistry and Physics*, vol. 50, pp. 183-187, 1997.
  - [125] B. F. Levine, A. Y. Cho, J. Walker, R. J. Malik, D. A. Kleinman, D. L. Sivco, “InGaAs/InAlAs multiquantum well intersubband absorption at a wavelength of  $\lambda=4.4 \mu\text{m}$ ”, *Applied Physics Letters*, vol. 52, pp. 1481-1483, 1988.

- [126] H. Schneider, "Theory of avalanche multiplication and excess noise in quantum-well infrared photodetectors", *Applied Physics Letters*, vol. 82, pp. 4376–4378, 2003.
- [127] R. Rehm, H. Schneider, M. Walther, P. Koidl, and G. Weimann, "Avalanche multiplication due to impact ionization in quantum-well infrared photodetectors: A quantitative approach," *Applied Physics Letters*, vol. 82, pp. 2907–2909, 2003.
- [128] S.V. Bandara, S.D. Gunapala, J.K. Liu, E. M. Luong, J.M. Mumolo, W. Hong, D.K. Sengupta, and M.J. McKelvey, "10-16  $\mu\text{m}$  Broadband quantum well infrared photodetector", *Applied Physics Letters*, vol. 72, pp. 2427-2429, 1998
- [129] K.K. Choi, S.W. Kennerly, J. Yao, and D.C Tsui, "Characteristics of QWIPs at low background", *Infrared Physics and Technology*, vol. 42, pp. 221-235, 2001.
- [130] A. Singh, D. A. Cardimona, "Zero-bias offsets in the low-temperature dark current of quantum well infrared photodetectors", *Optical Engineering*, vol. 38, pp. 1424-1432, 1999.
- [131] D. A. Cardimona, A. Singh, D. Huang, C. Morath, and P. Varangis, "Time-dependent effects in QWIPs in low temperature, low background conditions", *Infrared Phys. and Tech.*, vol. 42, pp. 211-219, 2001.
- [132] J. E. Hubbs, D. C. Arrington, M. E. Gramer, and G. A. Dole, "Nonlinear response of quantum well infrared photodetectors under low-background and low-temperature conditions", *Optical Engineering*, vol. 39, pp. 2660-2671, 2000
- [133] S. Ozer, "InSb and InAsSb Infrared Photodiodes on Alternative Substrates and InP/InGaAs Quantum Well Infrared Photodetectors: Pixel And Focal Plane Array Performance", Ph.D. Thesis, Middle East Technical University, Ankara, 2005.
- [134] FLIR Systems Inc., "Products", <http://www.indigosystems.com/products/products.html>, 1 May 2006

- [135] E. Costard, P. Bois, A. D. Rossi, A. Nedelcu, O. Cocle, F. H. Gauthier, and F. Audier, “QWIP detectors and thermal imagers” *C. R. Physique*, vol. 4, pp. 1089–1102, 2003.
- [136] S. Ozer, O. O. Cellek, and C. Besikci, “Assessment of large format InP/InGaAs quantum well infrared photodetector focal plane array”, *Infrared Physics & Technology*, vol. 47, pp. 115-118, 2005.
- [137] Ioffe Physico Technical Institute, “Semiconductors”, <http://www.ioffe.rssi.ru/SVA/NSM/Semicond>, 1 May 2006.

## APPENDIX A

### MATERIAL PARAMETERS

The following material parameters were used for GaAs well, and  $\text{Al}_{0.3}\text{Ga}_{0.7}\text{As}$  and  $\text{Al}_{0.15}\text{Ga}_{0.85}\text{As}$  barrier materials. The material parameters were compiled from various resources [70,81-82]

Table A.1 Material parameters for GaAs,  $\text{Al}_{0.3}\text{Ga}_{0.7}\text{As}$ , and  $\text{Al}_{0.15}\text{Ga}_{0.85}\text{As}$ .

Description	GaAs	$\text{Al}_{0.3}\text{Ga}_{0.7}\text{As}$	$\text{Al}_{0.15}\text{Ga}_{0.85}\text{As}$
Mass density ( $\text{kg/m}^3$ )	5360	4880	5.12
Low frequency relative permittivity	12.9	12.24	12.7
High frequency relative permittivity	10.92	10.01	10.5
Acoustic wave velocity (m/sec)	5240		
Longitudinal Optical Phonon Energy (eV)	0.03536	0.0381	0.0362
Electron affinity (eV)	4.07		
Effective mass ratio in $\Gamma$ valley	0.0670	0.0847	0.0759



Effective mass ratio in L valley	0.222	0.230	0.226
Effective mass ratio in X valley	0.580	0.422	0.501
<b>Description</b>	<b>GaAs</b>	<b>Al<sub>0.3</sub>Ga<sub>0.7</sub>As</b>	<b>Al<sub>0.15</sub>Ga<sub>0.85</sub>As</b>
Nonparabolicity factor of $\Gamma$ valley (1/eV)	0.610	0.554	0.582
Nonparabolicity factor of L valley (1/eV)	0.461	0.614	0.537
Nonparabolicity factor of X valley (1/eV)	0.204	0.317	0.261
Intervalley Deformation from $\Gamma$ to $\Gamma$ (eV/cm)	0	0	0
Intervalley Deformation from $\Gamma$ to L (eV/cm)	1E9	1E9	1E9
Intervalley Deformation from $\Gamma$ to X (eV/cm)	1E9	1E9	1E9
Intervalley Deformation from L to L (eV/cm)	1E9	1E9	1E9
Intervalley Deformation from L to X (eV/cm)	5E8	5E8	5E9
Intervalley Deformation from X to X (eV/cm)	7E8	7E8	7E9
Intervalley phonon energy from $\Gamma$ to $\Gamma$ (eV)	0	0	0
Intervalley phonon energy from $\Gamma$ to L (eV)	0.0278	0.0278	0.0278
Intervalley phonon energy from $\Gamma$ to X (eV)	0.0299	0.0299	0.0299
Intervalley phonon energy from L to L (eV)	0.0290	0.0290	0.0290
Intervalley phonon energy from L to X (eV)	0.0293	0.0293	0.0293

Intervalley phonon energy from X to X (eV)	0.0299	0.0299	0.0299
Acoustic deformation potential in $\Gamma$ valley (eV)	7	7.3	7.15
Acoustic deformation potential in L valley (eV)	9.2	8.84	9.02
<b>Description</b>	<b>GaAs</b>	<b>Al<sub>0.3</sub>Ga<sub>0.7</sub>As</b>	<b>Al<sub>0.15</sub>Ga<sub>0.85</sub>As</b>
Acoustic deformation potential in X valley (eV)	9.27	8.89	9.08
Number of equivalent valleys in $\Gamma$	1	1	1
Number of equivalent valleys in L	4	4	4
Number of equivalent valleys in X	3	3	3
L to $\Gamma$ valley energy separation (eV)	0.29	0.128	0.193
X to $\Gamma$ valley energy separation (eV)	0.48	0.161	0.311
CL		5.65E-8	5.65E-8
Alloy Deformation Potential (eV)		0.49	0.49

E-k plot of bulk GaAs is given in Figure A.1. AlGaAs is also a direct bandgap semiconductor at Al mole fractions used in this simulation.

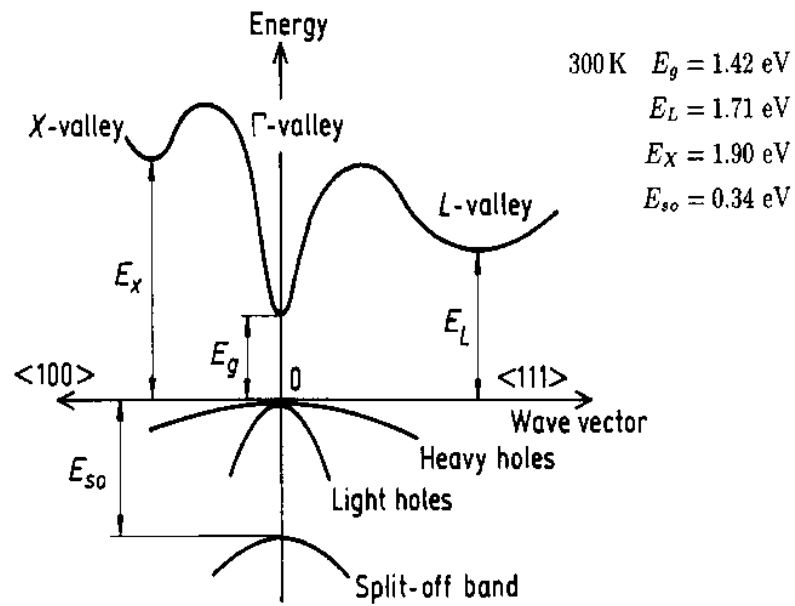


Figure A.1 E-k plot of GaAs at 300K [137]

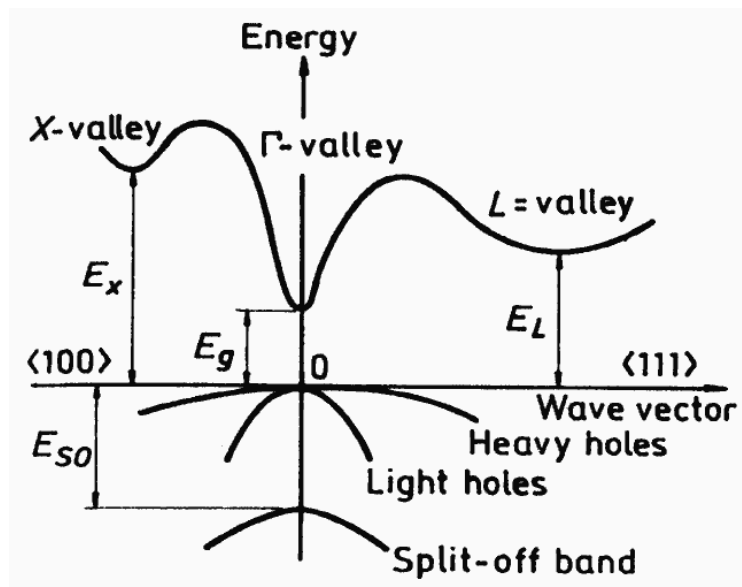


Figure A.2: Typical E-k plot of  $\text{Al}_x\text{Ga}_{1-x}\text{As}$  ( $x < 0.41$ ) at 300K [137].

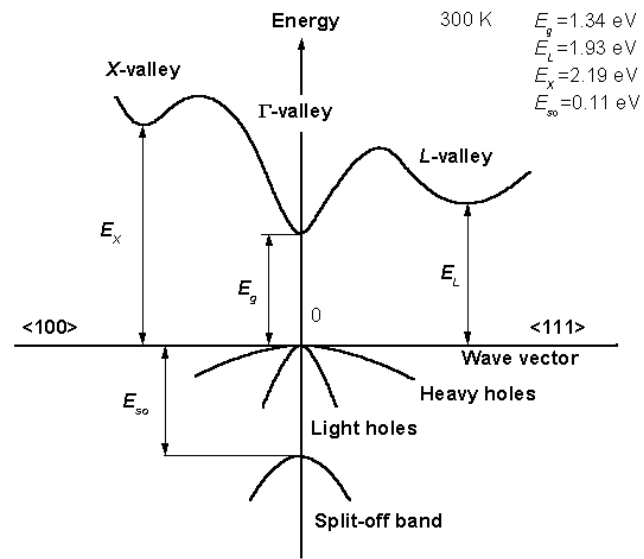


Figure A.3: E-k plot of InP at 300K [137].

## APPENDIX B

### SOLUTION OF POISSON'S EQUATION

The potential distribution in the device is found by numerically solving the Poisson's equation in 1D. The equation is given as

$$\frac{d^2}{dz^2} U = -\frac{q}{\varepsilon h_z} (Nds - ns) \quad (\text{B.1})$$

where  $U$  is the electrostatic potential,  $Nds$  is the sheet density of the related mesh, and  $h_z$  is the mesh length in  $z$  dimension. After discretization, Poisson's equation can be written as

$$\frac{U_{i-1} - 2U_i + U_{i+1}}{h_z^2} = -\frac{q}{\varepsilon h_z} (Nds - ns(i)) \quad (\text{B.2})$$

where  $ns(i)$  stands for sheet electron density of mesh  $i$ , which is found by the Cloud in the Cell (CIC) method [55]. In CIC method, each particle is assumed to have a cell like shape. During the simulation according to the position of the particle, its charge is shared with the surrounding mesh cells. This is illustrated in Figure B.1.

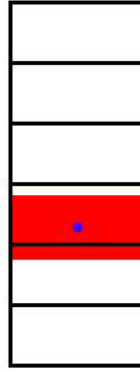


Figure B.1 Illustration of the CIC method.

After finding the potential distribution from Poisson's equation, electric field can be found by solving the equation

$$E = -\nabla U \quad (\text{B.3})$$

## APPENDIX C

### SCATTERING RATES

This Appendix describes the calculation of the 3D and 2D scattering rates used in the QWIP ensemble Monte Carlo simulations [56,59,60].

#### C.1.1 3D Polar Optical Phonon Scattering Rates

The polar optical phonon scattering rate is given by

$$\frac{1}{\tau_{pop}} = \frac{q^2 \left(\frac{1}{2m^*}\right)^{\frac{1}{2}} \omega_0}{4\pi\epsilon\hbar} \left( \frac{1}{\epsilon_{inf}} - \frac{1}{\epsilon} \right) \frac{1+2\alpha E'}{\gamma^{\frac{1}{2}}(E)} F_0(E, E_0) \left( N_0 + \frac{1}{2} \pm \frac{1}{2} \right) \quad (C.1)$$

$$N_0 = \frac{1}{e^{\frac{\hbar\omega_0}{k_B T}} - 1} \quad (C.2)$$

$$F_0(E, E') = \frac{1}{C} \left[ A \ln \left| \frac{\gamma^{\frac{1}{2}}(E) + \gamma^{\frac{1}{2}}(E')}{\gamma^{\frac{1}{2}}(E) - \gamma^{\frac{1}{2}}(E')} \right| + B \right] \quad (C.3)$$

$$A = [2(1 + \alpha E)(1 + \alpha E') + \alpha(\gamma(E) + \gamma(E'))]^2 \quad (C.4)$$

$$B = -\alpha\gamma^{1/2}(E)\gamma^{1/2}(E')[4(1 + \alpha E)(1 + \alpha E') + \alpha(\gamma(E)\gamma(E'))] \quad (C.5)$$

$$C = 4(1 + \alpha E)(1 + \alpha E') + (1 + 2\alpha E)(1 + 2\alpha E') \quad (C.6)$$

After scattering, the electron energy is,

$$E' = E \pm \hbar\omega_0 \quad (C.7)$$

$$\frac{\hbar^2 k^2}{2m_n^*} = E(1 + \alpha_n E) \equiv \gamma(E) \quad (C.8)$$

where  $\omega_0$  is the optical phonon frequency and + and – refer to absorption and emission, respectively.

The polar optical phonon scattering is not isotropic. Therefore, the angle  $\beta$  between the old  $k$  vektor, and the new  $k'$  vector after a scattering event is found from

$$\cos(\beta) = \frac{1 + f - (1 + 2f)^{r_n}}{f} \quad (C.9)$$

$$f = \frac{2\sqrt{EE'}}{(\sqrt{E} - \sqrt{E'})^2} \quad (C.10)$$

where  $r_n$  is a uniformly distributed random number between 0 and 1.



## C.2 Acoustic Phonon Scattering Rate

The acoustic phonon scattering rate is given as

$$\frac{1}{\tau_{NAP}} = \frac{(2m^*)^{\frac{3}{2}} D_a^2 k_B T}{2\pi\rho v_s^2 \hbar^4} \gamma^{\frac{1}{2}}(E)(1+2\alpha E) \left[ \frac{(1+2\alpha E)^2 + \frac{1}{3}(\alpha E)^2}{(1+\alpha E)^2} \right] \quad (C.11)$$

where  $v_s$  is the sound velocity in the crystal and  $D_a$  is the acoustic deformation potential.

The angle  $\beta$  is calculated from

$$\cos(\beta) = \frac{\left[ (1+2\alpha E)^3 (1-r_n) + r_n \right]^{\frac{1}{3}} - (1+\alpha E)}{\alpha E} \quad (C.12)$$

This scattering mechanism is treated as an elastic process.

## C.3 3D Ionized Impurity Scattering Rate

The ionized impurity scattering rate and the angle  $\beta$  are given as

$$\frac{1}{\tau_{ION}} = \frac{N_I q^4}{32\pi\sqrt{2m^*} \varepsilon^2} \frac{1}{C(k)(1+C(k))} \frac{1+2\alpha E}{E^{3/2} (1+\alpha E)^{3/2}} \quad (C.13)$$

$$\cos(\beta) = 1 + \frac{2(r_n - 1)}{1 + \frac{r_n}{C(k)}} \quad (\text{C.14})$$

$$C(k) = \left( \frac{1}{2L_D k} \right)^2 \quad (\text{C.15})$$

$$L_D = \sqrt{\frac{ek_B T}{q^2 N_i}} \quad (\text{C.16})$$

where  $L_D$  is the Debye length, and  $N_i$  is the impurity density.

#### C.4 3D Intervalley and Intravalley Scattering Rates

The scattering rate from  $i^{\text{th}}$  valley to  $j^{\text{th}}$  valley is given as

$$\frac{1}{\tau_{INT}} = \frac{Z_j D_{ij}^2 (m_j^*)^{3/2}}{\sqrt{2\pi\rho\hbar^3} \omega_{ij}} \gamma_j^{1/2}(E') (1 + 2\alpha E') (N_{ij} + \frac{1}{2} \mp \frac{1}{2}) \quad (\text{C.17})$$

where  $D_{ij}$  is the intravalley deformation potential between the  $i^{\text{th}}$  and  $j^{\text{th}}$  valleys,  $Z_j$  is the equivalent  $j^{\text{th}}$  valley number,  $\rho$  is the mass density, and  $\hbar\omega_{ij}$  is the intravalley photon energy. After scattering, the electron energy is

$$E' = E + \Delta E_{ij} \pm \hbar\omega_{ij} \quad (\text{C.18})$$

$$N_{ij} = \frac{1}{e^{\frac{\hbar\omega_{ij}}{k_B T}} - 1} \quad (\text{C.19})$$

where  $\Delta E_{ij}$  is the conduction band energy difference. By using the above formulas, the equivalent inter-valley scattering rates can be found by replacing  $j$  with 1 and  $Z_j$  with  $(Z_j-1)$ . Since this scattering mechanism is isotropic,  $\beta$  is calculated as

$$\cos(\beta) = 1 - 2r_n \quad (C.20)$$

### C.5 3D $\leftrightarrow$ 2D Intervalley Scattering Rates

$\Gamma_{2D} \leftrightarrow L_{3D}$ ,  $L_{3D} \leftrightarrow \Gamma_{2D}$ , and  $L_{3D} \leftrightarrow \Gamma_{2D}$  transitions occur with the following scattering rates [62] :

$$\frac{1}{\tau_{\Gamma_i L_i}} = Z_L \frac{D_{\Gamma L}^2 m_L^{*3/2}}{\sqrt{2\hbar^2 \pi \rho \hbar \omega_{\Gamma L}}} [E_L (1 + \alpha_L E_L)]^{1/2} (1 + 2\alpha_L E_L) (N_q + \frac{1}{2} \pm \frac{1}{2}) \Lambda_{\Gamma_i L_i} \quad (C.21)$$

$$\frac{1}{\tau_{L_i \Gamma_i}} = Z_{\Gamma} \frac{D_{\Gamma L}^2 m_{\Gamma}^*}{2\hbar \rho \hbar \omega_{\Gamma L}} (1 + 2\alpha_{\Gamma} E_{\Gamma}) (N_q + \frac{1}{2} \pm \frac{1}{2}) \Lambda_{L_i \Gamma_i} \quad (C.22)$$

In the above equations,  $Z$  is the number of equivalent valleys,  $m^*$  is the effective mass in the final state, and  $\Lambda$  is the form factor between the initial and final state wavefunctions.  $D$  is the intervalley deformation potential,  $E$  is the energy references from the bottom of the valley, and  $\alpha$  is the nonparabolicity factor.

When 3D $\leftrightarrow$ 2D scattering mechanism is executed, the momentum in crystal growth direction is made zero and all of the energy is assigned to the energy corresponding to the momentum vector parallel to the heterointerfaces. This in-plane momentum vector's direction is random since QWIP is a 1D MQW device and the directions in the growth plane are indistinguishable.

When 2D→3D scattering mechanism is executed, electron momentum parallel to the heterointerfaces is conserved, and excess subband energy is assigned to the energy related to the momentum in the growth direction (z-direction) . The z momentum is randomly directed to the +z and -z directions with equal chance.

## C.6 2D Polar Optical Phonon Scattering Rates

The polar-optical phonon scattering rates are calculated using the Fermi's Golden Rule as [54,56]

$$\Gamma_{ij}(k) = \frac{e^2 w_{LO}}{2} \left( n_B(w_{LO}) + \frac{1}{2} \pm \frac{1}{2} \right) \int d^2 q \frac{H_{jij}^{eff}(q)}{q} \delta(E_i(k) \mp w_{LO} - E_j(k \mp q)) \quad (C.23)$$

where the upper signs for the emission and the lower ones for the absorption.  $n_B(w_{LO})$  is the Bose distribution function which gives the average number of phonons with energy  $\hbar w_{LO}$  at temperature T.  $H^{eff}$  is effective interaction defined in terms of the dielectric matrix to add dielectric screening effects.

$$H_{ijkl}(q) = \sum_{mn} \varepsilon_{ijnm}(q, w=0) H_{mnkl}^{eff}(q) \quad (C.24)$$

Without screening effects the subband form factors are expressed by

$$H_{ijkl}(q) = \int_0^\infty dz \int_0^\infty dz' e^{-q|z-z'|} \phi_i(z') \phi_j(z') \phi_k(z) \phi_l(z) \quad (C.25)$$

With screening effect the dielectric matrix is calculated by the random phase approximation (RPA) by

$$\varepsilon_{ijnm}(q) = \delta_{im} \delta_{jn} - V_{ijnm}(q) \chi_{nm}(q) \quad (C.26)$$

where  $\chi_{nm}(q)$  is the static polarizability. The form factors and the Coulomb interaction matrix elements are related by  $H_{ijkl}(q)=V_{ijkl}(q)/(2\pi e^2/q)$ . In the work presented in this thesis, only the static dielectric function is considered. The usual Thomas-Fermi screening corresponds to the  $q \rightarrow 0$  limit of our dielectric function. The static screening approximation adopted here should be appropriate for large carrier densities, since  $\hbar\omega_{LO}$  remains small compared with the characteristic energy (i.e. plasmon energy) of the electron gas.

### C.7 2D Acoustic Phonon Scattering Rates

The acoustic phonon scattering rate is expressed as

$$\frac{1}{\tau_{ij}} = \frac{m^* k_b T E_1^2}{\hbar^3 \rho v_{sl}^2} \int F^4(z) dz \quad (C.27)$$

where  $F(z)$  is the subband envelope wave function,  $E_1$  is the deformation potential constant,  $\rho$  is the density, and  $v_{sl}$  is the longitudinal sound velocity.

### C.8 2D Impurity Scattering Rates

In the quantum well region, the 2D electrons are subject to scattering due to ionized impurities distributed randomly. We considered two different types of 2D impurity scattering; remote ionized impurity scattering and background ionized impurity scattering [76,60].

### C.8.1 Remote Ionized Impurity Scattering Rate

There are two kinds of charged scattering centers: quantum well dopants, which are the scattering centers in the well, and remote scattering centers. Remote scattering centers are due to the unintentional doping in the AlGaAs barrier region, which is assumed to be  $1 \times 10^{14} \text{ cm}^{-3}$ . In our program, the approach of Hess [Emre58] is used to calculate the scattering rates due to both background and remote impurities.

Scattering rate due to remote impurities can be expressed as [76]

$$\frac{1}{\tau} = \frac{4\pi e^4 m^* N_R}{\hbar^3 \varepsilon^2 k} \int_0^\pi \frac{\exp(-4kz_0 \sin \theta) \sin \theta d\theta}{(2k \sin \theta + S)^2} \quad (\text{C.28})$$

where  $z_0$  is the separation distance from the barrier layer to the maximum of the square of the wave function,  $N_R$  is the remote impurity density,  $m^*$  is the effective mass,  $\varepsilon$  is the relative dielectric constant of the semiconductor,  $k$  is the absolute value of two dimensional wave-vector, and  $S$  is the two dimensional screening constant.  $S$  is given by

$$S = \frac{e^2 n_{2d}}{2kT\varepsilon\varepsilon_0} \quad (\text{C.29})$$

where  $n_{2d}$  is the two dimensional carrier density,  $\varepsilon$  and  $\varepsilon_0$  are the permittivities of the layers and free space respectively.

### C.8.2 Background Ionized Impurity Scattering Rate

The background ionized impurity scattering rate for the electrons in the quantum well is expressed as [76]

$$\frac{1}{\tau} = \frac{4\pi e^4 m^* N_B}{\hbar^3 \varepsilon^2 k} \int_0^\pi \frac{\sin \theta d\theta}{(2k \sin \theta + S)^2} \quad (\text{C.30})$$

where  $N_B$  is the background impurity density.

### C.9 3D-to-2D Capture and Escape Rates

The transition of electrons between the continuum and bound states ( $\Gamma_{3D} \leftrightarrow \Gamma_{2D}$  and  $L_{3D} \leftrightarrow L_{2D}$ ) is modelled as  $3D \leftrightarrow 2D$  polar optical phonon scattering [61]. As given in Ref. [61], the  $3D \rightarrow 2D$  scattering rate is expressed as

$$S_{3D \rightarrow 2D}(k_z, k_{//}, n) = \frac{e^2 \omega_{LO} m^*}{8\pi \hbar^2} \left( \frac{1}{\varepsilon_\infty} - \frac{1}{\varepsilon_s} \right) \left( n_B + \frac{1}{2} \pm \frac{1}{2} \right) \int_0^{2\pi} \frac{f_{k_z, n}(Q(\vartheta))}{\sqrt{Q^2(\vartheta) + q_s^2}} d\vartheta \quad (\text{C.31})$$

where

$$f_{k_z, n}(Q) = \int_{-\infty}^{\infty} dz \int_{-\infty}^{\infty} dz' \rho_{k_z, n}(z) \rho_{k_z, n}^*(z') e^{-\sqrt{Q^2 + q_s^2} |z - z'|} \left[ 1 - \frac{|z - z'| q_s^2}{2\sqrt{Q^2 + q_s^2}} - \frac{q_s^2}{2(Q^2 + q_s^2)} \right] \quad (\text{C.32})$$

and

$$\rho_{k_z, n}(z) = \psi_{k_z}^*(z) \psi_n(z) \quad (\text{C.33})$$

In the above expressions,  $\psi_{k_z}(z)$  is the unbound wavefunction with  $k_z$  being the component of the unbound wavevector in the  $z$  direction.  $\psi_n(z)$  is the 2D wavefunction obtained through the solution of the Schrödinger equation.  $\psi_{k_z}(z)$  is obtained following the approach presented in [77] for unbound states of arbitrary shaped potential [61].  $Q$  is the phonon wavevector parallel to the heterojunction plane.  $\vartheta$  is the angle between the related momentum vector components in the scattering process [61].  $q_s$  is the screening factor, and  $n_B$  is the phonon occupation number. The capture rate for a continuum electron is a function of its energy and momentum in the crystal growth direction.

The 2D→3D scattering rate is expressed as [61]

$$S_{2D \rightarrow 3D} = \frac{e^2 \omega_{LO} m^*}{8\pi \hbar^2} \left( \frac{1}{\epsilon_\infty} - \frac{1}{\epsilon_s} \right) \left( n_B + \frac{1}{2} \pm \frac{1}{2} \right) \int_{\alpha_{\min}}^{\frac{\pi}{2}} d\alpha \int_0^{2\pi} d\vartheta \frac{f_{k_z, n}(Q(\alpha, \vartheta))}{\sqrt{Q^2(\alpha, \vartheta) + q_s^2}} \quad (C.34)$$

In the equation above,  $\alpha$  is the angle between the 3D electron wave vector and QW plane [61].

When 3D↔2D scattering mechanism is executed, the momentum in crystal growth direction is made zero and all of the energy is assigned to the momentum vector parallel to the heterointerfaces. This in-plane momentum vector's direction is random since QWIP is a 1D MQW device and the directions in the growth plane are indistinguishable.

When 2D→3D scattering mechanism is executed, electron momentum parallel to the heterointerfaces is conserved and excess subband energy is assigned to the energy related to the momentum in the growth direction (z-direction). The z momentum is randomly directed to the +z and -z directions with equal chance.

## C.10 2D Intervalley Scattering Rates

$\Gamma_{2D \leftrightarrow L_{2D}}$  nonequivalent and  $L_{2D} \leftrightarrow L_{2D}$  equivalent intervalley scatterings are included in the Monte-Carlo simulations. The scattering rate is expressed as [64]

$$\frac{1}{\tau_{2D \text{Intervalley}}} = \Gamma_{ij}(k) = N \frac{m^* E_{iv}^2 (n_w + \frac{1}{2} \pm \frac{1}{2}) I_{iv}}{2\rho\omega_{iv}\hbar^2} \quad (C.35)$$

where  $I_{iv}$  is the overlap integral given as

$$I_{iv} = \int_{-\infty}^{\infty} dz \left| \psi_i^{v_i}(z) \right|^2 \left| \psi_f^{v_f}(z) \right|^2 \quad (C.36)$$



Here,  $N$  is the number of possible final valleys. It is 4 for  $\Gamma_{2D} \rightarrow L_{2D}$ , 1 for  $L_{2D} \rightarrow \Gamma_{2D}$ , and 3 for  $L_{2D} \rightarrow L_{2D}$  transitions.  $E_{iv}$  is the intervalley deformation potential,  $m^*$  is the effective mass in the final valley,  $\rho$  is the mass density,  $\omega_{iv}$  is the intervalley phonon energy.  $\psi_i^{v_i}(z)$  and  $\psi_f^{v_f}(z)$  are the initial and final valley envelope wavefunctions and,  $n_w$  is the phonon number.

## APPENDIX D

### MOMENTUM CALCULATION AFTER SCATTERING

After every scattering, both the magnitude and the direction of the particle's momentum should be updated. Magnitude of the particle's momentum is a function of energy difference before and after the scattering and is given by

$$p' = \sqrt{2m^* (E + \Delta E)} \quad (\text{D.1})$$

where  $p'$  is the momentum after scattering,  $E$  is the carrier's energy before scattering and  $\Delta E$  is the change in energy associated with the type of the scattering event selected.

If the scattering is isotropic (i.e., if the scattered electron has the same probability of being in any direction after scattering), the components  $k_x'$ ,  $k_y'$ , and  $k_z'$  can be found by considering that the probability density  $p(\phi', \theta') d\phi' d\theta'$  is proportional to the number of available states on a sphere of radius  $k'$ , where  $\phi'$  and  $\theta'$  are the azimuthal and polar angles of  $\mathbf{k}'$  with respect to  $k_z^L$ .  $p(\phi', \theta')$  equals  $\sin \theta'$ , since any  $\phi'$  is equally probable. Therefore,  $\phi'$  and  $\theta'$  can be determined using uniformly distributed random numbers between 0 and 1. The relations between the azimuthal, polar angles and random numbers are given by

$$\phi' = 2\pi r_n \quad (\text{D.2})$$

$$\cos(\theta') = 1 - 2r_m \quad (\text{D.3})$$

After  $\phi'$  and  $\theta'$  are selected using random numbers  $r_n$  and  $r_m$ , components of the wave vector are obtained using the following equations:

$$k'_x = k' \times \sin \theta' \times \cos \phi' \quad (\text{D.4})$$

$$k'_y = k' \times \sin \theta' \times \sin \phi' \quad (\text{D.5})$$

$$k'_z = k' \times \cos \theta' \quad (\text{D.6})$$

The above expressions are only valid for the case of isotropic scattering. For anisotropic scattering processes, such as impurity scattering and polar optical phonon scattering, the final state  $\mathbf{k}'$  is denoted by  $\theta$  and  $\phi$ , which are the polar and azimuthal angles of  $\mathbf{k}'$  with respect to the initial wave vector  $\mathbf{k}$ . The azimuthal angle  $\phi$  can also be determined randomly because the transition rate is independent of  $\phi$ . Thus,  $\phi$  can be found from

$$\phi = 2\pi r_n \quad (\text{D.7})$$

Polar angle  $\theta$  is given by

$$\cos \theta = 1 - \frac{2r_m}{1 + (1 - r_m) \left( \frac{2k}{q_D} \right)^2} \quad (\text{D.8})$$

for impurity scattering

$$\cos \theta = \frac{1 + f - (1 + 2f)^{r_m}}{f} \quad (\text{D.9})$$

for polar optical phonon scattering.

When updating the orientation of the electron wave vector  $\mathbf{k}$  in a laboratory frame  $(k_x^L, k_y^L, k_z^L)$ , it is convenient to work with a new frame  $(k_x^r, k_y^r, k_z^r)$ , in which the  $k_z$ -axis is parallel to the initial wave vector  $\mathbf{k}$ . The new frame is obtained by rotating  $(k_x^L, k_y^L, k_z^L)$  by an angle  $\alpha$  about the  $k_x$ -axis and then  $\beta$  about the  $k_z$ -axis, as illustrated in Figure D.1.

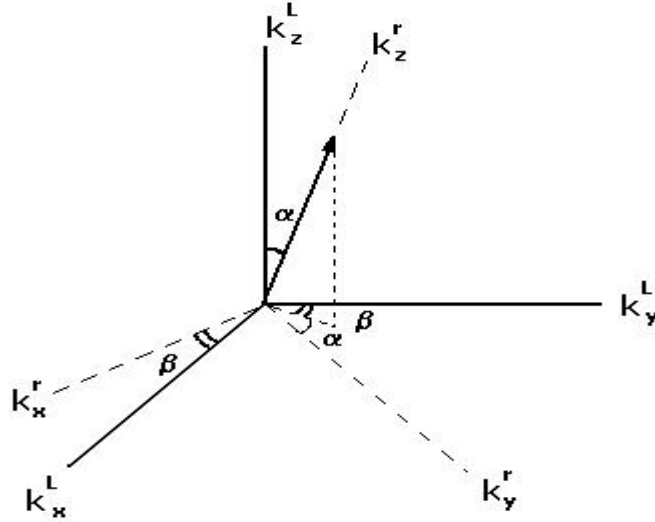


Figure D.1 Relation between the initial frame and new frame.

As the result of this rotation, the components of the wave vector after scattering in terms of the  $(k_x^L, k_y^L, k_z^L)$  frame are obtained as

$$\begin{pmatrix} k_x^r \\ k_y^r \\ k_z^r \end{pmatrix} = \begin{pmatrix} \frac{k_y}{\sqrt{k_x^2 + k_y^2}} & \frac{k_x k_z}{k \sqrt{k_x^2 + k_y^2}} & \frac{k_x}{k} \\ -\frac{k_x}{\sqrt{k_x^2 + k_y^2}} & \frac{k_y k_z}{k \sqrt{k_x^2 + k_y^2}} & \frac{k_y}{k} \\ 0 & \frac{-\sqrt{k_x^2 + k_y^2}}{k} & \frac{k_z}{k} \end{pmatrix} \begin{pmatrix} k' \sin \theta \cos \phi \\ k' \sin \theta \sin \phi \\ k' \cos \theta \end{pmatrix} \quad (\text{D.10})$$

## CURRICULUM VITAE

### PERSONAL INFORMATION

Surname, Name: Cellek, Oray Orkun  
Nationality: Turkish  
Date and Place of Birth: 1980, Ankara  
email: cellek@gmail.com

### EDUCATION

Degree	Institution	Year of Graduation
BS	METU Electrical and Electronics Engineering Department	2001
Minor	METU Physics Department, Solid State Physics	2001
High School	Yüce Fen Lisesi, Ankara	1997

### WORK EXPERIENCE

Year	Place	Enrollment
2006 -	ASELSAN Inc.	Design Engineer
2001-2006	METU Department of Electrical and Electronics Engineering	Research Assistant
2000-2001	METU Department of Electrical and Electronics Engineering	Part-time Research Project Personnel

### FOREIGN LANGUAGES

Advanced English

### PUBLICATIONS

1. O. O. Cellek, S. Özer, C. Beşikci, "High responsivity InP-InGaAs quantum-well infrared photodetectors: characteristics and focal plane array performance", *IEEE Journal of Quantum Electronics*, vol. 41, no.7, pp. 980-985, 2005.
2. S. Özer, O. O. Cellek, C. Beşikci, "Assessment of large format InP/InGaAs quantum well infrared photodetector focal plane array", *Infrared Physics and Technology*, vol. 47, pp. 115-118, 2005.
3. O. O. Cellek, S. Memiş, U. Bostancı, S. Özer, C. Beşikci, "Gain and transient photoresponse of quantum well infrared photodetectors: a detailed ensemble Monte Carlo study", *Physica E*, vol. 24, pp. 318-317, 2004.
4. O. O. Cellek, C. Beşikci, "Detailed investigation of electron transport, capture and gain in  $\text{Al}_{0.3}\text{Ga}_{0.7}\text{As}/\text{GaAs}$  quantum well infrared photodetectors", *Semiconductor Science and Technology*, vol. 19, pp. 183-190, 2004.